ABSTRACT

Title of dissertation: PRECISE STEERING OF PARTICLES IN ELECTROOSMOTICALLY ACTUATED MICROFLUIDIC DEVICES

Satej V. Chaudhary,
Doctor of Philosophy, 2010

Dissertation directed by: Professor Benjamin Shapiro
Department of Aerospace Engineering

In this thesis, we show how to combine microfluidics and feedback control to independently steer multiple particles with micrometer accuracy in two dimensions. The particles are steered by creating a fluid flow that carries all the particles from where they are to where they should be at each time step. Our control loop comprises sensing, computation, and actuation to steer particles along user-input trajectories. Particle positions are identified in real-time by an optical system and transferred to a control algorithm that then determines the electrode voltages necessary to create a flow field to carry all the particles to their next desired locations. The process repeats at the next time instant.

Our method achieves inexpensive steering of particles by using conventional electroosmotic actuation in microfluidic channels. This type of particle steering has significant advantages over other particle steering methods, such as laser tweezers. (Laser tweezers cannot steer reflective particles, or particles where the index of refraction is lower than that of the surrounding medium. More sophisticated optical vortex holographic tweezers require that the index of refraction does not differ substantially from that of the surrounding medium.). In this thesis, we address three specific aspects of this technology. First, we develop the control algorithms for steering multiple particles independently and validate our control techniques using simulations with realistic sources of initial position errors and system uncertainties. Second, we develop optimal path planning methods to efficiently steer particles between given initial and final positions. Third, we design high performance microfluidic devices that are capable of simultaneously steering five particles in experiment. (Steering of up to three particles in experiment had been previously demonstrated [1].)

PRECISE STEERING OF PARTICLES IN ELECTROOSMOTICALLY ACTUATED MICROFLUIDIC DEVICES

by

Satej V. Chaudhary

Dissertation submitted to the Faculty of the Graduate School of the University of Maryland, College Park in partial fulfillment of the requirements for the degree of

Doctor of Philosophy

2010

Advisory Committee:

Dr. Benjamin Shapiro, Chair/Advisor

Dr. Robert Sanner

Dr. Christopher Cadou

Dr. Alison Flatau

Dr. Howard Elman, Dean's Representative

Dedication

I dedicate this work to my wife Sonal and our baby Aakshaj.

Acknowledgments

I owe my gratitude to all the people who have made this thesis possible and because of whom my graduate experience has been one that I will cherish for ever. First, I would like to acknowledge my advisor Dr. Benjamin Shapiro for introducing me to the fascinating world of MEMS, for his guidance on structured problem solving, and his continuous support in my PhD program. A very special thanks goes to my advisory committee Dr. Robert Sanner, Dr. Christopher Cadou, Dr. Alison Flatau, and Dr. Howard Elman, whose incisive questions reinforced rigor in my analysis and helped me sharpen my arguments. I would also like to acknowledge Dr. Robert Sanner's inputs on the development of the control algorithm for our device.

The multi-particle steering project would not have been possible without the resourcefulness, enthusiasm, camaraderie, teamwork, and dedication of my colleagues Roland Probst, Mike Armani, and Zach Cummins. I thank them for their invaluable support in completion of this thesis and for their friendship.

Finally, I am forever indebted to my parents and to my wife for their understanding, endless patience and encouragement when it was most required.

Table of Contents

List of Figures

Chapter 1

Introduction

1.1 Background

The ability to steer individual particles inside microfluidic systems is useful for navigating particles to localized sensors, cell sorting, sample preparation, and combinatorial testing of particle interactions with other particles, with chemical species, and with distributed sensors. A variety of methods are currently used to manipulate particles inside microfluidic systems: individual particles can be steered by laser tweezers [2], [3], [4]; they can be trapped, and steered to some degree, by dielectrophoresis (DEP) [5], [6], [7]; and by traveling-wave-dielectrophoresis [7], [8]; held by acoustic traps [9]; steered by manipulating magnets attached to the particles [10]; and guided by MEMS pneumatic array [11]. Cohen [12], [13] uses a similar feedback control approach, invented independently after ours, to trap and steer a single particle, by using electroosmotic or electrophoretic actuation.

Of these methods, laser tweezers are the gold standard for single particle manipulation. Askin's survey article [2] provides a history of optical trapping of small neutral particles, atoms, and molecules. Current laser tweezer systems can create up to four hundred three-dimensional traps, they can trap particles ranging in size from tens of nanometers to tens of micrometers, and trapping forces can exceed 100 pN with resolutions as fine as 100 aN, and the positioning accuracy can be below

tens of nanometers[3], [14]. However, optical tweezers require lasers and delicate optics, they are expensive, and the whole system is unlikely to be miniaturized into a hand-held format. An additional disadvantage of laser tweezers is that it can only be used to steer particles with a refractive index greater than that of the surrounding medium. For example, in the quantum chip project at University of Maryland, laser tweezers cannot be used to steer quantum dots to place them at precise locations on a substrate. The aforementioned methods (DEP, acoustic traps, manipulation via attached magnets, and steering via pneumatic arrays systems) can be miniaturized into handheld formats but their steering capabilities are not as sophisticated as those of laser tweezers.

Our approach uses vision-based microflow control to steer particles by correcting for particle deviations - at each time instant we create a fluid flow to move the particles from their current position to their intented destination. This allows very simple devices, actuated by routine methods (electroosmosis), to replicate the planar steering capabilities typically requiring laser tweezers. We have shown that our approach permits a device with four electrodes to steer a single cell, a device with eight electrodes to steer up to three particles, and a device with twelve electrodes to steer up to five particles simultaneously. The method is noninvasive (the moving fluid simply carries the particles along), the entire system can be miniaturized into a handheld format (both the control algorithms and the optics can be integrated onto chips), we can steer almost any kind of visible particle (neutral particles are carried along by the electroosmotic flow, charged particles are actuated by a combination of electroosmosis and electrophoresis), and the system is cost effective (the

most expensive part is the camera and microscope, and these will be replaced by an on-chip optical system for the next generation of devices).

Due to the correction for errors provided by the feedback loop, the flow control algorithm steers the particles along their desired paths even if the properties of the particles (their charge, size, and shape) and the properties of the device and buffer (the exact geometry, the zeta potential, pH, and other factors) are not known precisely. The fundamental disadvantage of our approach is its lower accuracy as compared to laser tweezers: our positioning accuracy will always be limited by the resolution of the imaging system and by the Brownian motion that particles experience in-between flow control corrections. Our current optical resolution is of the order of one micron, and the Brownian drift during each control time step is around 100 nm. In addition it is not possible to steer a large number of particles with our method, like it is with laser tweezers.

Both feedback and microflows are essential for our particle steering capability. Feedback is required to correct for particle position errors at each instant in time. At the microscale, the Navier-Stokes equations reduce to a set of simpler equations that are easy to invert and it is relatively straightforward to calculate the necessary actuation to steer multiple particles at once. Note: The Navier-Stokes equations governing the motion of macroflows are complex and difficult to invert making it hard to determine the necessary actuation to steer particles.

1.2 Thesis Outline

This thesis is concerned with discussing certain theoretical and experimental challenges that were overcome in the course of demonstrating multi-particle steering. Building upon chapter 1, chapter 2 presents equations governing fluid and particle motion under electroosmotic actuation. In chapter 3, we design the control algorithm to steer the particles along desired trajectories. In chapter 4 we look at a path planning method to efficiently transport particles between given initial and final positions. Lastly, in chapter 5, we look at high performance device design to enable demonstration of five particle steering in experiment. Several researchers have contributed to different aspects of this project. Details about their contributions are provided in the final section of this chapter.

1.3 Overview of Steering by Feedback Control

Fig. 1.1 shows the basic control idea for steering a single particle: a microfluidic device , an optical observation system, and a computer with a control algorithm, are connected in a feedback loop. The vision system locates the position of the particle in real time, the computer then compares the current position of the particle with the desired (user input) particle position, the control algorithm computes the necessary actuator voltages that will create the electric field, or the fluid flow, that will carry the particle to its intended location, and these voltages are applied at the electrodes in the microfluidic device. For example, if the particle is currently north-west of its desired location, then a south-east flow must be created. The process

repeats at each time instant and forces the particle to follow the desired path.

Both neutral and charged particles can be steered in this way: a neutral particle is carried along by the flow that is created by electroosmotic forces, and a charged particle is driven by a combination of electroosmotic and electrophoretic effects. In either case, it is possible to move a particle at any location in the device, to the north, east, south , or west by choosing the appropriate voltages at the four electrodes. It is also possible to use this scheme to hold a particle in place - whenever the particle deviates from its desired position, the electrodes create a correcting flow to bring it back to its target location.

Surprisingly, it is also possible to steer multiple particles independently using this feedback control approach [15] (see also chapter 3). A multi-electrode device is able to actuate multiple fluid flow modes. Different modes cause particles in different locations to move in different directions. By judiciously combining these modes, it is possible to move all particles in the desired directions. The control algorithm that can combine the modes in this manner is described in detail in chapter 3. The algorithm requires some knowledge of the particle and system properties but this knowledge does not have to be precise. The reason is that feedback, the continual comparison between the desired and actual particle positions, serves to correct for errors and makes the system robust to experimental uncertainties. Even though our experiments have sources of error, some of which are unavoidable, such as variations in device geometry, parasitic pressure forces caused by surface tension at the reservoirs, Brownian noise, and variations in zeta potentials and charges on the particles - our control algorithm still steers all the particles along their desired

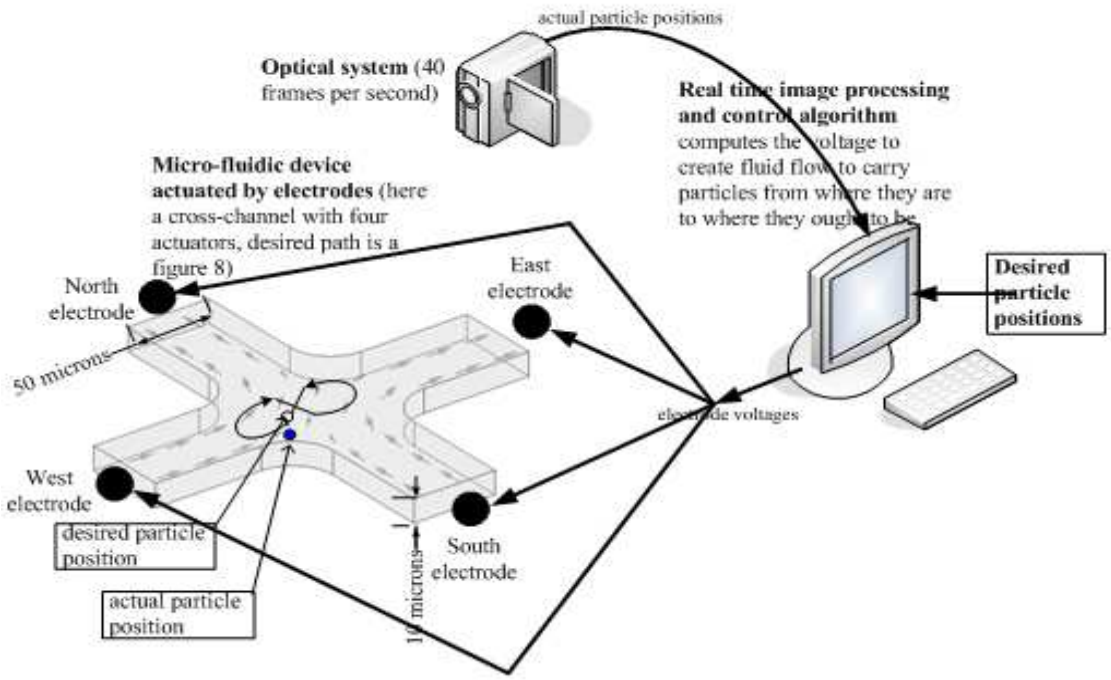

Figure 1.1: Feedback control particle steering approach for a single particle. A microfluidic device with standard electroosmotic actuation is observed by a camera that informs the control algorithm of the current particle position. The control algorithm compares the actual position against the desired position and finds the actuator voltages that will create a flow to steer the particles from the current location to where it should be. The process repeats continuously until the particles reach the destination.

trajectories.

1.4 Author's Contribution to Research within the Larger Team

Several graduate students within Dr. Benjamin Shapiro's research group have contributed to this project (Mike Armani, Zach Cummins, and Roland Probst). This section outlines the contribution made by the author within this larger team.

The concept of microfluidic particle control was first suggested by Dr. Benjamin Shapiro in 2002. Michael Armani and Roland Probst demonstrated the first particle steering in experiments in 2003 [1] with a simple cross channel device design. This used a simple control algorithm that created a flow to the North if the particle was to the South of its desired position (or West if it was East of its desired position, etc.). With this simple control algorithm it was not possible to steer more than one particle.

The equations governing electroosmotic actuation are documented in literature [16], [17] but were applied to the situation of multiple channels feeding into a planar control region by the author. The author created models of the electric field, fluid dynamics, and resulting particle motion under control within the devices. He further developed a simulation environment to develop and test strategies for control of multiple particles. The multi-particle control algorithms that the author designed, mathematically developed, analyzed, and validated in simulations, were then further adapted to the experiment by Roland Probst. Probst experimentally demonstrated three particle steering in 2005. At this stage, Zach Cummins became involved in

the project and during his overlap with the author, Cummins improved the vision system and created a Matlab graphical user interface for operating the setup. At this stage, at the end of 2005, through the control theory development efforts of the author and Roland's contributions, we were able to control up to three particles.

Both the author and Roland Probst led a thorough investigation into the factors that prevented steering of more than three particles in experiments. To this end, the author proved that the maximum particle actuation speed dropped rapidly with increase in the number of particles, and for more than three particles the actuation was no longer sufficient to overcome the parasitic pressure flow. To address this issue, the author redesigned the devices to enhance particle actuation by a factor of more than five. The author, Cummins, and Probst then used these high performance devices to demonstrate steering of five particles in an experiment.

To demonstrate steering of multiple particles it was also imperative to carefully design the paths. Improperly designed paths would lead to actuator saturation and subsequent loss of control. Probst and the author both worked on developing optimal path planning methods (2007) and eventually, and independently, achieved two different but complementary approaches. This thesis includes the research on optimal path planning carried out by the author.

Chapter 2

Governing Equations

This chapter provides equations relevant to modeling the microfluidic device in consideration. The first section of this chapter describes the physics of electroosmosis. The second section provides equations governing fluid motion. The third section provides equations governing motion of microparticles in the microfluidic device.

2.1 Physics of Electroosmosis

When a potential difference is applied across the two ends of a glass microcapillary filled with an aqueous buffer as shown in Fig. 2.1, the fluid inside it moves in the direction of the electric field. This phenomenon is called electroosmosis. Electroosmosis provides a very effective method of transporting fluid at the microscale using electricity.

The mechanism of fluid transport through electroosmosis is as follows. Glass surfaces acquire a negative surface charge when brought in contact with an electrolyte (aqueous buffer solution). Chemists widely believe that this spontaneous charging of glass surfaces is due to the deprotonation of surface groups ($SiOH$) on the surface of glass [17]. The equilibrium reaction associated with this deprotonation

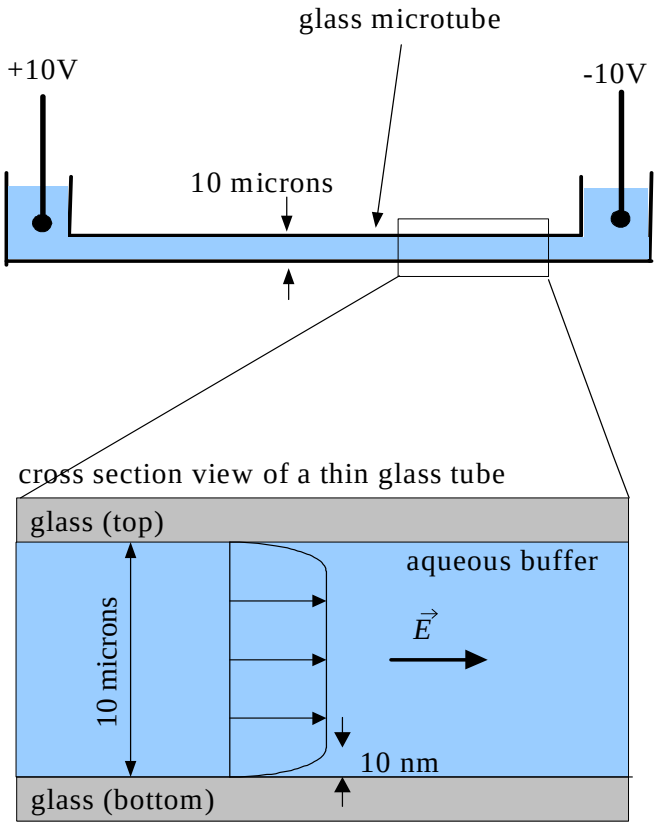

Figure 2.1: This diagram illustrates the transport of fluid in a glass microcapillary due to electroosmosis. When a potential difference is applied across a glass microcapillary filled with an aqueous buffer, fluid moves in the direction of the electric field. This movement of fluid is called electroosmosis.

can be represented as

$$SiOH \rightleftharpoons SiO^- + H^+ \tag{2.1}$$

Models describing this reaction have been proposed for several types of glass [18], [19], [20].

The negatively charged surface attracts positive ions in the electrolyte towards it. This electrostatic attraction combined with the random thermal motion of the ions gives rise to an electric double layer close to the glass surface. The electrical double layer is a region close to the charged surface where there is an excess of positive ions over negative ions to neutralize the surface charge. Fig. 2.2 shows a schematic of the electrical double layer [17], [21]. We may observe that if there were no thermal motion, there would be exactly as many positive ions in the electrical double layer as needed to balance the charge on the surface. However, because of the finite temperature and associated random thermal motion of the ions, those ions at the edge of the electric double layer where the electric field is weak, have enough thermal energy to escape from the electrostatic potential well. Therefore the edge of the double layer is considered to be at a position where the electrostatic potential energy is approximately equal to the average thermal energy of the positive ions (RT/2 per mole per degree of freedom). For the simple case of a symmetric electrolyte with two monovalent ions, the characteristic thickness of the electric double layer λ_D is given by [22]

$$\lambda_D = \left(\frac{\epsilon k T}{2 F^2 c} \right)^{\frac{1}{2}}, \tag{2.2}$$

where ϵ is the permittivity of the liquid, k is the Boltzman constant, T is the

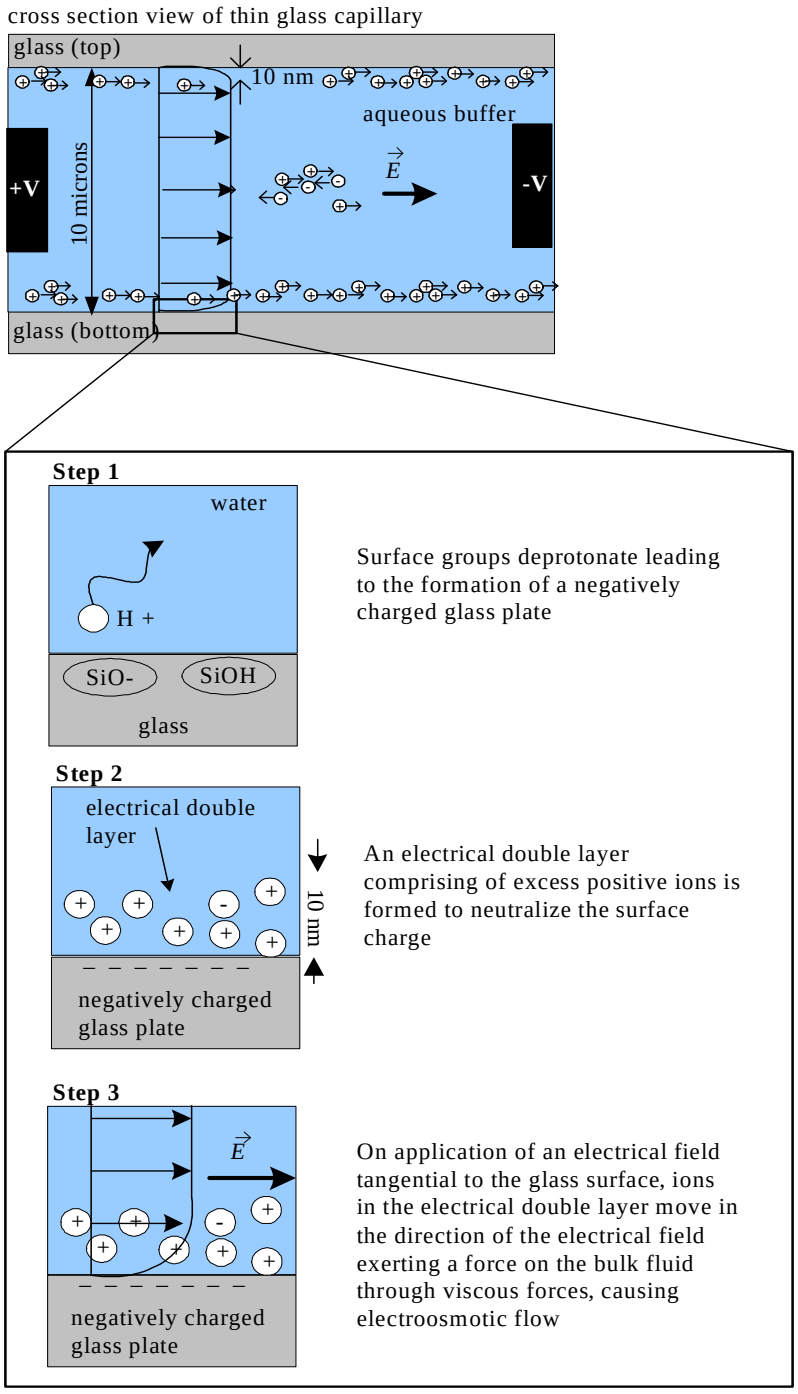

Figure 2.2: Mechanism of electroosmotic actuation. The three steps in the mechanism are illustrated - formation of surface charge on glass, the formation of an electrical double layer to neutralize the surface charge, and movement of the electrical double layer under influence of an external electric field.

temperature, F is Faraday's constant, and c is the molar concentration of each of the two ion species in the bulk. At typical biochemical, singly ionized buffer concentrations of 10 mM and room temperature of 298 K , the electric double layer is of the order of 10 nm thick.

When an electric field is applied tangential to the glass surface, the ions in the diffuse electric double layer experience a electrostatic body force and move in the direction of the electric field. This moving layer of ions in the electrical double layer exerts a force on the bulk fluid via viscous drag resulting in a bulk flow of fluid in the direction of the electric field. This is the mechanism of electroosmotic actuation.

In addition, it is important to note that the bulk fluid is electrically neutral (i.e. it contains equal number of positive and negative ions), and even though these ions move under the influence of the electric field, the viscous drag created by these ions cancel each other with a net zero contribution to the bulk flow.

2.2 Equations Governing Fluid Motion

This section provides the equations governing fluid motion in the microfluidic device. Section 2.2.1 provides the full coupled Navier-Stokes and Gauss equations governing fluid flow. Section 2.2.2 provides a simplification of the governing equations through the use of dimensional analysis techniques. In section 2.2.3, the fluid flow solution is expressed as a superposition of electroosmotic and pressure-driven flow components. Section 2.2.4 provides the solution to the electroosmotic flow component. Section 2.2.5 provides a solution to the pressure-driven flow component.

2.2.1 Full coupled Navier-Stokes and Gauss equations

We start by considering the Knudsen number (K_n) of the device, which provides a measure of accuracy of the continuum hypothesis for a fluid system [23]. For our case, the Knudsen number is

$$K_n = \frac{\lambda_{water}}{h} = \frac{3 \times 10^{-10} \text{ m}}{10 \times 10^{-6} \text{ m}} = 3 \times 10^{-5}, \tag{2.3}$$

where λ_{water} is the mean free path of water molecules at standard temperature and pressure; and h is the channel height of the device. Since the Knudsen number is less than 10^{-2}, the flow is within the continuum regime [23].

Since the flow is a continuum, the Navier-Stokes equations are applicable. Because we are modeling the flow of water, incompressibility and Newtonian fluid assumptions may be used [24]. Hence, the equations governing fluid motion are given by

$$\nabla \cdot \overrightarrow{V} = 0 \tag{2.4}$$

and

$$\rho \left(\frac{\partial \overrightarrow{V}}{\partial t} + \overrightarrow{V} \cdot \nabla \overrightarrow{V} \right) = -\nabla p + \mu \nabla^2 \overrightarrow{V}, \tag{2.5}$$

where $\overrightarrow{V} = (u, v, w)$ is the three dimensional fluid velocity, p is the pressure, μ is the dynamic viscosity, ρ is the fluid density, ∂t denotes the partial derivative with respect to time, ∇ is the gradient operator, and $\nabla \cdot ()$ is the divergence operator.

Since the electrical double layer thickness (10 nm) is very small compared to the channel dimensions, we can state the wall boundary conditions in terms of the

velocity slip condition (Helmoltz-Smoluchowski equation) [16], [25], [26] as

$$\overrightarrow{V}_{wall} = -\frac{\epsilon\zeta}{\mu}\overrightarrow{E}. \tag{2.6}$$

where $\overrightarrow{V}_{wall}$ represents the fluid velocity at the wall, $\overrightarrow{E} = (E_x, E_y, E_z)$ is the electric field, ϵ is the permittivity of the fluid, and ζ is the zeta potential at the wall. The pressure boundary condition at the inlets is given by the equation

$$p(\partial D_i) = P_i, \tag{2.7}$$

where ∂D_i denotes the surface corresponding to i^{th} inlet, and P_i denotes the pressure at the i^{th} inlet.

The equations governing electric fields are given by Gauss's law [26]:

$$-\epsilon\nabla^2\phi = 0 \tag{2.8}$$

and

$$\overrightarrow{E} = -\nabla\phi, \tag{2.9}$$

where ϕ is the electric potential. The corresponding boundary conditions - insulation at the walls and voltage potential at the inlets are given by

$$\overrightarrow{n} \cdot \overrightarrow{E}_{wall} = 0 \tag{2.10}$$

and

$$\phi(\partial D_i) = \gamma_i, \tag{2.11}$$

where $\overrightarrow{n}$ denotes the normal vector to the surface, $\overrightarrow{E}_{wall}$ is the electric field at the wall, and γ_i is the electric potential at the i^{th} inlet.

2.2.2 Simplification of Fluid Flow Equations at the Microscale

At the microscale, and at our operating conditions, these equations reduce to a set of simple linear PDEs [16]. In order to obtain these simplified equations, we first normalize equations (2.5) and (2.4) using the non-dimensionalization of variables shown below:

$$\overrightarrow{r}^* = \frac{\overrightarrow{r}}{d}, \tag{2.12}$$

$$t^* = \frac{t}{t_c}, \tag{2.13}$$

$$\overrightarrow{V}^* = \frac{\overrightarrow{V}}{V_c}, \tag{2.14}$$

and

$$p^* = \frac{p}{(\mu V_c/h)}, \tag{2.15}$$

where $\overrightarrow{r}$ is the position vector, $d \approx 20 \times 10^{-6}$ m is the hydraulic diameter for the channel (for non-circular channels, hydraulic diameter is given by four times the cross sectional area divided by the cross-sectional perimeter). We chose the cross section to have rectangular width of 100×10^{-6} m and depth of 25×10^{-6} m) , $t_c = 1$ s is the characteristic time scale (e.g., for an applied forcing function), $V_c = 10 \times 10^{-6}$ ms^{-1} is the characteristic electroosmotic velocity magnitude, $\mu = 10^{-3}$ Nsm^{-2} is the dynamic viscosity, $E_c = 5000$ Vm^{-1} is the characteristic electric field strength (this value was chosen as a potential difference of 20V is applied across 4 mm), and $\epsilon = 80.2 \times 8.854 \times 10^{-12}$ $\mathrm{CN}^{-1}\mathrm{m}^{-2}$ permittivity of the fluid. We then compare the order of magnitude of each term in the equation, and finally discard the terms of extremely small magnitude.

Substituting equations (2.12)-(2.15) in (2.5) and (2.4), the normalized equations of fluid flow are given by

$$\nabla \cdot \overrightarrow{V}^* = 0 \tag{2.16}$$

and

$$St\,\mathrm{Re}\,\frac{\partial \overrightarrow{V}^*}{\partial t^*} + \mathrm{Re}\,\overrightarrow{V}^* \cdot \nabla \overrightarrow{V}^* = -\nabla^* p^* + \nabla^{*2} \overrightarrow{V}^*, \tag{2.17}$$

where the ∇ and ∇^2 operators are non-dimensionalized using d. St and Re are the Strouhal and Reynolds numbers respectively, and are defined as

$$St = \frac{d}{t_c V_c} \tag{2.18}$$

and

$$\mathrm{Re} = \frac{\rho V_c h}{\mu}. \tag{2.19}$$

The Strouhal number is a measure of the unsteadiness of the flow and the Reynolds number gives the ratio of inertial and viscous forces in the fluid flow. In our case,

$$St = 2 \tag{2.20}$$

and

$$\mathrm{Re} = 2 \times 10^{-4}. \tag{2.21}$$

Hence, we see that, the terms on the left-hand side are extremely small in magnitude and can be ignored. The normalized equations of fluid motion then become

$$\nabla \cdot \overrightarrow{V}^* = 0 \tag{2.22}$$

and

$$0 = -\nabla^* p^* + \nabla^{*2} \overrightarrow{V}^*. \tag{2.23}$$

Using (2.12)-(2.15), and transforming (2.22) and (2.23) back to the dimensional form, the equations governing fluid motion are given by

$$\nabla \cdot \overrightarrow{V} = 0 \tag{2.24}$$

and

$$-\nabla p + \mu \nabla^2 \overrightarrow{V} = 0. \tag{2.25}$$

The boundary conditions are given by equations (2.6) and (2.7).

2.2.3 Solution of Equation as a Superposition of Electroosmotic and Pressure Flows

Due to the linear nature of equations (2.24) and (2.25), their solution can be expressed as a linear superposition of the electroosmotic and pressure driven components [17]:

$$\overrightarrow{V} = \overrightarrow{V}_{EO} + \overrightarrow{V}_p. \tag{2.26}$$

The rationale behind the decomposition of the velocity field is as follows: If $\overrightarrow{V}_{EO}$ satisfies

$$\nabla \cdot \overrightarrow{V}_{EO} = 0 \tag{2.27}$$

and

$$\mu \nabla^2 \overrightarrow{V}_{EO} = 0 \tag{2.28}$$

with boundary conditions

$$\overrightarrow{V}_{EOwall} = -\frac{\epsilon\zeta}{\mu}\overrightarrow{E}, \tag{2.29}$$

(these correspond the equations of fluid flow due to electroosmosis in the absence of externally applied or internally generated pressure gradients, which are obtained by setting $\nabla p = 0$ in (2.24) and (2.25)), and $\overrightarrow{V}_p$ satisfies

$$\nabla \cdot \overrightarrow{V}_p = 0 \tag{2.30}$$

and

$$-\nabla p + \mu \nabla^2 \overrightarrow{V}_p = 0 \tag{2.31}$$

with boundary conditions

$$\overrightarrow{V}_{Pwall} = 0 \tag{2.32}$$

and

$$p(\partial D_i) = P_i \tag{2.33}$$

(these correspond to equations of fluid motion due to pressure driven flow in the absence of an electrical double layer), then, adding (2.27) and (2.30); (2.28) and (2.31); and boundary conditions (2.29), (2.32) and (2.33); and substituting $\overrightarrow{V} = \overrightarrow{V}_{EO} + \overrightarrow{V}_p$, we get that $\overrightarrow{V}$ satisfies

$$\nabla \cdot \overrightarrow{V} = 0 \tag{2.34}$$

and

$$-\nabla p + \mu \nabla^2 \overrightarrow{V} = 0 \tag{2.35}$$

with boundary conditions

$$\overrightarrow{V}_{wall} = 0 \tag{2.36}$$

and

$$p(\partial D_i) = P_i. \tag{2.37}$$

2.2.4 Solution for Electroosmotic Flow

Equations governing electroosmotic flow are given by (2.27) and (2.28) with boundary conditions (2.43). We hypothesize that a solution of the equation is of the form [16]

$$\overrightarrow{V}_{EO} = c_0 \overrightarrow{E}, \tag{2.38}$$

where c_0 is an undetermined constant, and $\overrightarrow{E}$ is the electric field. The rationale behind this hypothesis is the following: The electric field satisfies both, the Faraday and Gauss' laws, which are given by

$$\nabla \cdot \overrightarrow{E} = 0 \tag{2.39}$$

and

$$\nabla \times \overrightarrow{E} = 0. \tag{2.40}$$

From equation (2.39), we have, $\overrightarrow{V}_{EO} = c_0 \overrightarrow{E}$ directly satisfies equation (2.27). To prove that $\overrightarrow{V}_{EO} = c_0 \overrightarrow{E}$ satisfies equation (2.28), we use a well known vector identity

$$\nabla^2 \overrightarrow{V}_{EO} = \nabla(\nabla \cdot \overrightarrow{V}_{EO}) - \nabla \times \nabla \times \overrightarrow{V}_{EO}. \tag{2.41}$$

From equations (2.41), (2.39), and (2.40), we have that $\overrightarrow{V}_{EO} = c_0 \overrightarrow{E}$ satisfies (2.28). We choose

$$c_0 = -\frac{\epsilon \zeta}{\mu} \tag{2.42}$$

to ensure that the hypothesized solution $\overrightarrow{V}_{EO} = c_0 \overrightarrow{E}$ satisfies the boundary condition (2.29) as well. The fluid flow velocity due to electroosmosis, in the bulk flow region bounded by the slip surfaces, is therefore given by

$$\overrightarrow{V}_{EO} = -\frac{\epsilon\zeta}{\mu}\overrightarrow{E}. \tag{2.43}$$

Since the solution of the Laplace equation with fixed boundary conditions is unique [27], and PDE (2.28) is a Laplace equation, we can be sure that (2.43) is the only solution for the electroosmotic flow in the bulk flow region.

Note that the electroosmotic flow is directly proportional to the electric field and responds instantly to it (because the Reynolds number is so small). Also, it has a plug flow profile in the dimension perpendicular to the flow. Fig. 2.3 provides an example of an electroosmotic flow solution. The electric field $\overrightarrow{E}$ is computed by first solving the Gauss equations (2.8) and (2.9) with boundary conditions (2.11) and (2.10). We solved these equations using COMSOL, a commercially available numerical PDE solver.

2.2.5 Solution for Pressure-Driven Flow

Equations governing pressure driven flow (also known as Stokes flow) are given by (2.30) and (2.31) with boundary conditions (2.32) and (2.7). We solved these equations using COMSOL, a commercially available numerical PDE solver. Fig. 2.3 provides an example of a pressure driven flow solution.

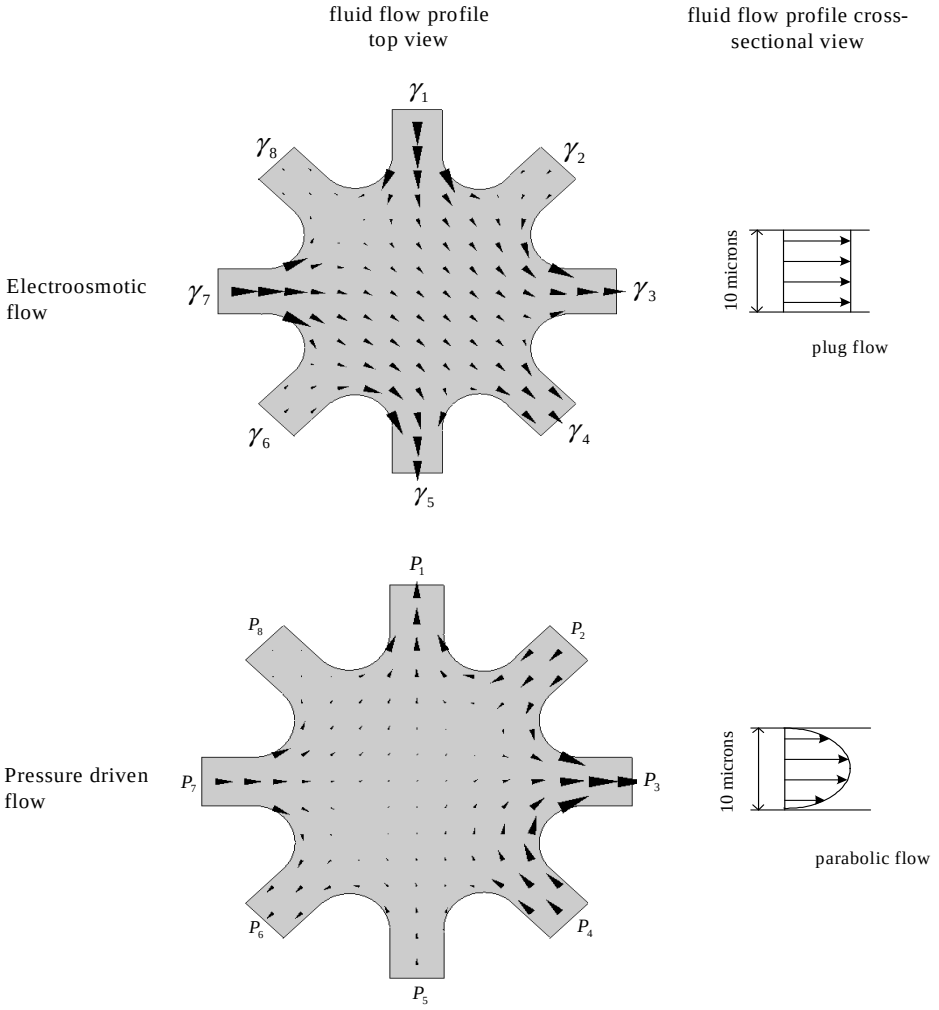

Figure 2.3: Sample solutions for electroosmotic and pressure-driven flows respectively. The electroosmotic flow is directly proportional to the electric field and has a plug flow profile in the cross sectional view. The pressure-driven flow has a parabolic profile in the cross sectional view.

2.3 Equations Governing Particle Motion

In this section, we shall obtain equations governing motion of microparticles in the microfluidic device. Their motion is a vector sum of four components: motion due to electroosmotic flow, pressure-driven flow, electrophoretic forces, and Brownian motion. Section 2.2.3 provides a mathematical expression for the components of particle motion due to electroosmosis and pressure-driven flow. Section 2.3.2 and 2.3.3 provide a mathematical expression for the components of particle motion due to electrophoresis and Brownian motion. Section 2.3.4 provides the equation governing net particle motion. Finally, in Section 2.3.5 we express the particle velocities in terms of input voltage vectors.

2.3.1 Particle Motion due to Electroosmotic and Pressure flows

As seen in previous sections, the net fluid flow in the device is given by the superposition of electroosmotic and pressure flows. If the particles are neutral, we can assume that they flow perfectly along with the fluid at all times. This assumption can be justified as follows: Consider a spherical particle of radius a_p in the fluid. When the fluid flows at velocity V_0 relative to the particle, the particle experiences a drag force F_d, which can be calculated by the classical Stokes drag law [26]:

$$F_d = 6\pi\mu a_p V_0. \tag{2.44}$$

The motion of the particle as it accelerates due to F_d can be modeled by Newton's second law:

$$m\frac{dv}{dt} = 6\pi\mu a_p(V_0 - v), \tag{2.45}$$

where m is the mass of the particle, v is the velocity of the particle at any given instant, and $V_0 - v$ is the relative velocity of the fluid with respect to the particle. The time t_{St}, required for the particle to accelerate to velocity $0.999V_0$, can be determined by rearranging equation (2.45) and integrating both the variable t between limits 0 to t_{St} and the variable v between limits 0 to $0.999V_0$:

$$\int_0^{0.999V_0} \frac{dv}{V_0 - v} = \frac{6\pi\mu a_p}{m} \int_0^{t_{St}} dt \tag{2.46}$$

solving which, we get

$$t_{St} = \frac{m}{6\pi\mu a_p} \ln\left(\frac{1}{0.001}\right). \tag{2.47}$$

For a particle of radius $a_p = 1 \times 10^{-6}$ m (reflecting the size of polystyrene beads used in our experiments) and assuming its density to be approximately equal to that of water, $\rho \approx 10^3$ kg m^{-3}, we have $t_{St} \approx 10^{-6}$ s. Since the characteristic time scale in our experiments is seconds, for all practical purposes we can assume that the particles move along with the fluid.

Hence the component of the microparticle motion due to electroosmosis $\dot{\overrightarrow{r}}_{EO}$ can be expressed as

$$\dot{\overrightarrow{r}}_{EO} = -\frac{\epsilon\zeta}{\mu}\overrightarrow{E}(\overrightarrow{r}) \tag{2.48}$$

and the component of the motion due to pressure driven flow $\dot{\overrightarrow{r}}_p$ can be expressed as

$$\dot{\overrightarrow{r}}_p = \overrightarrow{V}_p(\overrightarrow{r}) \tag{2.49}$$

where $\overrightarrow{r}$ is the position vector of the particle.

2.3.2 Particle Motion due to Electrophoresis

If the particles are charged, (polystyrene beads may acquire a surface charge in water [26], [22]) they experience an electrophoretic drift velocity with respect to the fluid on application of an electric field. This drift velocity is given by

$$\dot{\overrightarrow{r}}_{Ep} = c\overrightarrow{E}(\overrightarrow{r}), \tag{2.50}$$

where c is the particle's electrophoretic mobility.

2.3.3 Particle Motion due to Brownian Motion

In addition to the previously discussed contributions to motion, the particles also exhibit a random walk or Brownian motion due to collisions with fluid molecules. The particle velocity is modeled as [26], [28],

$$\dot{\overrightarrow{r}}_{B} = \sqrt{\frac{kT}{3\pi\mu a_p dt}}\,\overrightarrow{\omega}(0,1), \tag{2.51}$$

where $\overrightarrow{\omega}(0,1)$ is a 2 by 1 vector whose elements are Gaussian random variables with zero mean and a variance of one, and dt is the time interval over which the particle displacement is measured. Note that the average particle displacement in time dt given by

$$\delta_B = \sqrt{\frac{kTdt}{3\pi\mu a_p}} \approx 150 \text{ nm} \tag{2.52}$$

is a very small number compared to particle diameter (2.5 microns). For calculation purposes, here we chose $dt = 0.05$ s because the control voltages are updated 20 times every second in experiments.

2.3.4 Equations for Net Particle Motion

From equations (2.48), (2.49), (2.50), and (2.51) the net particle velocity is given by

$$\dot{\overrightarrow{r}} = -\frac{\epsilon\zeta}{\mu}\overrightarrow{E}(\overrightarrow{r}) + c\overrightarrow{E}(\overrightarrow{r}) + \overrightarrow{V}_p(\overrightarrow{r}) + \sqrt{\frac{kT}{3\pi\mu a_p dt}}\overrightarrow{\omega}(0,1). \tag{2.53}$$

The particle motion due to electroosmosis and electrophoresis is in the direction of the electric field and can be combined together. The particle motion due to pressure flow and Brownian motion cannot be controlled and hence we consider them as uncertainty terms. The net particle velocity equation is therefore given by

$$\dot{\overrightarrow{r}} = \left(-\frac{\epsilon\zeta}{\mu} + c\right)\overrightarrow{E}(\overrightarrow{r}) + \delta \tag{2.54}$$

where δ denotes the uncertainty due to Brownian motion and pressure flow.

2.3.5 Governing Equations for a System of Particles in Terms of Input Voltages

In order to obtain the equations governing motion for a system of particles, in terms of input voltage, consider a microfluidic device with n inlets, with voltages $\gamma_1, \gamma_2, .., \gamma_n$ applied to the n electrodes, and say we wish to obtain governing equations for a system of m particles at position vectors $\overrightarrow{r}_1, \overrightarrow{r}_2, .., \overrightarrow{r}_m$. From equation (2.54) the equations governing nominal particle motion for the m particles are given

by

$$\begin{bmatrix} \dot{\overrightarrow{r}}_1 = \left(-\frac{\epsilon\zeta}{\mu} + c\right) \overrightarrow{E}(\overrightarrow{r}_1) \\ \dot{\overrightarrow{r}}_2 = \left(-\frac{\epsilon\zeta}{\mu} + c\right) \overrightarrow{E}(\overrightarrow{r}_2) \\ \vdots \\ \dot{\overrightarrow{r}}_m = \left(-\frac{\epsilon\zeta}{\mu} + c\right) \overrightarrow{E}(\overrightarrow{r}_m) \end{bmatrix}. \tag{2.55}$$

Since electric fields are superposable, $\overrightarrow{E}$ can be expressed as a linear combination of n modes, where the i^{th} mode is defined as the electric field generated when the i^{th} electrode is set to 1V and the rest are set to 0V i.e. $\gamma_i = 1\text{V}$ and $\gamma_j = 0$ $(\forall j \neq i)$. This is expressed as

$$\overrightarrow{E}(\overrightarrow{r}) = \begin{bmatrix} \overrightarrow{E}_1(\overrightarrow{r}) & \overrightarrow{E}_2(\overrightarrow{r}) & .. & \overrightarrow{E}_n(\overrightarrow{r}) \end{bmatrix} \begin{bmatrix} \gamma_1 \\ \gamma_2 \\ \vdots \\ \gamma_n \end{bmatrix}. \tag{2.56}$$

Now, since voltage vectors $\begin{bmatrix} \gamma_1 & \gamma_2 & .. & \gamma_n \end{bmatrix}^T$ and $\begin{bmatrix} \gamma_1 + \alpha & \gamma_2 + \alpha & .. & \gamma_n + \alpha \end{bmatrix}^T$ would produce the exact same electric field, it is always possible to adjust the voltages such that $\gamma_n = 0$, or we say that γ_n is set to ground. Hence, any possible electric field is can be expressed as a linear combination of only $n-1$ modes. This is expressed by

$$\overrightarrow{E}(\overrightarrow{r}) = \begin{bmatrix} \overrightarrow{E}_1(\overrightarrow{r}) & \overrightarrow{E}_2(\overrightarrow{r}) & .. & \overrightarrow{E}_{n-1}(\overrightarrow{r}) \end{bmatrix} \begin{bmatrix} \gamma_1 \\ \gamma_2 \\ \vdots \\ \gamma_{n-1} \end{bmatrix}. \tag{2.57}$$

Substituting equation (2.57) in (2.55) we have the equations governing motion of a system of particles:

$$\begin{bmatrix} \dot{\overrightarrow{r}}_1 \\ \dot{\overrightarrow{r}}_2 \\ : \\ \dot{\overrightarrow{r}}_m \end{bmatrix} = \left(-\frac{\epsilon\zeta}{\mu} + c\right) \begin{bmatrix} \overrightarrow{E}_1(\overrightarrow{r}_1) & \overrightarrow{E}_2(\overrightarrow{r}_1) & .. & \overrightarrow{E}_{n-1}(\overrightarrow{r}_1) \\ \overrightarrow{E}_1(\overrightarrow{r}_2) & \overrightarrow{E}_2(\overrightarrow{r}_2) & .. & \overrightarrow{E}_{n-1}(\overrightarrow{r}_2) \\ : & : & : & : \\ \overrightarrow{E}_1(\overrightarrow{r}_m) & \overrightarrow{E}_2(\overrightarrow{r}_m) & .. & \overrightarrow{E}_{n-1}(\overrightarrow{r}_m) \end{bmatrix} \begin{bmatrix} \gamma_1 \\ \gamma_2 \\ : \\ \gamma_{n-1} \end{bmatrix}, \tag{2.58}$$

which can be expressed more concisely as

$$\dot{\overrightarrow{r}} = A(\overrightarrow{r})\overrightarrow{\gamma}, \tag{2.59}$$

where

$$\overrightarrow{r} = \begin{bmatrix} \overrightarrow{r}_1 \\ \overrightarrow{r}_2 \\ : \\ \overrightarrow{r}_m \end{bmatrix}, \tag{2.60}$$

$$A(\overrightarrow{r}) = \left(-\frac{\epsilon\zeta}{\mu} + c\right) \begin{bmatrix} \overrightarrow{E}_1(\overrightarrow{r}_1) & \overrightarrow{E}_2(\overrightarrow{r}_1) & .. & \overrightarrow{E}_{n-1}(\overrightarrow{r}_1) \\ \overrightarrow{E}_1(\overrightarrow{r}_2) & \overrightarrow{E}_2(\overrightarrow{r}_2) & .. & \overrightarrow{E}_{n-1}(\overrightarrow{r}_2) \\ : & : & : & : \\ \overrightarrow{E}_1(\overrightarrow{r}_m) & \overrightarrow{E}_2(\overrightarrow{r}_m) & .. & \overrightarrow{E}_{n-1}(\overrightarrow{r}_m) \end{bmatrix}, \tag{2.61}$$

and

$$\overrightarrow{\gamma} = \begin{bmatrix} \gamma_1 \\ \gamma_2 \\ : \\ \gamma_{n-1} \end{bmatrix}. \tag{2.62}$$

Chapter 3

Controller Design

In this chapter, we look at the design of control logic to steer particles along desired trajectories. Section 3.1 provides the derivation of the feedback control law for the nominal system. Section 3.2 analyzes degradation of tracking performance of the controller in the presence of system uncertainties. Section 3.3 presents some simulation results and section 3.4 provides explanations for addressing important questions about loss of control in certain situations.

3.1 Designing a Controller for the Nominal System

Fig. 3.1 shows the basic components for multiple particle control: the microfluidic device, a camera, and a computer with a control algorithm are connected in a feedback loop. The camera registers the position of the particles in real time, the computer compares the current position of the particles with the desired particle position, and the control algorithm then computes the necessary actuator voltages that will create the fluid flow to carry the particles to their desired position. These voltages are immediately applied at the electrodes in the microfluidic device. This process is repeated 20 times every second. The following theorem gives the feedback control law for the nominal system.

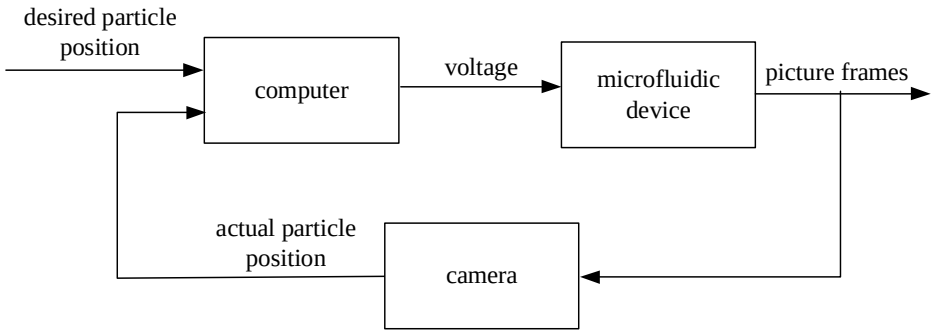

Figure 3.1: Block diagram for the feedback control of multiple particles in the microfluidic device.

Theorem 1 *Consider a set of particles, whose motion is described by the system*

$$\dot{\overrightarrow{r}} = A(\overrightarrow{r})\overrightarrow{\gamma}, \tag{3.1}$$

with given initial condition

$$\overrightarrow{r}(0) = \overrightarrow{r}_0, \tag{3.2}$$

where $\overrightarrow{r} = \begin{bmatrix} \overrightarrow{r}_1 & \overrightarrow{r}_2 & .. & \overrightarrow{r}_m \end{bmatrix}^T \in D_1$ *is the vector of particle positions,* $D_1 \subset \mathbb{R}^{2m}$ *is a domain covering the control area of the device,* $\overrightarrow{\gamma} \in \mathbb{R}^{n-1}$*is the control voltage vector,* $A : D_1 \rightarrow \mathbb{R}^{2m\times(n-1)}$ *is a smooth function on domain* D_1*,* m *is the number of particles and* n *is the number of electrodes. The desired particle trajectory is* $\overrightarrow{r}_d$ *where* $\overrightarrow{r}_d \in D_1$*. Then, the feedback control law*

$$\overrightarrow{\gamma} = A^{\ddagger}(\overrightarrow{r})(\dot{\overrightarrow{r}}_d - k\overrightarrow{e}), \tag{3.3}$$

where $A^{\ddagger}(\overrightarrow{r})$ *is the pseudo-inverse of matrix* $A(\overrightarrow{r})$ *and follows the relation [29]*

$$A^{\ddagger}(\overrightarrow{r}) = A^T(\overrightarrow{r})(A(\overrightarrow{r})A^T(\overrightarrow{r}))^{-1}, \tag{3.4}$$

$\overrightarrow{e} = \overrightarrow{r} - \overrightarrow{r}_d$ *is the tracking error, and* k *is the controller gain, ensures that the tracking error* $\overrightarrow{e}$ *exponentially decays to zero with time.*

Proof. Applying the feedback law (3.3) to the system (3.1) the closed loop dynamics are described as

$$\dot{\overrightarrow{r}} = A(\overrightarrow{r})A^{\ddagger}(\overrightarrow{r})(\dot{\overrightarrow{r}}_d - k\overrightarrow{e}), \tag{3.5}$$

Substituting equation (3.4) in equation (3.5) we have

$$\dot{\overrightarrow{r}} = A(\overrightarrow{r})A^{T}(\overrightarrow{r})(A(\overrightarrow{r})A^{T}(\overrightarrow{r}))^{-1}(\dot{\overrightarrow{r}}_d - k\overrightarrow{e}), \tag{3.6}$$

$$\Longrightarrow \dot{\overrightarrow{r}} = A(\overrightarrow{r})A^{T}(\overrightarrow{r})(A^{T}(\overrightarrow{r}))^{-1}(A(\overrightarrow{r}))^{-1}(\dot{\overrightarrow{r}}_d - k\overrightarrow{e}), \tag{3.7}$$

$$\Longrightarrow \dot{\overrightarrow{r}} = \dot{\overrightarrow{r}}_d - k\overrightarrow{e}, \tag{3.8}$$

which simplifies to

$$\dot{\overrightarrow{e}} = -k\overrightarrow{e}. \tag{3.9}$$

Hence the feedback control law (3.3) ensures that the tracking error exponentially decays to zero with time. ■

Note: The pseudo-inverse of a fat matrix A is defined by [29]

$$A^{\ddagger} = A^{T}(AA^{T})^{-1}, \tag{3.10}$$

inverts the non-invertible matrix A as best as possible and has the following properties:

- The least norm solution of the linear system $y = Ax$ is given by $x = A^{\ddagger}y$.
- $AA^{\ddagger} = I$.

The feedback control law

$$\overrightarrow{\gamma} = A^{\ddagger}(\overrightarrow{r})(\dot{\overrightarrow{r}}_d - k\overrightarrow{e}), \tag{3.11}$$

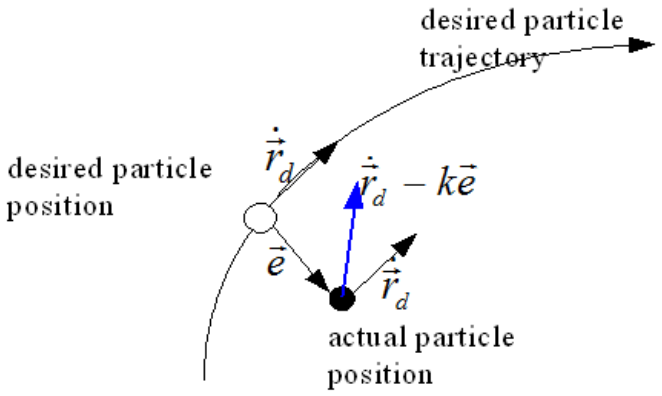

Figure 3.2: The desired and actual particle positions are denoted by the black hollow and solid circles, respectively. The various vectors denoting desired particle velocity and error are as indicated. The controller creates a particle velocity of $\dot{\overrightarrow{r}}_d - k\overrightarrow{e}$, which, as we can see, pushes the particle towards the desired trajectory.

can be interpreted as producing $\overrightarrow{\gamma}$, the most efficient solution (least norm solution) from a set of all possible voltages that will move particles at position $\overrightarrow{r}$ with velocity $(\dot{\overrightarrow{r}}_d - k\overrightarrow{e})$. As seen from the Fig. 3.2, this makes intuitive sense, as this pushes the particles towards the desired trajectory.

3.2 Degradation in Controller Performance due to System Uncertainties

The previous section provided a feedback control law for the nominal system. In reality, however, there are several sources that introduce uncertainty in particle velocities and affect tracking performance. Electrophoresis, Brownian motion, and pressure driven flow (as pointed out in the final section of chapter 2) all contribute

to uncertainty in particle motion. In addition, distortions in device geometry due to fabrication tolerances and uncertainties in zeta potential value also contribute to distortion of the nominal flow field. In our model, we assume that the polystyrene beads move along with the flow, but in experiments, we often observed that the particles encounter friction with the top and the bottom channel surfaces. The following theorem provides a numerical bounds and convergence rate for the tracking error in the presence of such uncertainties.

Theorem 2 *Consider the system described by*

$$\dot{\overrightarrow{r}} = [A(\overrightarrow{r}) + \delta_1(\overrightarrow{r}, t)]\overrightarrow{\gamma}(t) + \delta_2(\overrightarrow{r}, t) \tag{3.12}$$

with given initial condition

$$\overrightarrow{r}(0) = \overrightarrow{r}_0, \tag{3.13}$$

where $\overrightarrow{r} \in D_1$ *is the vector of particle positions,*$D_1 \subset \mathbb{R}^{2m}$ *is a domain such that* $\overrightarrow{r}_i \in D_{device}$ *(*D_{device} *is the domain covering the control area of the device),* $\overrightarrow{\gamma} \in \mathbb{R}^{n-1}$ *is the control voltage vector,* $A : D_1 \rightarrow \mathbb{R}^{2m\times(n-1)}$ *is a smooth function on domain* D_1*,* m *is the number of particles,* n *is the number of electrodes,* δ_1*is the deviation of the real map from the nominal map* A *due to distortions in device geometry and uncertainties in zeta potential value,* $\overrightarrow{\delta_2}$ *is the vector of parasitic pressure, electrophoretic, Brownian motion, and friction velocities that are superposed on top of the electroosmotic particle velocities.*

(a) *Then the feedback control law*

$$\overrightarrow{\gamma} = A^{\ddagger}(\overrightarrow{r})(\dot{\overrightarrow{r}}_d - k\overrightarrow{e}) \tag{3.14}$$

ensures that the norm of the tracking error $\|\overrightarrow{e}\|_2$ *is ultimately bound by* $\Delta_m/\lambda_{K\min}$ *where*

$$\overrightarrow{\delta}(t, \overrightarrow{r}, \overrightarrow{\gamma}) = \delta_1(\overrightarrow{r}, t)A^{\ddagger}(\overrightarrow{r})\dot{\overrightarrow{r}}_d + \delta_2(\overrightarrow{r}, t), \tag{3.15}$$

$$K = k(1 + \delta_1(\overrightarrow{r}, t)A^{\ddagger}(\overrightarrow{r})), \tag{3.16}$$

$$\left\|\overrightarrow{\delta}(t, \overrightarrow{r}, \overrightarrow{\gamma})\right\|_2 < \Delta_m \tag{3.17}$$

and K *is positive definite with its smallest eigenvalue given by* $\lambda_{K\min}$.

(b) *Further the convergence of* $\|\overrightarrow{e}\|_2$ *is bounded by an exponentially decaying function such that*

$$\|\overrightarrow{e}(t)\|_2 < (\|\overrightarrow{e}(0)\|_2 - \frac{\Delta_m}{\lambda_{K\min}})\exp(-kt) + \frac{\Delta_m}{\lambda_{K\min}} \tag{3.18}$$

$\forall t \geq 0$.

Proof.

(a) *Consider the system*

$$\dot{\overrightarrow{r}} = [A(\overrightarrow{r}) + \delta_1(\overrightarrow{r}, t)]\overrightarrow{\gamma}(t) + \overrightarrow{\delta}_2(\overrightarrow{r}, t), \tag{3.19}$$

applying the feedback control law (3.14) the closed loop dynamics are given by

$$\dot{\overrightarrow{r}} = A(\overrightarrow{r})(A^{\ddagger}(\overrightarrow{r})(\dot{\overrightarrow{r}}_d - k\overrightarrow{e}) + \overrightarrow{\delta}(t, \overrightarrow{r}, \overrightarrow{\gamma}), \tag{3.20}$$

which simplifies to

$$\dot{\overrightarrow{e}} = -K\overrightarrow{e} + \overrightarrow{\delta}(t, \overrightarrow{r}, \overrightarrow{\gamma}). \tag{3.21}$$

Considering the Lyapunov function candidate

$$V = \frac{1}{2}\overrightarrow{e}^T\overrightarrow{e} \tag{3.22}$$

for the system (3.21) and taking its time derivative we have

$$\dot{V} = \overrightarrow{e}^T \dot{\overrightarrow{e}}. \tag{3.23}$$

Substituting equation (3.21) in equation (3.23) we have

$$\dot{V} = \overrightarrow{e}^T(-K\overrightarrow{e} + \overrightarrow{\delta}(t, \overrightarrow{r}, \overrightarrow{\gamma})), \tag{3.24}$$

$$\Longrightarrow \dot{V} = -\overrightarrow{e}^T K\overrightarrow{e} + \overrightarrow{e}^T\overrightarrow{\delta}(t, \overrightarrow{r}, \overrightarrow{\gamma}), \tag{3.25}$$

$$\Longrightarrow \dot{V} \leq -\lambda_{K\min} \|\overrightarrow{e}\|_2^2 + \|\overrightarrow{e}\|_2 \left\|\overrightarrow{\delta}(t, \overrightarrow{r}, \overrightarrow{\gamma})\right\|_2, \tag{3.26}$$

$$\Longrightarrow \dot{V} < -\lambda_{K\min} \|\overrightarrow{e}\|_2^2 + \|\overrightarrow{e}\|_2 \Delta_m, \tag{3.27}$$

$$\Longrightarrow \dot{V} < 0 \quad \forall \|\overrightarrow{e}\|_2 > \frac{\Delta_m}{\lambda_{K\min}}. \tag{3.28}$$

Hence $\|\overrightarrow{e}\|_2$ *is ultimately bound by* $\Delta_m/\lambda_{K\min}$.

(b) *To obtain an estimate on the convergence of* $\|\overrightarrow{e}\|_2$, *we first consider the rate of decay of the Lyapunov function*

$$\dot{V} = \frac{d}{dt}(\frac{1}{2}\overrightarrow{e}^T\overrightarrow{e}) \tag{3.29}$$

$$\Longrightarrow \dot{V} = \frac{d}{dt}(\frac{1}{2}\|\overrightarrow{e}\|_2^2) \tag{3.30}$$

$$\Longrightarrow \dot{V} = \|\overrightarrow{e}\|_2 \|\dot{\overrightarrow{e}}\|_2 \tag{3.31}$$

Comparing equations (3.27) and (3.31) we have

$$\|\overrightarrow{e}\|_2 \|\dot{\overrightarrow{e}}\|_2 < -\lambda_{K\min} \|\overrightarrow{e}\|_2^2 + \|\overrightarrow{e}\|_2 \Delta_m \tag{3.32}$$

$$\Longrightarrow \|\dot{\overrightarrow{e}}\|_2 < -\lambda_{K\min} \|\overrightarrow{e}\|_2 + \Delta_m. \tag{3.33}$$

The solution of which yields [30]

$$\|\overrightarrow{e}(t)\|_2 < (\|\overrightarrow{e}(0)\|_2 - \frac{\Delta_m}{\lambda_{K\min}}) \exp(-\lambda_{K\min} t) + \frac{\Delta_m}{\lambda_{K\min}}. \tag{3.34}$$

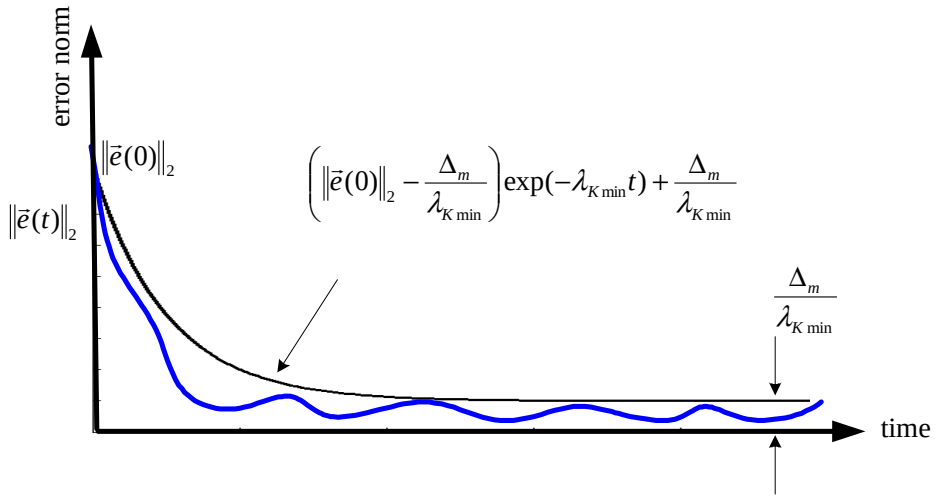

Figure 3.3: The particle tracking error norm (blue curve) in the presence of system uncertainties is bounded between the exponentially decaying curve (marked in black). The ultimate bound is given by $\Delta_m/\lambda_{K\min}$.

■

Fig. (3.3) illustrates that the error norm is bound by the exponentially decaying function given by equation (3.34).

3.3 Simulation Results

This section presents COMSOL/MATLAB simulation results for the control of one, two, and three particles. To simulate experimental conditions we considered:

- A twelve channel device geometry, similar to that used in experiments. Incoming radial channels were 25 microns wide, 10 microns deep, and the central control area was about 125 microns in diameter

- A mild parasitic pressure driven flow with a magnitude of around 10 microns/s at particle positions
- A 10% uncertainty in the estimation of zeta potential
- Minor distortions in the device geometry of ± 5 microns at arbitrary locations
- Brownian noise with an average particle displacement of 0.15 microns per control voltage update time step
- Control voltage was updated 20 times a second

3.4 Explaining Two Important Observations

We could only apply voltages in the range $+10$V to -10V to the electrodes. Higher voltages led to electrochemical reactions at the electrodes, disturbing the control and complicating the physics of the problem. Overall, we encountered two effects that put serious limits on the steering capability of the device.

1. As particles came close to each other, the voltages computed by the controller rose sharply, saturating the actuators, making control impossible.
2. As the number of particles to be steered was increased, the maximum speed at which the particles could be steered dropped drastically. The drop was so dramatic, that when attempting to steer more than three particles, the electroosmotic flow was insufficient to overcome even the mildest parasitic pressure-driven flows that existed in the device at all times - leading to loss of control.

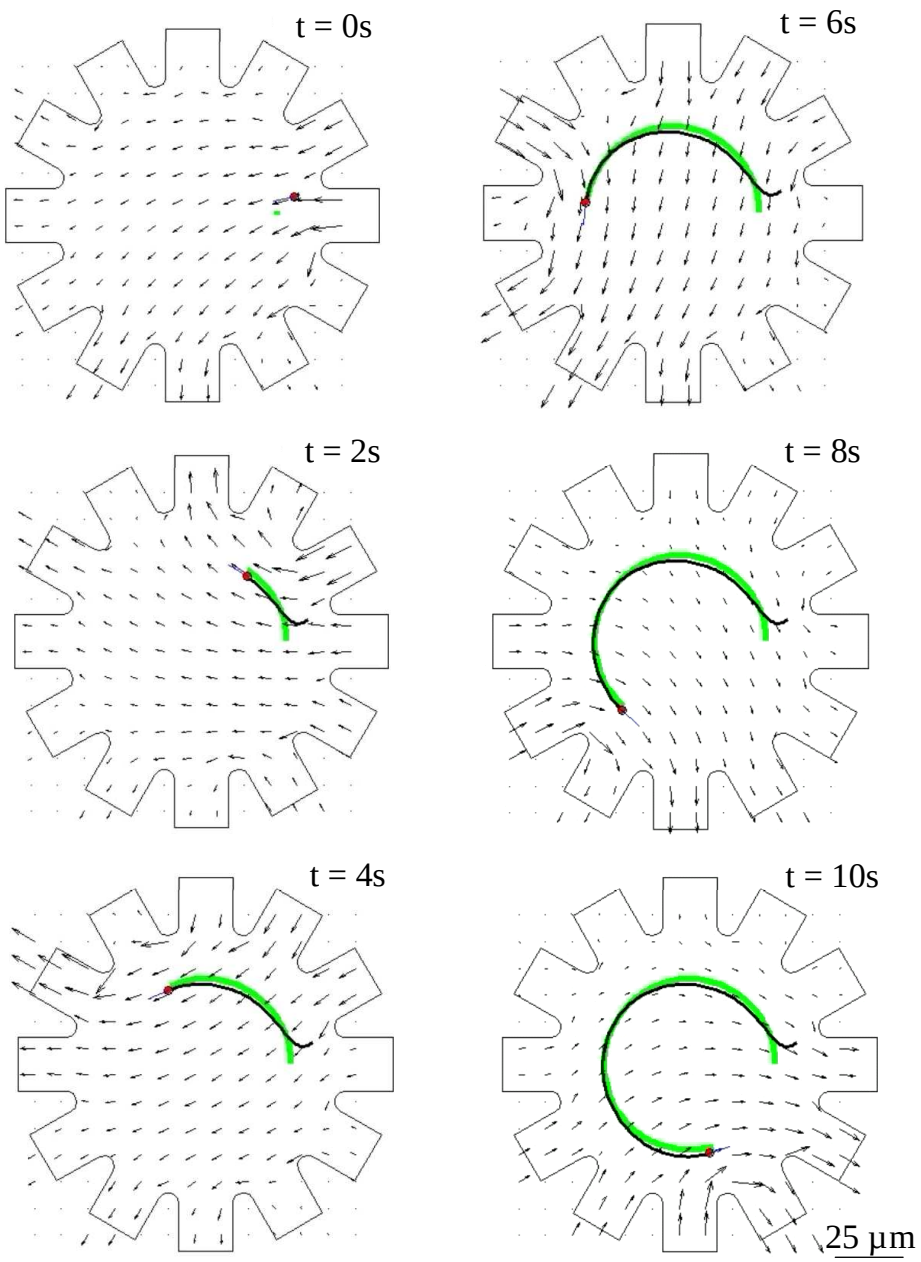

Figure 3.4: This figure shows a single particle steering simulation results for a twelve channel microfluidic device. The thick green lines indicate the desired particle trajectory. The thin black lines indicate the actual particle trajectory. A mild parasitic pressure flow, distortions in device geometry, uncertainty in estimation on zeta potential values, and Brownian motion are considered in the simulation.

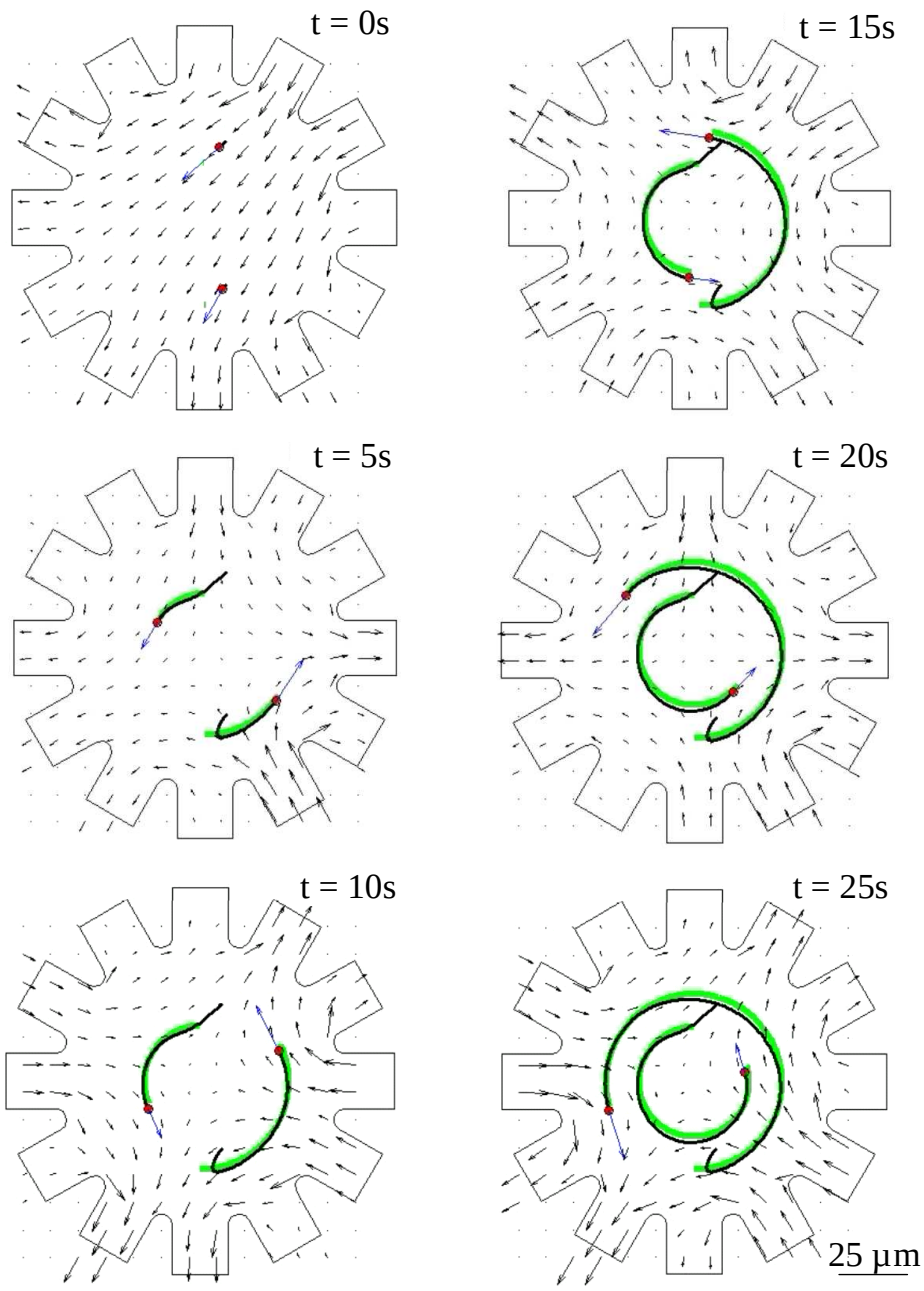

Figure 3.5: This figure shows a two-particle steering simulation results for a twelve channel microfluidic device. The thick green lines indicate the desired particle trajectory. The thin black lines indicate the actual particle trajectory. A mild parasitic pressure flow, distortions in device geometry, uncertainty in estimation on zeta potential values, and Brownian motion are considered in the simulation.

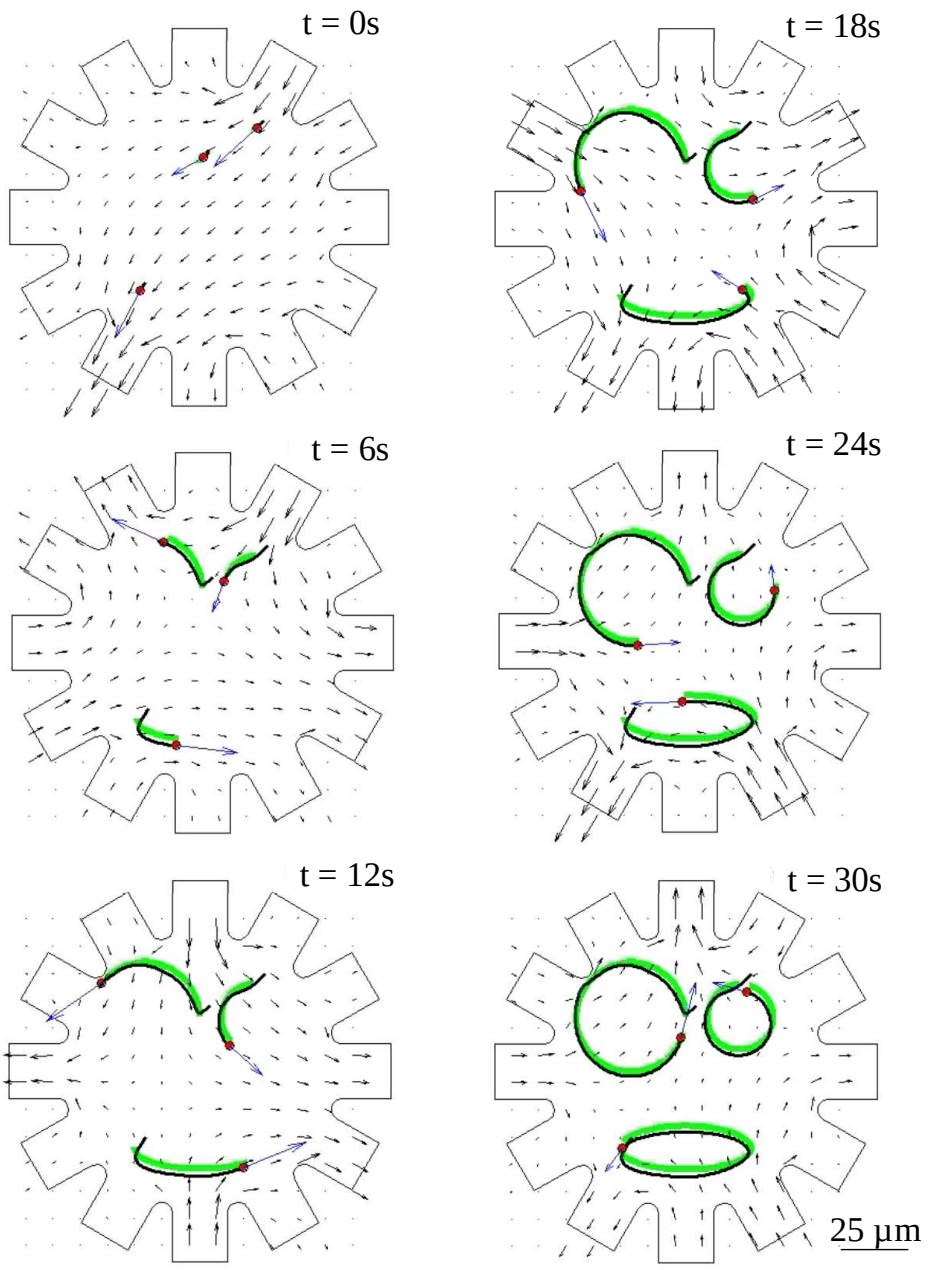

Figure 3.6: This figure shows a three-particle steering simulation results for a twelve channel microfluidic device. The thick green lines indicate the desired particle trajectory. The thin black lines indicate the actual particle trajectory. A mild parasitic pressure flow, distortions in device geometry, uncertainty in estimation on zeta potential values, and Brownian motion are considered in the simulation.

As a result, initially we could only demonstrate steering of up to three particles. Additionally, we had to ensure that no two particles came very close to each other at any time during the particle steering process. Manually designing such paths was extremely tedious. In order to achieve our objective of demonstrating steering of up to 5 particles, it was necessary to first understand the reasons for this system behavior and then identify ways of avoiding or changing this behavior. In this section, we explain the cause. In chapters 4 and 5 we elaborate on ways of avoiding/changing this behavior.

In the first subsection, we will express the voltage vector in terms of the singular values of the A matrix. In the second and third subsection, we will use this expression and an understanding of the change in the singular values of A in response to changes in particle configurations and to changes in particle numbers to explain the two observations mentioned earlier.

3.4.1 Expressing the Controller Voltage in Terms of the Singular Values of Matrix A

Consider a set of particles at positions $\overrightarrow{r}_g$ and say we wish to actuate the particles with velocities $\dot{\overrightarrow{r}}_D$. The equations governing particle motion are then given by the linear equation

$$\dot{\overrightarrow{r}}_D = A(\overrightarrow{r}_g)\overrightarrow{\gamma}. \tag{3.35}$$

This equation is now expressed in terms of its standard basis. Without loss of generality, it can also be expressed in terms of its singular value basis. The singular

value basis is obtained by considering the SVD decomposition of the matrix $A_g = A(\overrightarrow{r}_g)$ as shown.

$$A_g = Q\Sigma W^T = \begin{bmatrix} \overrightarrow{q}_1 & \overrightarrow{q}_2 & .. & \overrightarrow{q}_{n-1} \end{bmatrix} \begin{bmatrix} \sigma_1 & 0 & 0 & 0 \\ 0 & \sigma_2 & 0 & 0 \\ 0 & 0 & \ddots & 0 \\ 0 & 0 & 0 & \sigma_{n-1} \end{bmatrix} \begin{bmatrix} \overrightarrow{w}_1^T \\ : \\ : \\ \overrightarrow{w}_{n-1}^T \end{bmatrix}. \quad (3.36)$$

The input and output basis vectors for the standard and singular value basis is shown in the table below.

	Standard basis	Singular Value basis
Normalized input vectors (voltage)	$\begin{bmatrix}1\\0\\:\\0\end{bmatrix}, \begin{bmatrix}0\\1\\:\\0\end{bmatrix}, ..., \begin{bmatrix}0\\0\\:\\1\end{bmatrix}$	$\overrightarrow{w}_1, \overrightarrow{w}_2, ..., \overrightarrow{w}_{n-1}$
Normalized output vectors (particle vector)	$\frac{1}{\|A_{g1}\|}A_{g1}, \frac{1}{\|A_{g2}\|}A_{g2}, ..$ ($n-1$ vectors) $A_{g(i)}$ is i^{th} column of A_g	$\overrightarrow{q}_1, \overrightarrow{q}_2, ..., \overrightarrow{q}_{n-1}$
Relation between input & output vectors	$A_g \begin{bmatrix}0\\:\\1\\:\\0\end{bmatrix} = A_{g(i)}$ Here the input vector has a 1 at the i^{th} position	$A_g \overrightarrow{w}_i = \sigma_i \overrightarrow{q}_i$ (see Appendix A)

When expressed in terms of the standard basis, we can physically interpret the equation (3.35) as: *The desired particle velocities can be obtained by linearly combining $n-1$ fluid modes, as shown in the upper half of Fig. 3.7.* When expressed in terms of the singular value basis, the equation (3.35) can be physically interpreted as: *The desired particle velocities can be obtained by linearly combining $n-1$ singular value fluid modes, as shown in the upper half of Fig. 3.7.* The i^{th} singular value

fluid mode is obtained by applying the voltage vector $\overrightarrow{w}_i$ to the electrodes.

The controller voltage

$$\overrightarrow{\gamma} = A_g^T (A_g A_g^T)^{-1} \dot{\overrightarrow{r}}_D \tag{3.37}$$

which also corresponds to the least norm solution to equation (3.35), is obtained by linearly combining only the first $2m$ singular value fluid modes (Refer to subsection (3.4.4) for a rigorous mathematical proof.). Let $c_1, c_2, ..., c_{2m}$ be the components of the voltage vector $\overrightarrow{\gamma}$ along the singular value input basis. Therefore,

$$\overrightarrow{\gamma} = c_1 \overrightarrow{w}_1 + c_2 \overrightarrow{w}_2 + ... + c_{2m} \overrightarrow{w}_{2m}. \tag{3.38}$$

Let $a_1, a_2, ..., a_{2m}$ be the components of the particle velocity vector $\dot{\overrightarrow{r}}_D$ along the singular value output basis. Therefore,

$$\dot{\overrightarrow{r}}_D = a_1 q_1 + a_2 q_2 + ... + a_{2m} q_{2m}. \tag{3.39}$$

Substituting (3.38) and (3.39) in (3.35) and using the identity $A_g \overrightarrow{w}_i = \sigma_i \overrightarrow{q}_i$, we get

$$\sum a_i q_i = \sum c_i \sigma_i q_i. \tag{3.40}$$

Comparing coefficients of q_i we have

$$c_i = \frac{a_i}{\sigma_i}. \tag{3.41}$$

Substituting (3.41) in (3.38) we get

$$\overrightarrow{\gamma} = \frac{a_1}{\sigma_1} \overrightarrow{w}_1 + \frac{a_2}{\sigma_2} \overrightarrow{w}_2 + ... + \frac{a_{2m}}{\sigma_{2m}} \overrightarrow{w}_{2m}. \tag{3.42}$$

In general we expect a_i to be of the same order of magnitude $O(a)$, hence

$$\overrightarrow{\gamma} \approx \frac{O(a)}{\sigma_1} \left(\overrightarrow{w}_1 + \frac{\sigma_1}{\sigma 2} \overrightarrow{w}_2 + ... + \frac{\sigma_1}{\sigma_{2m}} \overrightarrow{w}_{2m} \right). \tag{3.43}$$

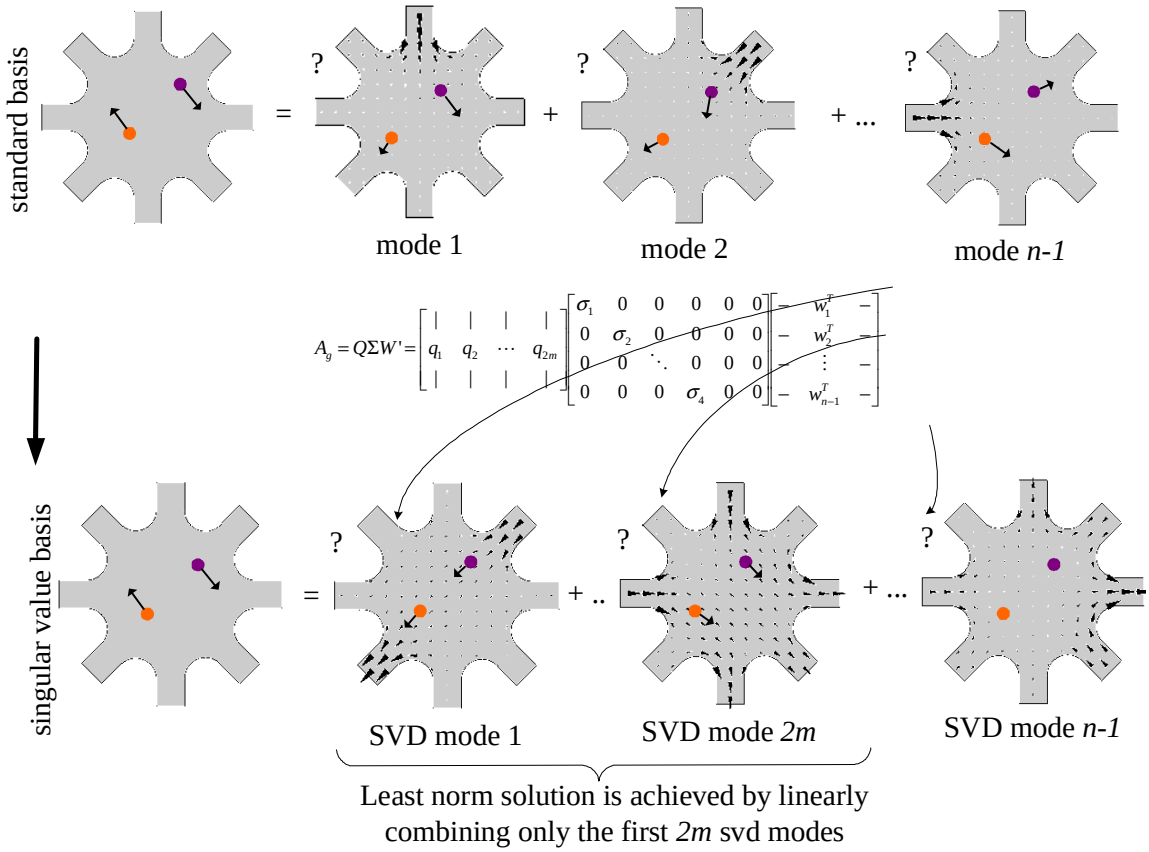

Figure 3.7: Desired particle velocities can be obtained by linearly combining $n-1$ fluid modes, as shown in the upper half of the figure. Without loss of generality, the particle velocities can also be obtained by linearly combining the $n-1$ singular value modes, as shown in the lower half of the figure. The least norm voltage solution to obtain the desired particle velocities is acquired by linearly combining only the first $2m$ singular value modes.

In the following subsections we will use this expression to explain the two observations mentioned earlier.

3.4.2 Explaining Sharp Rise in Control Voltage when Particles Approach Each Other

Two scenarios are shown in Fig. 3.8: one is for two particles that are further away from each other and the other is for particles closer to each other. The A_g matrix corresponding to each scenario is shown on the right. The reader will recall that the rows of the A matrix are such that the first and third rows represent the x velocity component of the first and second particle respectively for all fluid modes $i = 1, 2, ..n$. The second and fourth rows represent the y velocity component of the first and second particles respectively for fluid modes $i = 1, 2, ..n$. For the first scenario the four rows in general would represent four linearly independent vectors. As the particles come closer to each other as shown in the second scenario, the first row becomes similar to the third row and the second row becomes similar to the fourth row. Consequently, the A_g matrix tends towards having only two linearly independent rows. In terms of singular values, this means that as the two particles come closer to each other, the last two singular values progressively tend to zero. Therefore $\sigma_1/\sigma_3 \to \infty$ and $\sigma_1/\sigma_4 \to \infty$, consequently the voltage expression

$$\overrightarrow{\gamma} \approx \frac{O(a)}{\sigma_1}\left(\overrightarrow{w}_1 + \frac{\sigma_1}{\sigma 2}\overrightarrow{w}_2 + \frac{\sigma_1}{\sigma_3}\overrightarrow{w}_3 + \frac{\sigma_1}{\sigma_4}\overrightarrow{w}_4\right) \to \infty, \tag{3.44}$$

saturating the actuators and leading to loss of control capability. This reflects a fundamental property of the system: two particles close together see a similar fluid

flow and steering them apart is difficult.

3.4.3 Explaining the Rapid Decrease in Maximum Particle Steering Speed as the Number of Particles Increases

Fig. 3.9 shows, for a typical case, the maximum particle steering speed and singular values of the A_g matrix as the number of particles increase. We see that the smallest singular value drops rapidly with increase in the number of particles. Consequently, the terms σ_1/σ_i towards the extreme right in the voltage expression

$$\overrightarrow{\gamma} \approx \frac{O(a)}{\sigma_1}\left(\overrightarrow{w}_1 + \frac{\sigma_1}{\sigma 2}\overrightarrow{w}_2 + ... + \frac{\sigma_1}{\sigma_{2m-1}}\overrightarrow{w}_{2m-1} + \frac{\sigma_1}{\sigma_{2m}}\overrightarrow{w}_{2m}\right) \tag{3.45}$$

rapidly rise in magnitude. Conversely, given a limit of $\pm 10V$ on each electrode the maximum particle steering speed falls rapidly as the number of particles increases. As shown in Fig. 3.9, the maximum electroosmotic particle actuation speed for four and five particles is much lower than the mild parasitic pressure flow that always exists in the device, and hence we were unable to steer more than three particles.

3.4.4 Rigorous Mathematical Treatment for the Physical Interpretation of Controller

In subsection (3.4.1) we had used the fact that the least norm solution to the system equation

$$\dot{\overrightarrow{r}}_D = A_g \overrightarrow{\gamma} \tag{3.46}$$

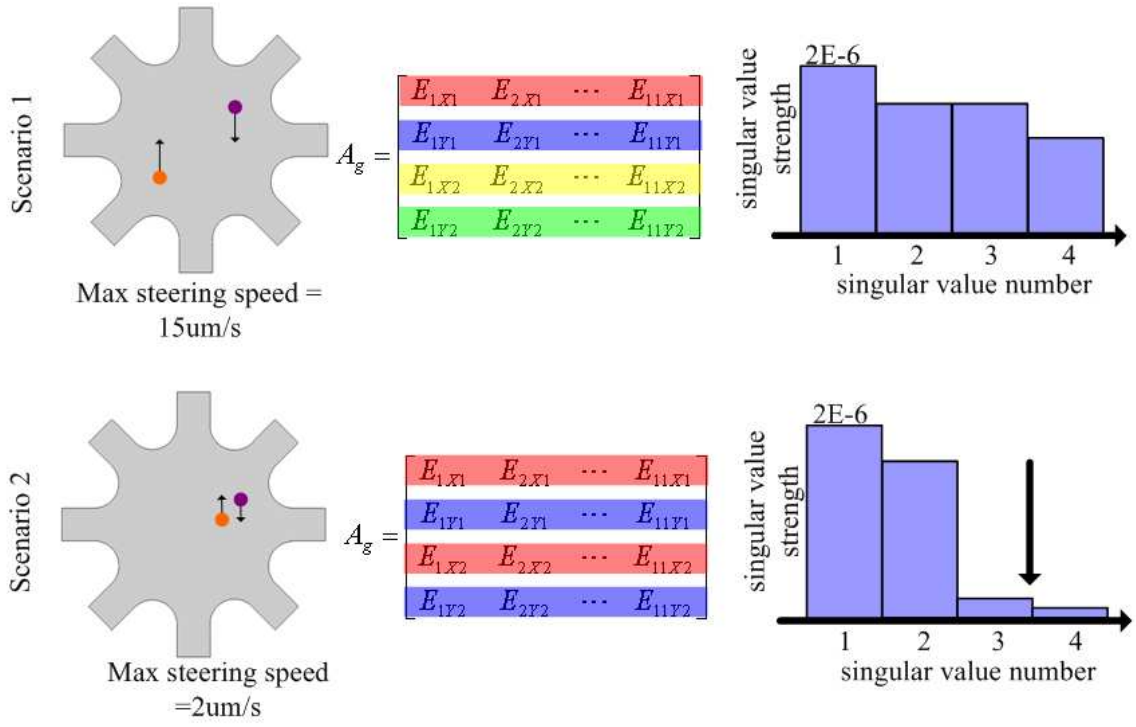

Figure 3.8: Scenario 1 represents a situation when the two particles being steered are far away from each other, and scenario 2 represents a situation when the particles are closer to each other. The A_g matrix and its singular values corresponding to each scenario are shown on the right. For scenario 1 the four rows in general would represent four linearly independent vectors. This is illustrated by each of the four rows highlighted by different colors. As the particles come closer to each other, as shown in scenario 2, the first row becomes similar to the third row and the second row becomes similar to the fourth row. This is illustrated by the first and third rows highlighted by the same color and the second and fourth rows highlighted by the same color. Consequently, the A_g matrix leans towards having only two linearly independent rows. In terms of singular values, this means that as the two particles come closer to each other, the last two singular values progressively tend to zero.

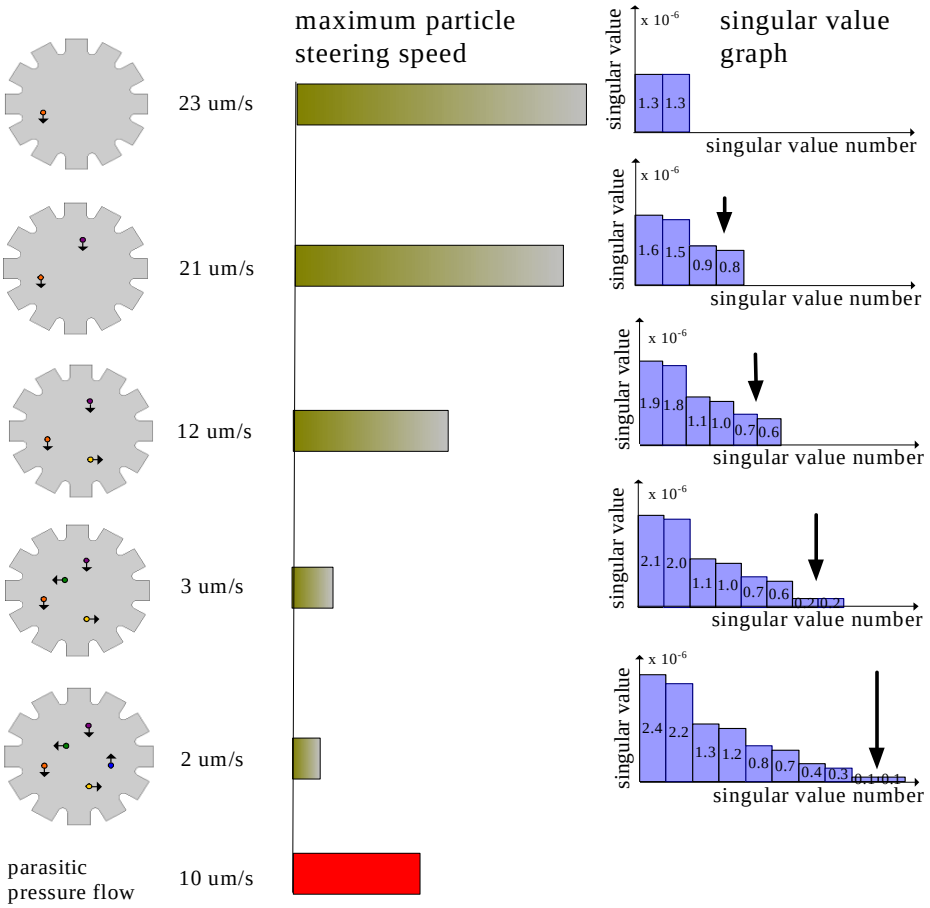

Figure 3.9: This figure shows, for a typical case, the maximum particle steering speed and singular values of the A matrix as the number of particles increase. For greater than three particles, the maximum particle steering speed is much lower than the mild parasitic pressure flow that always exists in the device; hence the inability to steer more than three particles with the existing setup. The singular values of the A matrix corresponding to each case are also given. The lower singular value modes introduce progressively larger voltage components in the control voltage solution. Conversely, with a maximum limit of ± 10 V on the actuation voltages, the maximum particle steering speed drops rapidly with an increase in the number of particles.

is obtained by combining only the first $2m$ singular value output basis vectors or fluid modes, and that it is given by the expression

$$\overrightarrow{\gamma}_l = A_g^T (A_g A_g^T)^{-1} \dot{\overrightarrow{r}}_D. \tag{3.47}$$

This section, provides a mathematical proof [29].

Theorem 3 *The nominal system equation (3.1) for a set of particles at a given position* $\overrightarrow{r} = \overrightarrow{r}_g$ *and for desired particle velocities* $\dot{\overrightarrow{r}} = \dot{\overrightarrow{r}}_D$ *is given by the linear system of simultaneous equations*

$$\dot{\overrightarrow{r}}_D = A_g \overrightarrow{\gamma} \tag{3.48}$$

where $A_g = A(\overrightarrow{r}_g)$ *and* $A_g \in \mathbb{R}^{2m \times (n-1)}$. *We only consider situations where* $2m < n-1$ *i.e. the number of particle degrees of freedom is less than the number of actuators. In this case,* A_g *is fat, i.e., there are more variables than equations,* $\overrightarrow{\gamma}$ *is underspecified and consequently system (3.48) has infinitely many solutions. Assume that* A_g *is full rank (rank(*A_g*)=2m). Let* $\overrightarrow{\gamma}$ *be any of the infinitely many solutions of system (3.48). Further, consider the singular value decomposition of* A_g

$$A_g = Q \Sigma W^T = \begin{bmatrix} \overrightarrow{q}_1 & \overrightarrow{q}_2 & .. & \overrightarrow{q}_{n-1} \end{bmatrix} \begin{bmatrix} \sigma_1 & 0 & 0 & 0 \\ 0 & \sigma_2 & 0 & 0 \\ 0 & 0 & \ddots & 0 \\ 0 & 0 & 0 & \sigma_{n-1} \end{bmatrix} \begin{bmatrix} \overrightarrow{w}_1^T \\ : \\ : \\ \overrightarrow{w}_{n-1}^T \end{bmatrix} \tag{3.49}$$

where $Q \in \mathbb{R}^{2m \times (n-1)}$, $W \in \mathbb{R}^{(n-1)\times(n-1)}$, $\Sigma \in \mathbb{R}^{(n-1)\times(n-1)}$ *and the vectors* $\overrightarrow{w}_i (i = 1, 2, .., n-1)$ *and* $\overrightarrow{q}_i (i = 1, 2, .., n-1)$ *satisfy [29]*

$$A_g \overrightarrow{w}_i = \sigma_i \overrightarrow{q}_i \tag{3.50}$$

$$\|\overrightarrow{w}_i\| = \|\overrightarrow{q}_i\| = 1. \tag{3.51}$$

(a) *The projection of* $\overrightarrow{\gamma}$ *in the subspace spanned by the first 2m input vectors* $\overrightarrow{w}_i$ *(i=1,2,..,2m) is also a solution of (3.48).*

(b) *All solutions of (3.48) have the same component along the first 2m input vectors* $\overrightarrow{w}_i$ *(i=1,2,..,2m).*

(c) *This component is the least norm solution of (3.48).*

(d) *The least norm solution of (3.48) is given by the formula* $\overrightarrow{\gamma}_l = A_g^T(A_g A_g^T)^{-1}\dot{\overrightarrow{r}}_d$.

Proof.

(a) From Appendix A [29], we see that the input vectors $\overrightarrow{w}_i$ $(i = 1, 2, .., n-1)$ are orthonormal, the first $2m$ input vectors $\overrightarrow{w}_i$ $(i = 1, 2, .., 2m)$ form the basis of the row space of A_g and the that the last $n-1-2m$ input vectors $\overrightarrow{w}_i$ $(i = 2m+1, .., n-1)$ form the basis of the null space of A_g.

Resolving $\overrightarrow{\gamma}$ into components along the row space $\overrightarrow{\gamma}_R$ and null space $\overrightarrow{\gamma}_N$ we get

$$\overrightarrow{\gamma} = \overrightarrow{\gamma}_R + \overrightarrow{\gamma}_N \tag{3.52}$$

Since $\overrightarrow{\gamma}_N$ is in the null space of A_g,

$$A_g(\overrightarrow{\gamma}_N) = 0 \tag{3.53}$$

Substituting (3.52) into (3.48) and using (3.53)we get

$$\dot{\overrightarrow{r}}_d = A_g\overrightarrow{\gamma} = A_g(\overrightarrow{\gamma}_R + \overrightarrow{\gamma}_N) = A_g\overrightarrow{\gamma}_R. \tag{3.54}$$

Hence, the projection of $\overrightarrow{\gamma}$ in the subspace spanned by the first $2m$ input vectors $\overrightarrow{w}_i$ $(i = 1, 2, .., 2m)$ is also a solution of (3.48).

(b) Let $\overrightarrow{\gamma}_1$ and $\overrightarrow{\gamma}_2$ be two solutions of (3.48) such that they have different components in the row space of A_g. Let $\overrightarrow{\gamma}_{1R}$ and $\overrightarrow{\gamma}_{2R}$ denote their components in the row space of A_g.Then from (a) we have that

$$A_g \overrightarrow{\gamma}_{1R} = \dot{\overrightarrow{r}}_D \tag{3.55}$$

and

$$A_g \overrightarrow{\gamma}_{2R} = \dot{\overrightarrow{r}}_D. \tag{3.56}$$

Subtracting (3.55) from (3.56) we get

$$A_g(\overrightarrow{\gamma}_{2R} - \overrightarrow{\gamma}_{1R}) = 0. \tag{3.57}$$

Hence, $\overrightarrow{\gamma}_{2R} - \overrightarrow{\gamma}_{1R}$ belongs to the null space of A_g. This is a contradiction since $\overrightarrow{\gamma}_{1R}$, $\overrightarrow{\gamma}_{2R}$ and all their linear combinations will also be in the row space of A_g. Hence all solutions of (3.48) have the same component in the row space of A_g.

(c) Let $\overrightarrow{\gamma}_{Rp}$ denote the row space component common in all solutions of (3.48). Any solution of (3.48) is then necessarily of the form

$$\overrightarrow{\gamma} = \overrightarrow{\gamma}_{Rp} + \overrightarrow{\phi}_N, \tag{3.58}$$

where $\overrightarrow{\phi}_N$ belongs to the null space of A_g. So given

$$\|\overrightarrow{\gamma}\|^2 = \|\overrightarrow{\gamma}_{Rp} + \phi_N\|^2 \geq \|\overrightarrow{\gamma}_{Rp}\|^2 + \|\phi_N\|^2, \tag{3.59}$$

$\overrightarrow{\gamma}$ has the lowest norm when $\overrightarrow{\phi}_N = 0$. Hence $\overrightarrow{\gamma}_{Rp}$ is the lowest norm solution of (3.48).

(d) From (c) we have that the lowest norm solution of (3.48) $\overrightarrow{\gamma}_l$ only has components in the row space of A_g. Hence

$$\overrightarrow{\gamma}_l = \sum_{i=1}^{2m} \overrightarrow{w}_i b_i, \tag{3.60}$$

for some scalar coefficients $b_i (i = 1, 2, .., 2m)$. Resolving $\overrightarrow{r}_D$ along output directions $q_i (i = 1, 2, .., 2m)$ we have that

$$\dot{\overrightarrow{r}}_D = \sum_{i=1}^{2m} (\overrightarrow{q}_i^T \dot{\overrightarrow{r}}_D) \overrightarrow{q}_i. \tag{3.61}$$

Substituting (3.60) and (3.61) in system equation (3.48) we get

$$\sum_{i=1}^{2m} (\overrightarrow{q}_i^T \dot{\overrightarrow{r}}_D) \overrightarrow{q}_i = A_g \sum_{i=1}^{2m} \overrightarrow{w}_i b_i. \tag{3.62}$$

Using the identity $A_g \overrightarrow{w}_i = \sigma_i \overrightarrow{q}_i$ from Appendix A we have that

$$\sum_{i=1}^{2m} (\overrightarrow{q}_i^T \dot{\overrightarrow{r}}_D) \overrightarrow{q}_i = \sum_{i=1}^{2m} \sigma_i \overrightarrow{q}_i b_i. \tag{3.63}$$

Comparing coefficients of q_i on both sides we have

$$b_i \sigma_i = (\overrightarrow{q}_i^T \dot{\overrightarrow{r}}_D). \tag{3.64}$$

Substituting (3.64) in (3.60) we get

$$\overrightarrow{\gamma}_l = \sum_{i=1}^{2m} \overrightarrow{w}_i b_i = \sum_{i=1}^{2m} \overrightarrow{w}_i \frac{1}{\sigma_i} \overrightarrow{q}_i^T \dot{\overrightarrow{r}}_D. \tag{3.65}$$

Using the identity $A_g^T q_i = \sigma_i w_i$ from Appendix A we have

$$\overrightarrow{\gamma}_l = \sum_{i=1}^{2m} (A_g^T \frac{\overrightarrow{q}_i}{\sigma_i}) \frac{1}{\sigma_i} (\overrightarrow{q}_i^T \dot{\overrightarrow{r}}_D) = \sum_{i=1}^{2m} A_g^T \frac{1}{\sigma_i^2} \overrightarrow{q}_i (\overrightarrow{q}_i^T \dot{\overrightarrow{r}}_D). \tag{3.66}$$

Using the identity

$$\frac{q_i}{\sigma_i^2} = (AA^T)^{-1} q_i \tag{3.67}$$

from Appendix A we have

$$\overrightarrow{\gamma}_l = \sum_{i=1}^{2m} A_g^T (A_g A_g^T)^{-1} \overrightarrow{q}_i (\overrightarrow{q}_i^T \dot{\overrightarrow{r}}_D) = A_g^T (A_g A_g^T)^{-1} \sum_{i=1}^{2m} \overrightarrow{q}_i (\overrightarrow{q}_i^T \dot{\overrightarrow{r}}_D). \tag{3.68}$$

Hence,

$$\overrightarrow{\gamma}_l = A_g^T (A_g A_g^T)^{-1} \dot{\overrightarrow{r}}_D. \tag{3.69}$$

■

Chapter 4

Path Planning

When conducting simulations it was found that if all particles were further away from each other they could be steered at much higher speeds. If in the course of a simulation, any two particles came close to each other, the control voltage rose sharply, and saturated the actuators. A rigorous mathematical explanation for this observation is provided in chapter 3. In order to efficiently transport particles, it is necessary that the particles do not come too close to each other during the entire steering process. Manually designing such paths is not feasible, especially when designing paths for three or more particles and hence there was a need to develop an automated method for path planning. This chapter deals with the objective of efficiently transporting particles between given initial and final positions. Section 4.1 outlines a method for rapidly generating high probability paths for efficiently steering particles. Section 4.2 presents a method for picking the best path using an algorithm called Dynamic Programming. Finally, section 4.3 presents simulation results.

4.1 Generating High Probability Paths

In order to ensure that particles stay atleast a pre-set distance apart during the steering process, it is necessary to impose certain restrictions on their movement.

Subsection 4.1.1 outlines these restrictions. Subsection 4.1.2 then introduces a notation for representing the paths and subsection 4.1.3 continues to present a method for rapidly obtaining high probability paths for a single particle. Lastly, subsection 4.1.4 extends the method to obtaining high probability paths for multiple particles.

4.1.1 Constraints on Particle Motion for Generating High Probability Paths

The following constraints imposed upon particle motion guarantee a minimum distance of $a/\sqrt{2}$ units between each pair of particles at all times.

- At time $t = 0$, each particle is at one of the vertices of the grid shown in Fig. 4.1.
- The motion of all particles is constrained to follow along the grid.
- At any given point of time, all particles move with the same speed.
- The particles can move with variable speed as they traverse along the grid segments.
- The particles do not collide.

This ensures that all particles leave and arrive at the grid vertices at the same time.

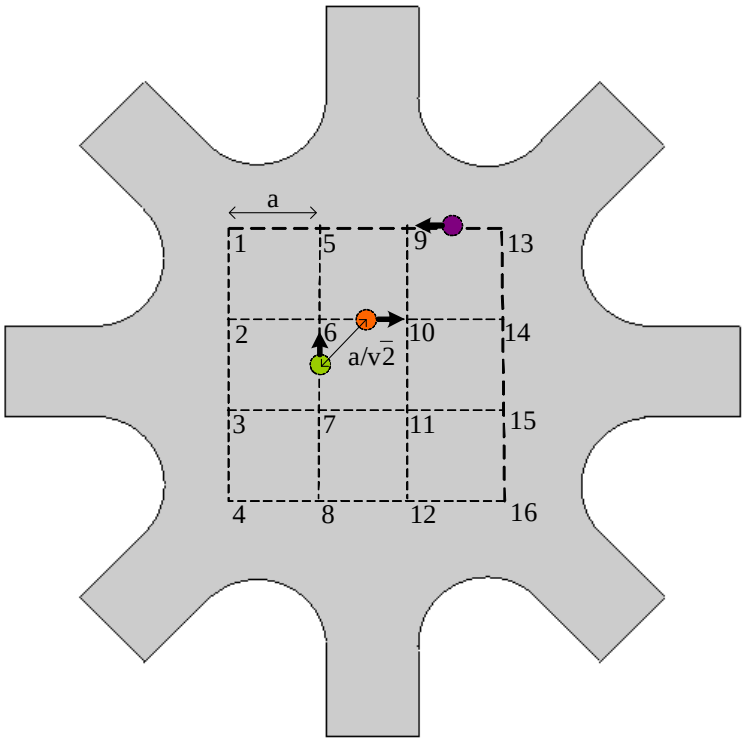

Figure 4.1: The numbers represent vertices of the grid. If at time $t = 0s$, each particle is at one of the vertices of the grid, and for all time $t > 0s$, the motion of the particles is constrained along the grid, all particles move with the same speed at any given time, and the particles are on trajectories such that they do not collide, then, the minimum distance between any two particles at all times is always greater than or equal to $a/\sqrt{2}$.

4.1.2 Notation for Representing Paths

Consider the path for a single particle traveling from vertex 2 to vertex 15 through vertices 6, 7 and 11. This path can be represented by a node diagram as shown in Fig. 4.2. Here each node represents a vertex through which the particle passes on its journey from the initial to the final vertex.

A multi-particle path is represented in a similar fashion as shown in Fig. 4.3.

4.1.3 Method for Rapidly Obtaining Paths for Single Particles

Let us say that we want to generate all possible paths for a single particle traveling from vertex 2 to vertex 15. To do this, first assign string variables r, l, u, d, s to denote right, left, up, down and stationary motions of the particle respectively. At a minimum, the particle must move three steps to the right and one step downward. Thus we associate a motion array shown in Fig. 4.4 with this path. We can see that all possible unique permutations of the elements of the motion array would give us all possible paths from vertex 2 to vertex 15 that involve moving three steps to the right and one step downward as shown in Fig. 4.4.

It should be noted, that it is possible to extend the degree of freedom of the path by adding equal and opposite moves or by adding an arbitrary number of stationary elements to the motion array. For example, adding an additional canceling up and down motion at arbitrary locations to the motion array will yield a new motion array and corresponding new set of paths. The additional degrees of freedom may be introduced based on the designer's judgement. This is especially

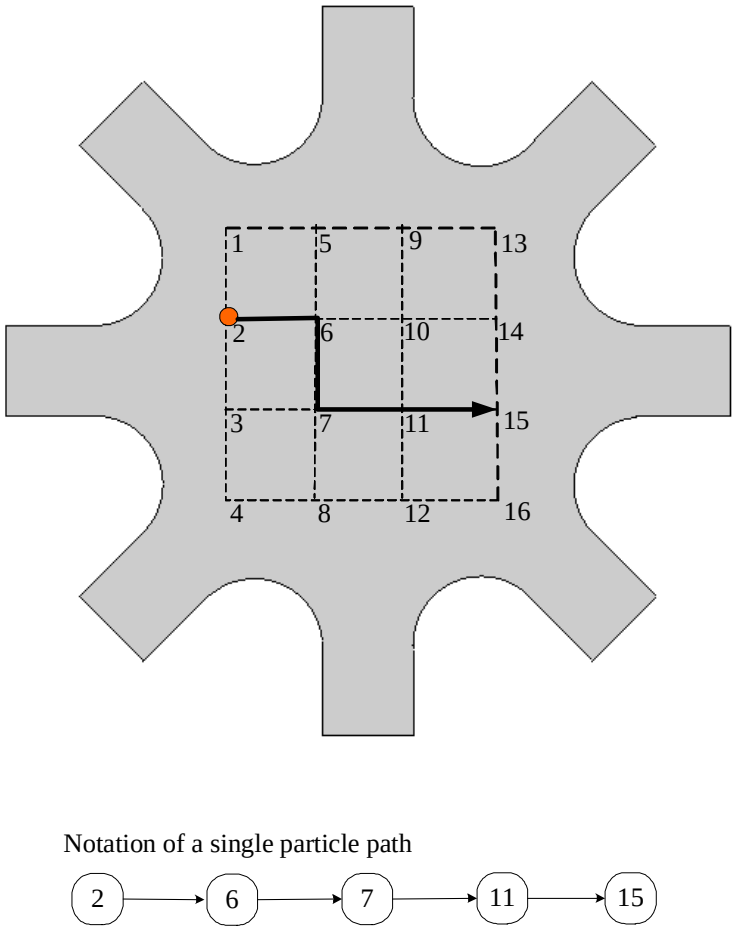

Figure 4.2: This figure gives the notation for representing the path of a single particle. As an example, the path of a particle as it moves from vertex 2 to vertex 15 passing through vertices 6, 7 and 11 en route is represented by the node diagram notation.

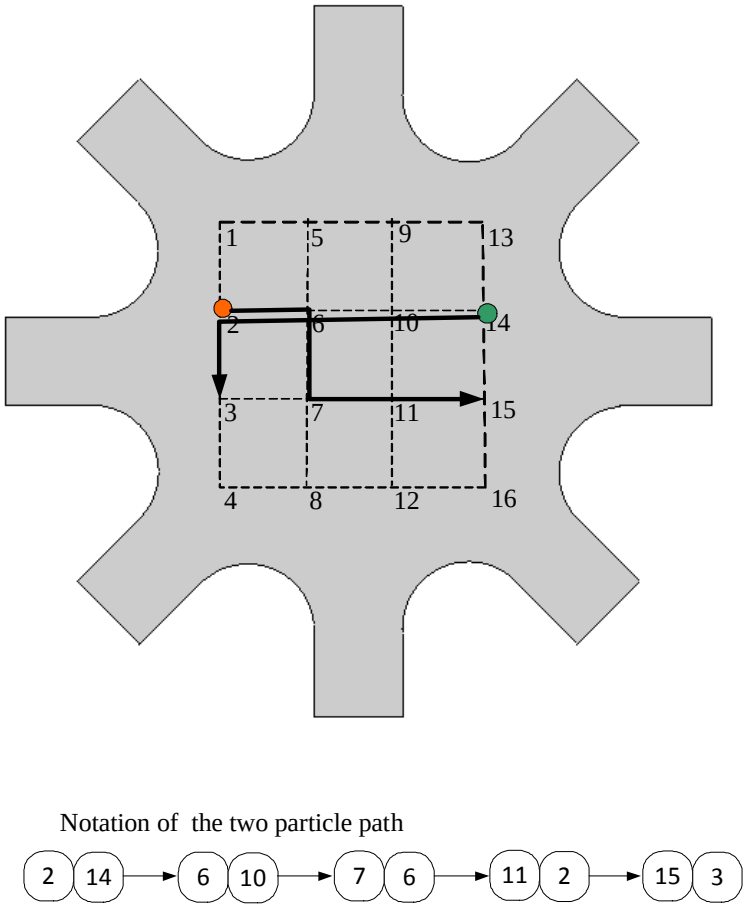

Figure 4.3: This figure gives the notation for representing the paths for multiple particles. As an example, the path of two particles is shown here. The first particle travels from vertex 2 to vertex 15, passing through vertices 6, 7 and 11. The second particle travels from vertex 14 to vertex 3, passing through vertices 10, 6 and 2. The path is represented by the node diagram notation.

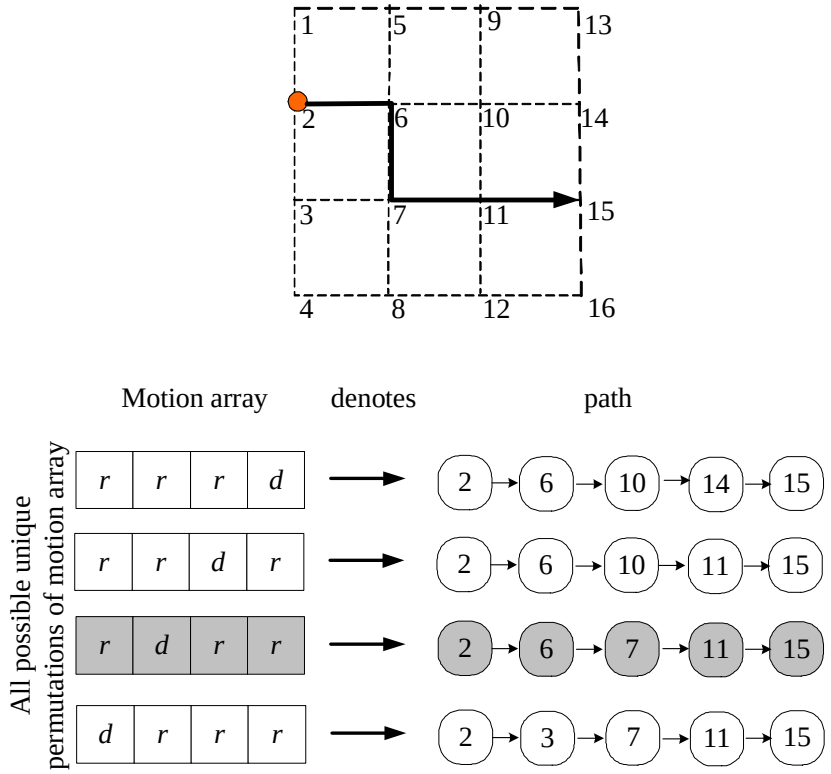

Figure 4.4: This figure illustrates a method for obtaining all possible paths for a single particle moving from vertex 2 to vertex 15. We assume that the particle is constrained to only move 3 steps to the right and one step down. All possible unique permutations of the motion array are shown on the left and the corresponding paths are shown on the right. The path of the particle shown on the grid is denoted by the third motion array that is shaded.

useful for extending a short motion array for a particular particle when the motion arrays of other particles are longer, or if the particle motion is congested and more freedom is required for the particles to reach a path with optimal separation.

4.1.4 Method for Rapidly Obtaining Paths for Multiple Particles

Let S_i denote the set of all possible paths for particle i. Then, $S_{all} = S_1 \times S_2 \times .. \times S_m$ represents the set of all possible path combinations that will take m particles from given initial to final positions. S_{all} also contains paths such that two or more particles collide during the steering process. We then have to cull a subset $S_{feasible} \subset S_{all}$ whose elements are all "possible" multi-particle paths that will take the particles from given initial to final positions. This process is best illustrated with an example.

Let us say for example that we wish to obtain all feasible paths that will take two particles from initial vertex positions 2 and 14 to their respective final vertex positions 15and 3 as shown in Fig 4.5.Let S_1 denote all possible paths from vertex 2 to vertex 15 for particle one. Let S_2 denote all possible paths from vertex 14 to vertex 3 for particle two. Following steps outlined in the earlier subsection (4.1.3) we can obtain the sets S_1 and S_2. Sets S_1 and S_2 are shown in Fig. 4.5 and set $S_{all} = S_1 \times S_2$ is shown in Fig. 4.6. However, not all paths of the set S_{all} are feasible. Paths where two particles collide or cross over need to be eliminated from the list. After eliminating such paths we are left with a set of feasible paths $S_{feasible}$ as shown in Fig. 4.7.

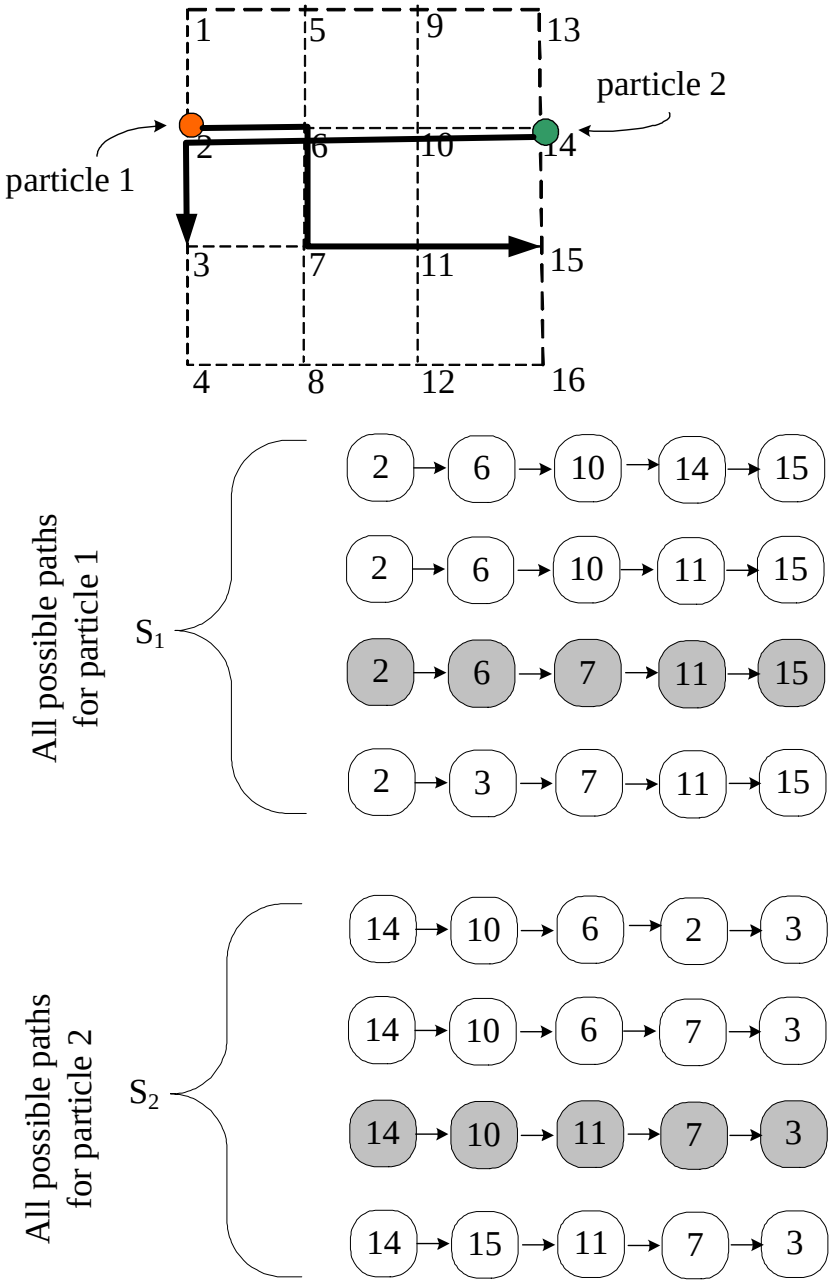

Figure 4.5: In this figure, S_1 denotes the set of all possible paths for particle 1 traveling from vertex 2 to vertex 15 and S_2 denotes the set of all possible paths for particle 2 traveling from vertex 14 to vertex 3. The path of each particle illustrated on the grid is shaded in the sets S_1 and S_2.

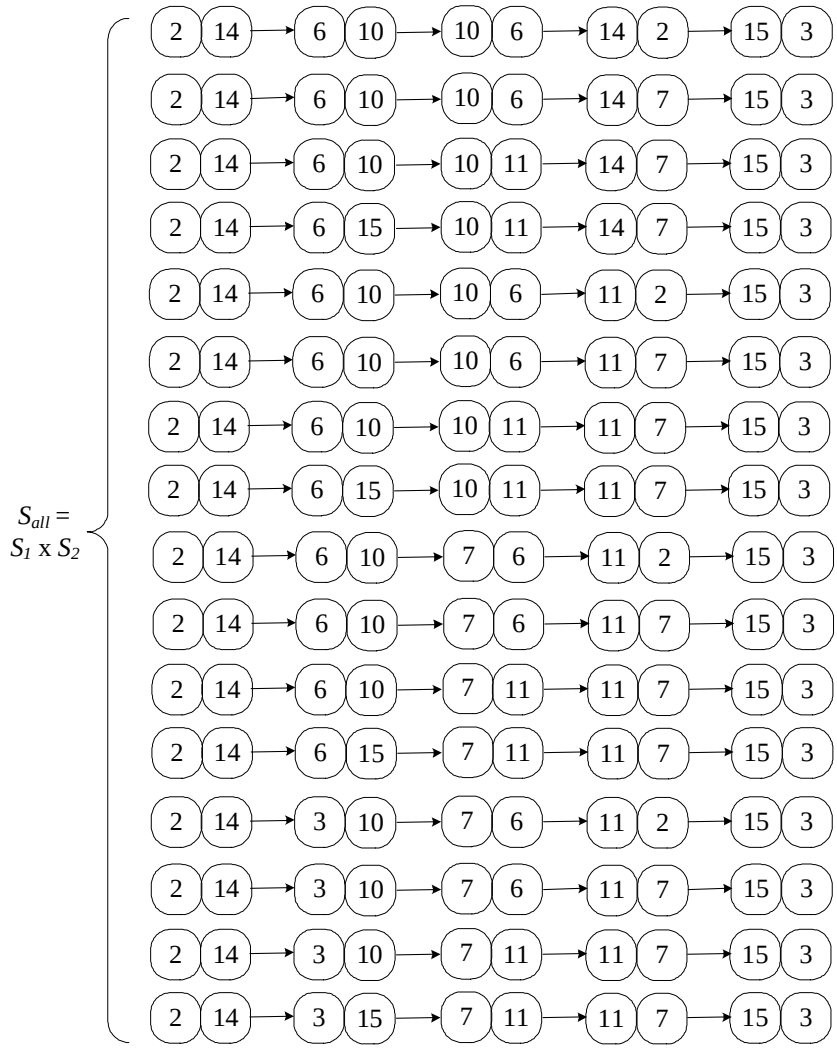

Figure 4.6: This figure denotes the set $S_{all} = S_1 \times S_2$ where S_1 is the set of all paths for particle 1 traveling from vertex 2 to vertex 15 and S_2 is the set of all paths for particle 2 traveling from vertex 14 to vertex 3.

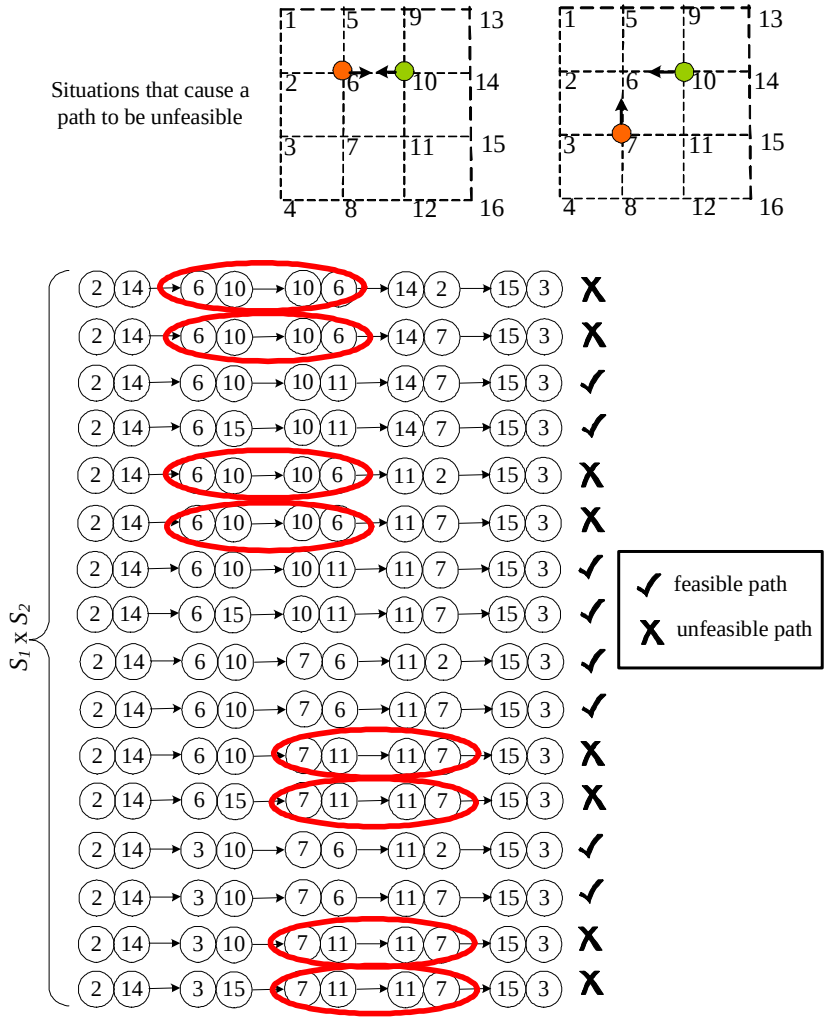

Figure 4.7: Not all paths of the set $S_1 \times S_2$ are feasible. Paths in which the two particles collide are unfeasible. Situations that cause the path to be unfeasible are shown at the top. Unfeasible paths in the set are marked by a cross, and the points on these paths where particle collision occurs are highlighted with a red ellipse. Feasible paths are marked with a check mark. The set of feasible paths forms the set $S_{feasible}$.

4.2 Picking the Most Efficient Path

In this section we shall present a method for picking the most efficient path out of the list of feasible paths obtained in the previous section. The most efficient path is defined as the one that transports particles between given initial and final positions in the shortest time. In subsection 4.2.1 we arrange the set of feasible paths in a network graph to enable the use of standard optimal path planning methods. Then in subsection 4.2.2 we assign a cost to each segment of the network graph to quantify the efficiency of each segment of the network. Finally, in subsection 4.2.3 we demonstrate the use of the Dynamic Programming algorithm to pick the most efficient path.

4.2.1 Representing High Probability Paths as a Network Graph

The set of feasible paths can be represented in a compact notation as shown in Fig. 4.8. This network diagram enables us to use a standard algorithm called Dynamic Programming to pick the most efficient path.

4.2.2 Computing the Cost for Each Path Segment

The next step in the process is to assign a cost to each segment of the network graph to quantify the efficiency of each path segment. We chose this cost to be the time needed to traverse the particular segment. As an example, let us compute the cost associated with the segment marked in Fig. 4.9.

Physically, it means that particle one moves from vertex 2 to vertex 6 and

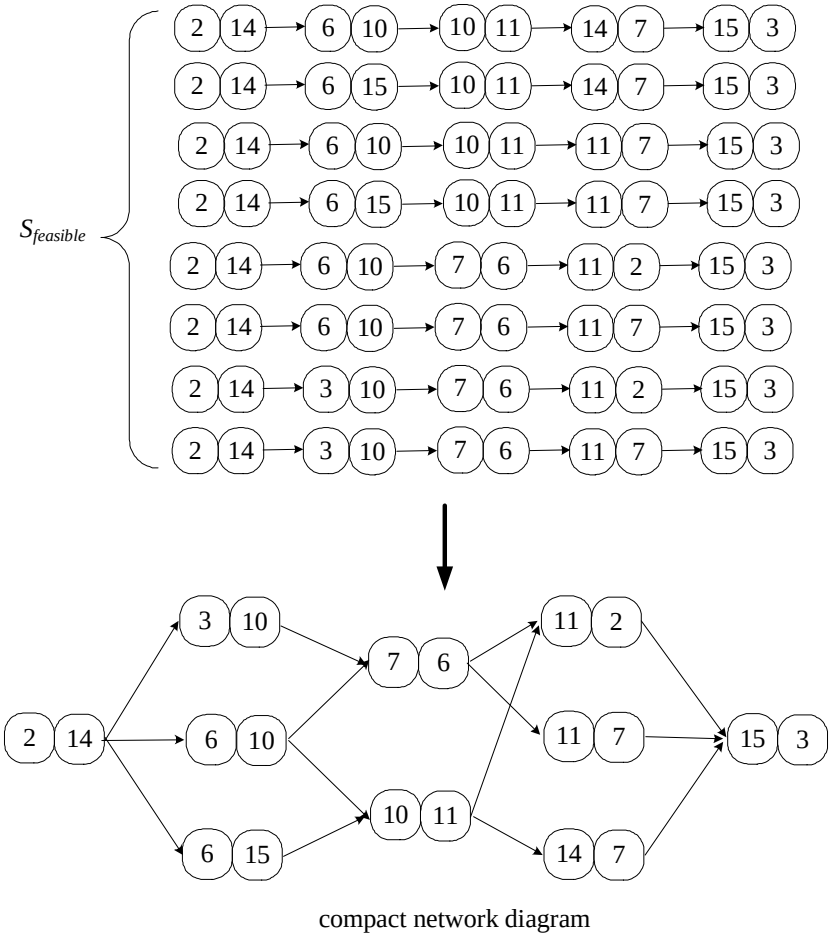

Figure 4.8: The set of feasible paths are arranged in a compact network diagram to enable the use of a standard algorithm called Dynamic Programming for picking the most efficient of these paths.

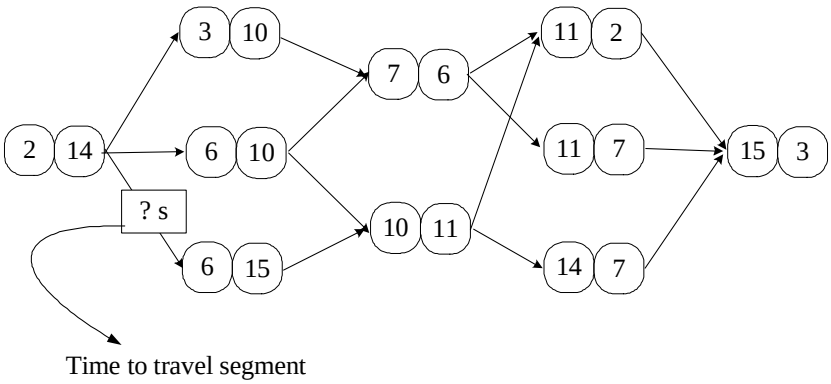

Figure 4.9: We assign a cost to each segment of the network graph. For the purpose of our problem, we have chosen this cost to be the minimum time required to travel the segment given the voltage constraint of $\pm 10V$ on each electrode. In this illustration the minimum time required for particle one and two to simultaneously travel from vertex 2 to vertex 6 and from vertex 14 to vertex 15, respectively, is assigned to the segment marked in the figure.

particle two moves from vertex 14 to vertex 15. The motion is restricted such that both particles move with the same speed at any given instant, though that speed may vary as they move along their paths. Given that the distance between two adjacent vertices is a, let ϱ be a parameter that linearly increases from 0 to a as particles move from the beginning of a segment to the end of of the segment. Let $S_p(\varrho) \geq 0$ denote the speed of the particle when at position $\vec{r}$ corresponding to parameter ϱ. The minimum time needed to travel the segment is given by

$$t_{\min} = \int_0^t dt = \int_0^a \frac{d\varrho}{S_{p_{\max}}(\varrho)}, \tag{4.1}$$

where $S_{p_{\max}}(\varrho)$ is the maximum speed at which the particles can be actuated, given the actuation limit of $\pm 10V$ on each electrode.

Now, let us compute $S_{p_{\max}}(\varrho)$. From the previous chapter we know that the voltage required to steer particles at position $\vec{r}$ with speed $S_p(\varrho)$ along direction vectors $\widehat{e}$ is given by

$$\vec{\gamma} = A^{\ddagger}(r) S_p(\varrho) \widehat{e}. \tag{4.2}$$

Taking the infinity-norm $\|\|_\infty$ on both sides we get

$$\|\vec{\gamma}\|_\infty = \left\|A^{\ddagger}(\vec{r}) S_p(\varrho) \widehat{e}\right\|_\infty = S_p(\varrho) \left\|A^{\ddagger}(\vec{r}) \widehat{e}\right\|_\infty, \tag{4.3}$$

as $S_p(\varrho) \geq 0$. $\|\vec{\gamma}\|_\infty$ represents the modulus of the largest element of $\vec{\gamma}$. The actuation limit of $\pm 10V$ for each electrode is mathematically expressed as $\|\gamma\|_{\infty\,\max} = 10$. Now we want to find the maximum speed $S_{p_{\max}}(\varrho)$ with which we can steer the particle at a given position. If $\|\vec{\gamma}\|_\infty < 10$ for a particular value of $S_p(\varrho)$ we can scale up both $S_p(\varrho)$ and γ up to the point where $\|\vec{\gamma}\|_\infty = 10$. At this point, $S_p(\varrho)$ becomes

$S_{p_{\max}}(\varrho)$. Similarly, if $\|\vec{\gamma}\|_\infty > 10$ for a particular value of $S_p(\varrho)$ we can scale up $S_p(\varrho)$ and correspondingly $\vec{\gamma}$ up to the point where $\|\vec{\gamma}\|_\infty = 10$. At this point $S_p(\varrho)$ becomes $S_{p_{\max}}(\varrho)$. Hence $S_p(\varrho) = S_{p_{\max}}(\varrho)$ when $\|\vec{\gamma}\|_\infty = 10$.

Plugging these values in equation (4.3) we have

$$10 = S_{p\,\max}(\varrho) \left\| A^{\ddagger}(\vec{r})\widehat{e} \right\|_\infty \tag{4.4}$$

or

$$S_{p\,\max}(\varrho) = \frac{10}{\|A^{\ddagger}(\vec{r})\widehat{e}\|_\infty} \tag{4.5}$$

Substituting (4.5) in equation (4.1) we determine that the cost associated (or the minimum time required to travel the segment in Fig. 4.9) is given by

$$t_{\min} = \int_0^t dt = \int_0^a \frac{d\varrho}{\frac{10}{\left\| A^{\ddagger}(\vec{r})\widehat{e} \right\|_\infty}}. \tag{4.6}$$

We calculate the cost for each segment in this way.

4.2.3 Using Dynamic Programming to Pick the Most Efficient Path

In our example, there are 20 possible routes from the initial to the final position. Our objective is to pick the most efficient path out of all these possible paths. One way to do this would be to calculate the travel time for each path and find the path that takes the minimum time to traverse. While this is feasible for simple cases, it rapidly becomes computationally expensive as the number of particles increases or as the number of steps in the path increases. To tackle this issue, an algorithm known as the Dynamic Programming [31] can be used. It helps pick

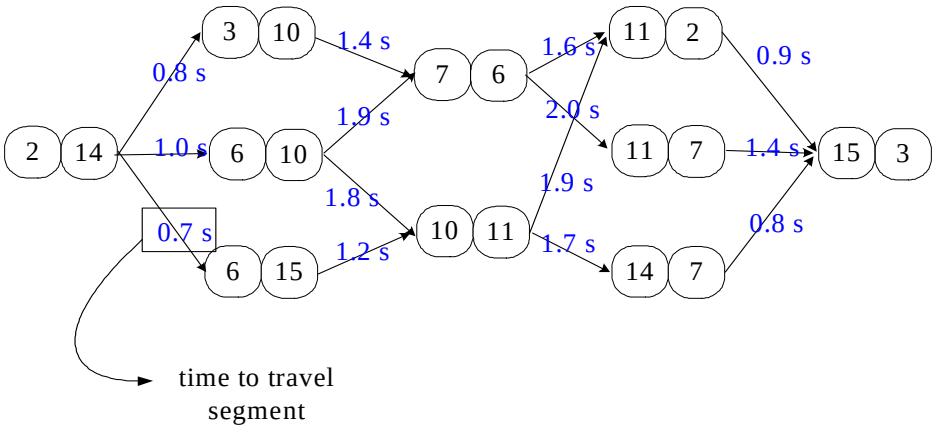

Figure 4.10: This figure shows the network diagram of all feasible paths for two particles traveling from initial vertices 2 and 14 to the final vertices 15 and 3. In addition, the cost associated with each segment (defined as the time to travel that particular segment) is also indicated.

the most efficient path with much less demanding computations. In this method, instead of starting from the initial node and attempting different routes to the final node, the algorithm works backward from the final node to find the fastest route as described below.

In order to effectively describe this algorithm, we split the procedure into 4 stages ($Stage$ 1, $Stage$ 2, $Stage$ 3, $Stage$ 4). In addition, each of the 20 paths are resolved into 5 steps ($Step$ 0, $Step$ 1, ..., $Step$ 4). This is illustrated in Fig. 4.11.

- In $Stage$ 1 of the algorithm, we consider the nodes in $Step$ 3 and find the most efficient route from each of these nodes to the final node. As an example, we find the most efficient path from node (11,2) to the final node (15,3). Since, in this case, there is only one choice it is the fastest route. We then record this

as the least time needed to go from node (11,2) to the final node (15,3) in the lower right corner of node (11,2), in bold red print. We repeat the procedure for the remaining nodes (11,7) and (14,7) in *Step* 3 as illustrated in *Stage* 1 of Fig. 4.11.

- In *Stage* 2 of the algorithm, we move one step back to the nodes in *Step* 2 and find the most efficient route from each of these nodes to the final node. As an example, we consider node (7,6) which is highlighted in blue in Fig. 4.11. Note that, in this case, we have two possible options. *Route* 1, which connects node (7,6) to node (11,2) to node (15,3), and *Route* 2 which connects (7,6) to node (11,7) to node (15,3). For *Route* 1, the total travel time is 1.6s+0.9s = 2.5s. For *Route* 2, the total travel time is 2.0s + 1.4s = 3.4s. We see that *Route* 1 is the fastest path. Hence we retain *Route* 1 and eliminate *Route* 2 (i.e. we erase the arrow from (7,6) to (11,7) corresponding to *Route* 2) and record the minimum travel time for node (7,6) in the lower right corner of the node in bold red print, as illustrated in *Stage* 2b of Fig. 4.11. We repeat this process for other nodes in *Step* 2.

- We continue this process, moving back one step at a time and for each node in the *Step*, retaining only the fastest path to the final node.

- At the end of this procedure, for every node in the network diagram, we obtain the minimum travel time to the final node and the optimal direction to follow in leaving the node. The fastest or the most efficient path can be traced from the initial node to the final node as shown in *Stage* 4 of Fig. 4.11.

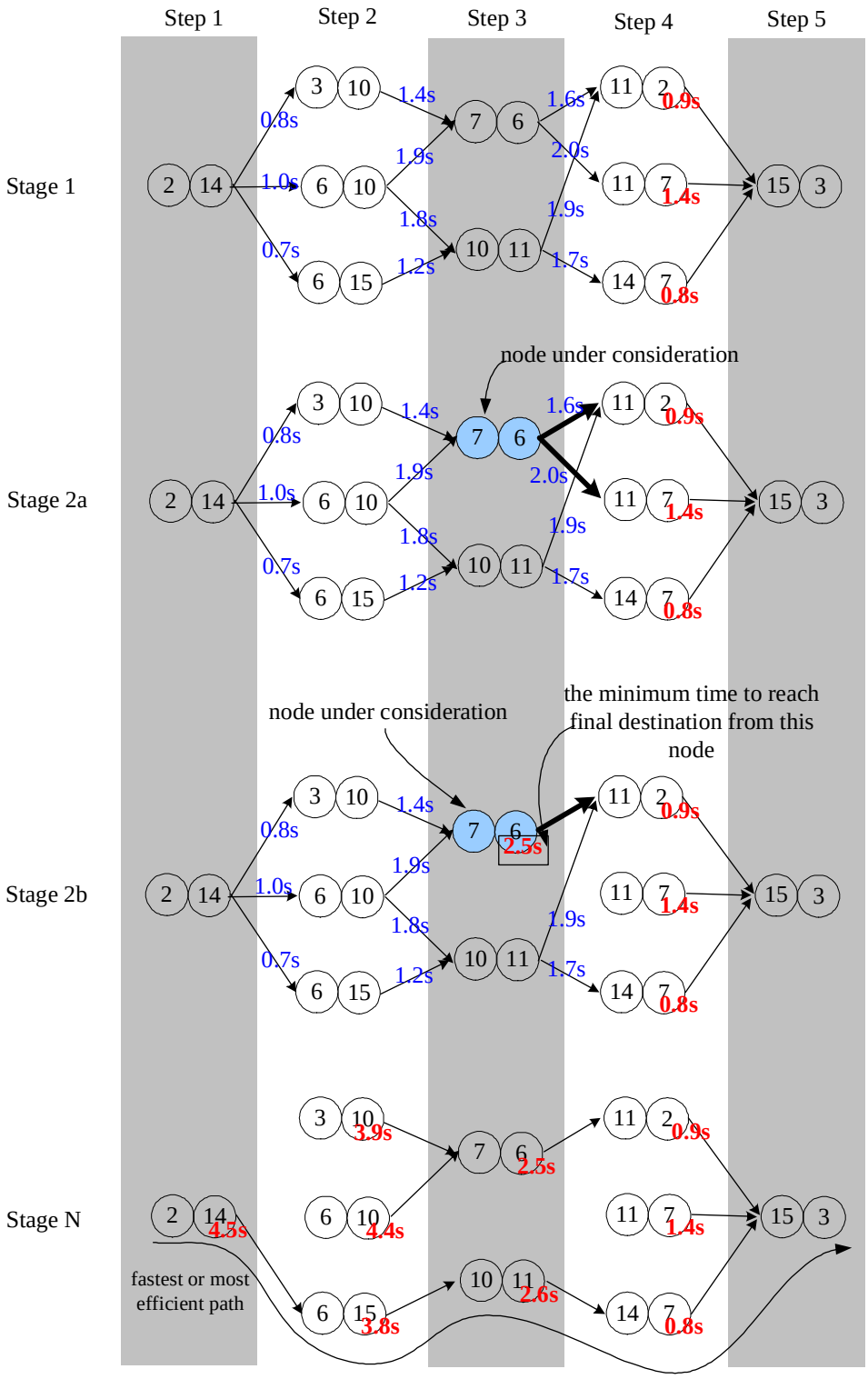

Figure 4.11: This figure illustrates the Dynamic Programming algorithm for finding the optimal path for a specific two particle case. A detailed description of this algorithm is provided in subsection 4.2.373

4.3 Simulation Results

In this section we present some simulation results. For the two particle example used for illustration, it was possible to compute the optimal path by hand, but as the number of particles and the length of the path increases, the number of feasible paths also increases rapidly, necessitating computer assistance. The table shows the number of feasible paths for two, three, four, and five particles respectively for a six step path.

Number of particles	Number of feasible paths (6 step path)
2	66
3	306
4	3886
5	11780

The number of feasible paths change with the specific case being considered, nonetheless it serves to make the point that the number of feasible paths rapidly increases with an increase in number of particles. A MATLAB program was written to automate steps outlined in section (4.1) and (4.2). Fig. 4.12, Fig. 4.13, Fig. 4.14 , and Fig. 4.15 show optimal paths for two, three, four, and five particles respectively.

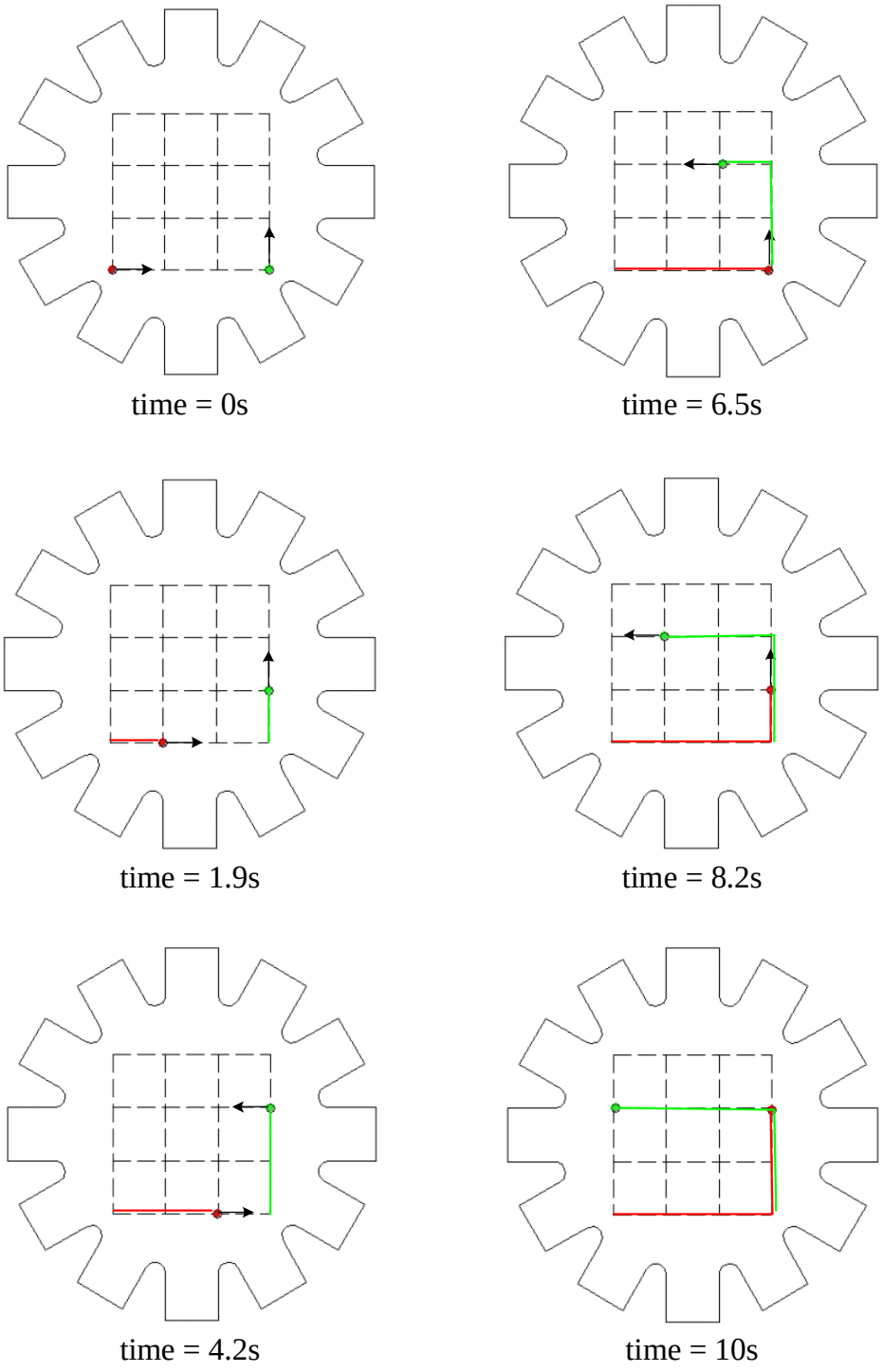

Figure 4.12: This figure shows the optimal path for two particles computed using the Dynamic Programming algorithm described in the earlier section. The initial and final positions of the particles are shown in the top left sub-figure and the bottom right sub-figure, respectively.

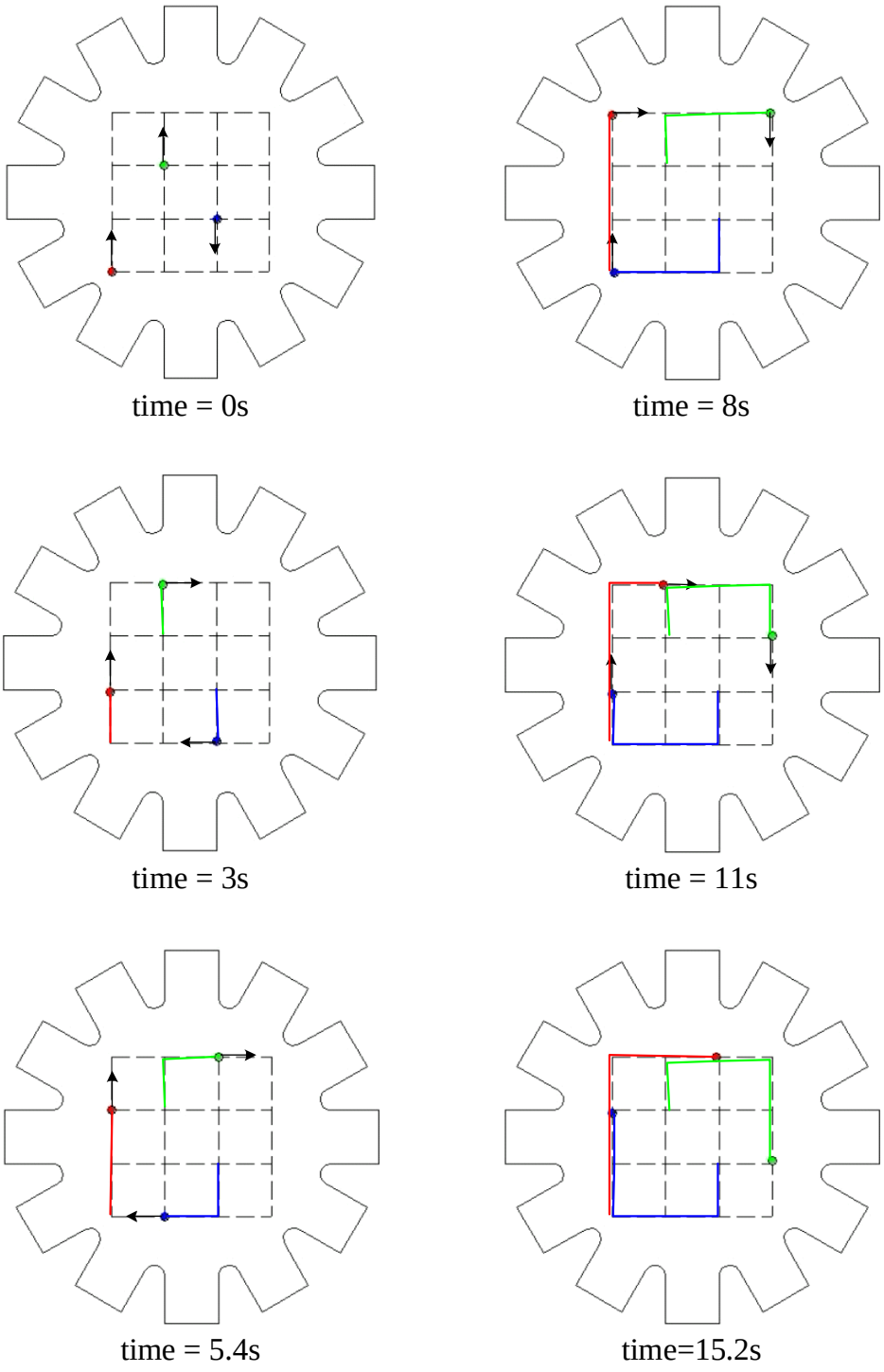

Figure 4.13: This figure shows the optimal path for three particles computed using the Dynamic Programming algorithm described in the earlier section. The initial and final positions of the particles are shown in the top left sub-figure and the bottom right sub-figure, respectively.

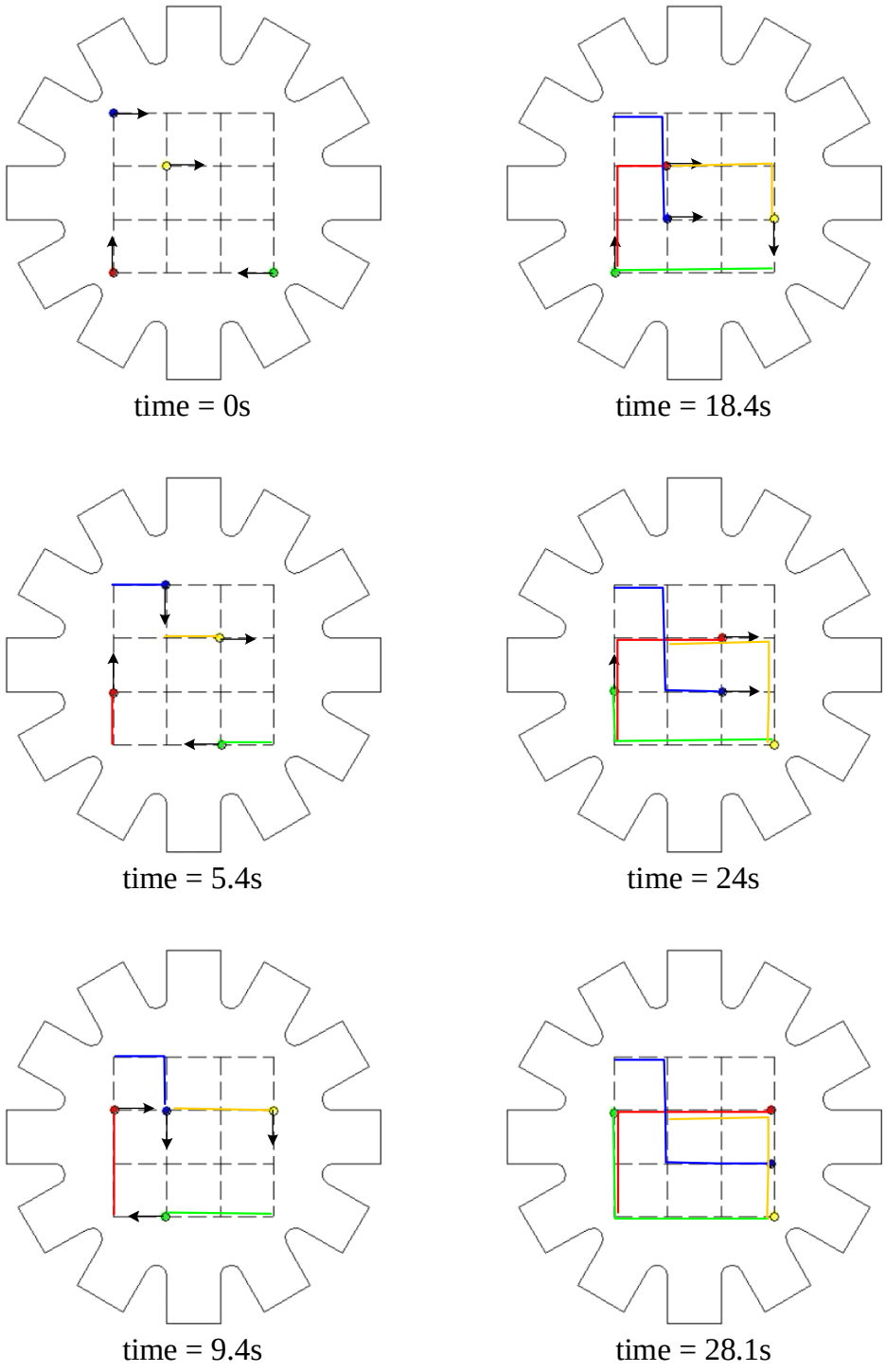

Figure 4.14: This figure shows the optimal path for four particles computed using the Dynamic Programming algorithm described in the earlier section. The initial and final positions of the particles are shown in the top left sub-figure and the bottom right sub-figure, respectively.

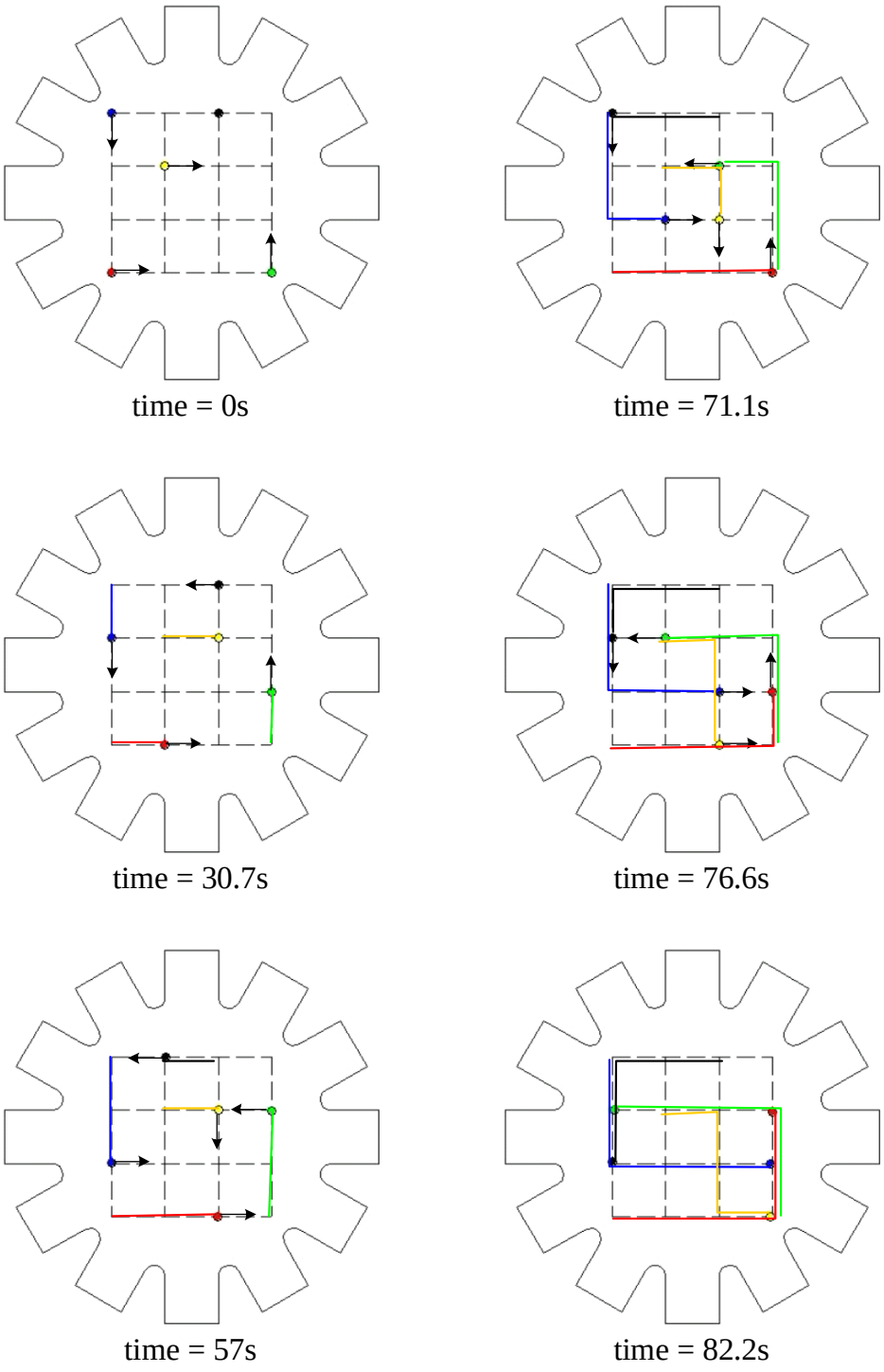

Figure 4.15: This figure shows the optimal path for five particles computed using the Dynamic Programming algorithm described in the earlier section. The initial and final positions of the particles are shown in the top left sub-figure and the bottom right sub-figure, respectively.

Chapter 5

Experiments

Armani and Probst were the first to demonstrate electroosmotic particle steering in experiments in 2003 [1]. They used a cross channel device design and a simple control algorithm that created a flow to the North if the particle was to the South of its desired position (or West if it was East of its desired position, etc). With this simple control algorithm it was not possible to steer more than one particle. Around that time, the author developed multi-particle control algorithms, that he analyzed, and validated through simulations. These algorithms were then adapted to the experiments by Probst, who subsequently demonstrated three particle steering in experiments in 2005. At this stage, Cummins became involved in the project and during his overlap with the author, Cummins improved the vision system and created an improved Matlab graphical user interface. At the end of 2005, through the control theory development efforts of the author and Probst's contributions, we were able to control 3 particles but not more. Both the author and Probst led a thorough investigation into the factors that prevented demonstration of steering more than three particles in experiments. In this vein, the author proved that the maximum particle actuation speed dropped rapidly with increase in the number of particles, and for more than three particles, the actuation was no longer sufficient to overcome the parasitic pressure flow. To address this issue, the author redesigned

the devices to enhance particle actuation by a factor of more than 5. The author, Cummins, and Probst then used these high performance devices to demonstrate steering of five particles in experiments(2008). This chapter focuses on the author's contribution to those experiments.

In section 5.1 we present one and three particle steering results through the efforts of Probst and Armani. In section 5.2 we identify the main roadblock to demonstrating steering of more than three particles in experiment - namely, a lack of sufficient actuation. In section 5.3 we identify the most feasible method for enhancing actuation - redesigning the shape of the device. In section 5.4 we present details about designing and fabricating molds for the high-actuation devices. In section 5.5 we outline the procedure used to condutct experiments. In section 5.6 we provide experimental results for steering of four and five particles. In section **??** we introduce a list of critical issues relating to the experimental method and apparatus that had to be sorted out to demonstrate five particle steering in a reproducible fashion. Finally, in section 5.8 the author's specific contributions to demonstrating steering of four and five particle experiments are listed.

5.1 Overview of One and Three Particle Steering Results

Fig. 5.1 shows the steering of a polystyrene microbead along a figure 8 in the four-electrode device through the efforts of Armani and Probst. Fig. 5.2 shows the work of Probst, in which two yeast cells are guided along circular paths while a third yeast cell is steered along a "UMD" path. Details about experimental setup and

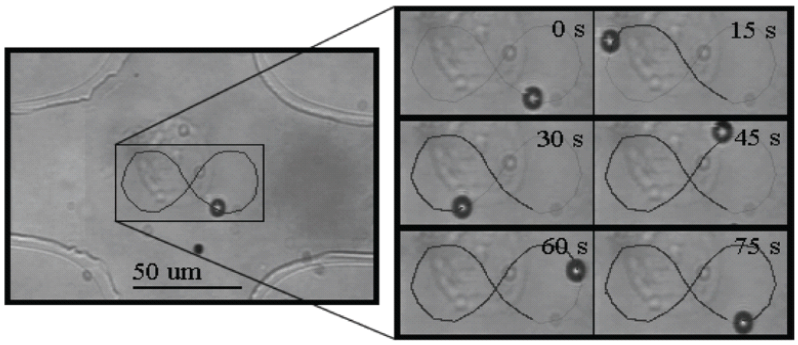

Figure 5.1: Control of a polystyrene bead along a figure 8 through the efforts of Mike Armani and Roland Probst. Left: photograph of a four channel microfluidic device with a figure "8" path superimposed on the image. Right: the actual path of the 5 micrometer polystyrene bead (Polysciences Inc., black circle) in the feedback control experiment.Snapshots are shown at six equally-spaced times. The bead follows the required trajectory to within a tolerance of 3 micrometers.

procedure are provided in [1].

5.2 Identifying Roadblocks to Demonstrating Five Particle Steering in Experiment - Insufficient Actuation

As mentioned earlier in chapters 3 and 4, we found that the maximum speed to which the particles could be actuated dropped drastically as particles came close to one another or as the number of particles increased. As a first line of precaution, we ensured that at least a distance of $a/\sqrt{2}$ units is maintained between each pair of particles at all times, using the method outlined in chapter 4. Still the drop in maximum particle speed with an increase in the number of particles was very rapid

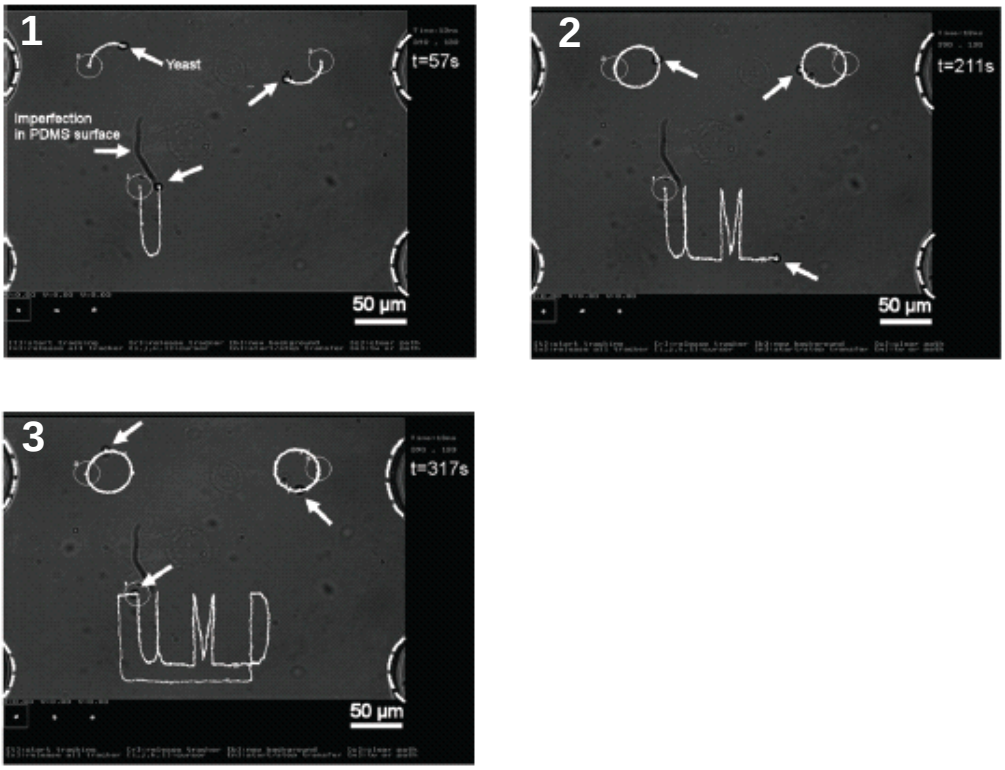

Figure 5.2: Steering of three yeast cells (5 micrometer diameter) around two circles and a "UMD" path through the efforts of Probst. The yeast cells are visible as black dots with a white center (marked with a white arrow in each image). The white curves are the trajectories that the target cells have traced out. The three yeast cells are being steered within an accuracy of one pixel (corresponding to less than 1 micrometer).

and for more than three particles, the electroosmotic actuation was not sufficient to overcome the parasitic pressure driven flows that existed in the device at all times. Fig. 5.3 gives the maximum particle steering speeds for one to five particles, while ensuring a minimum distance between any pair of particles. Based on the numbers shown in this figure it was clear that in order to demonstrate steering of five particles, the electroosmotic actuation had to be increased by at least a factor of five.

5.3 Evaluating Ways of Increasing Actuation

In order to enhance electroosmotic actuation, it is essential to first identify its drivers. The electroosmotic velocity at the tip of the microfluidic channel is given by

$$V_{EO_{tip}} = \frac{\epsilon\zeta}{\eta}\overrightarrow{E}_{tip}. \tag{5.1}$$

Therefore, there are four drivers of electroosmotic actuation - the permittivity of the fluid ϵ, fluid viscosity η, zeta potential ζ, and the electric field $\overrightarrow{E}_{tip}$. If we are to increase the electroosmotic fluid velocity at the microchannel inlet we have the following four options:

1. Increase the permittivity of the fluid ϵ
2. Increase the zeta potential ζ at the surface of the microchannels
3. Reduce the fluid viscosity η
4. Increase the electric field $\overrightarrow{E}_{tip}$

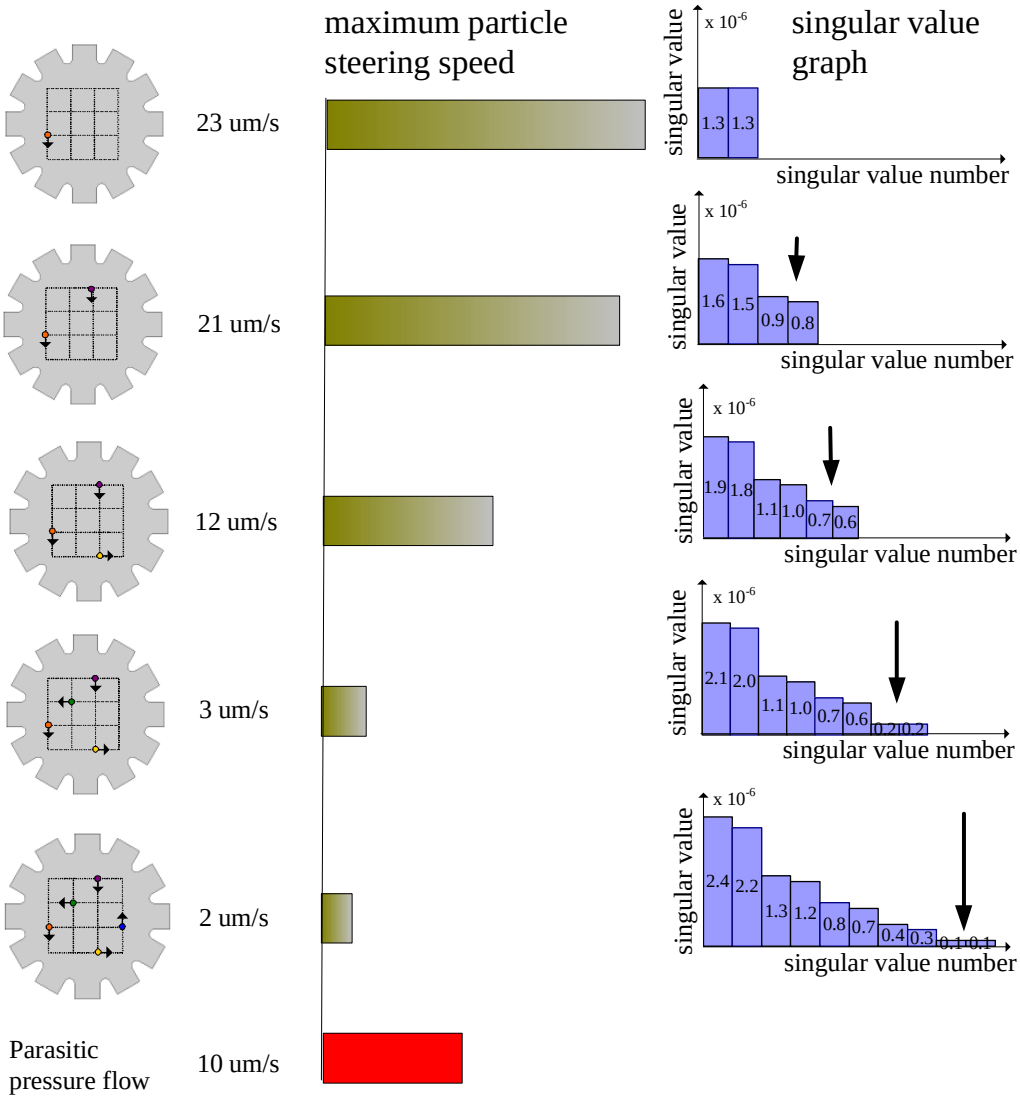

Figure 5.3: This figure shows, for a typical case, the maximum particle steering speed and singular values of the A matrix as the number of particles increase. For greater than three particles, the maximum particle steering speed is much lower than the mild parasitic pressure flow that always exists in the device, hence the inability to steer more than three particles with the previous setup.

The permittivity of water ϵ and its viscosity η are practically constant at normal operating conditions and were therefore ruled out. The zeta potential ζ is a measure of the surface charge density on the walls of the microfluidic channels. The higher the surface charge density, the higher the magnitude of ζ. To increase the charge density we could look at either modifying the surface chemistry of the microfluidic channels or build microfluidic channels with materials that have higher zeta potential. For all experiments up to the steering of three particles, we had used microchannels that were etched in PDMS and were covered with a Pyrex glass slide. This is one of the most common and mature technologies for building electroosmotically actuated microfluidic systems. Since we lacked the expertise in the area of surface modification, and it appeared to be a very resource-intensive path to pursue, we chose to look into enhancing electroosmotic flow by enhancing the electric field.

The electric field at the tip of the microfluidic channel is a function of the shape of the channels. The strength of the electric field $\overrightarrow{E}_{tip}$ can be enhanced by several times by appropriately designing the channel shape. We chose to express the shape of the channel (and therefore the electric field at the channel inlet) in terms of 7 parameters $h_1, h_2, t_1, t_2, t_3, l_1$ and l_2 as shown in Fig. (5.4).

Of these, we chose h_1, t_1, t_2, l_1, and l_2 to have specific values for the reasons outlined below. The parameters h_2 and t_3 were chosen such that the strength of the electric field $\overrightarrow{E}_{tip}$ was enhanced by a factor greater than 5 as compared to a straight channel.

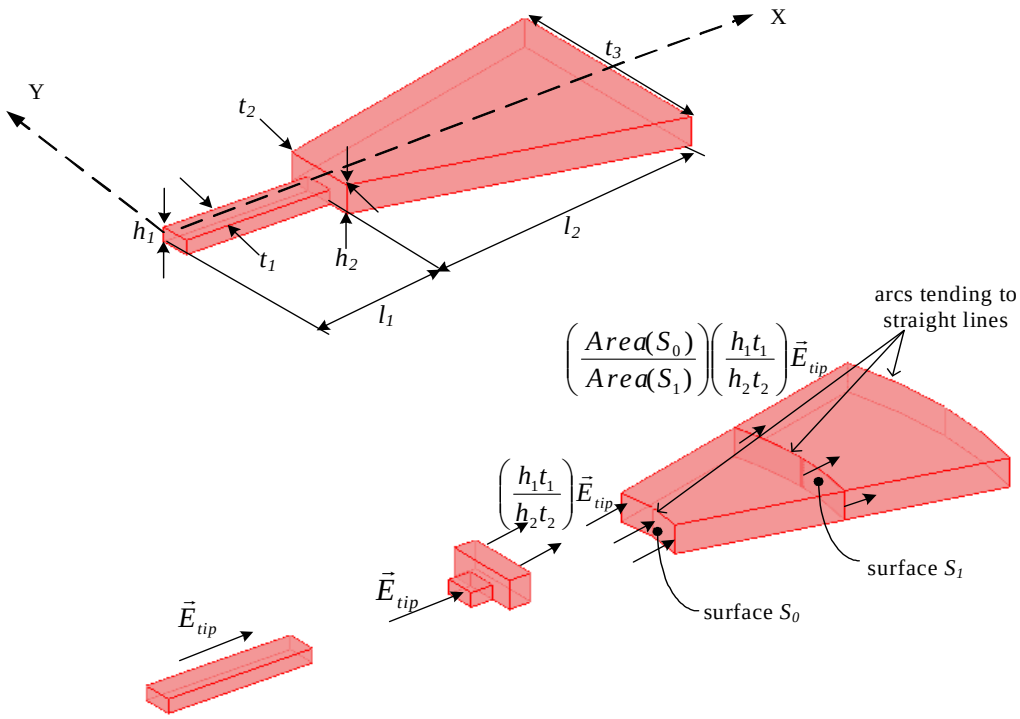

Figure 5.4: The microchannel shape was expressed in terms of seven parameters $h_1, h_2, t_1, t_2, t_3, l_1$, and l_2 as shown in this figure. The electric field strength at various points in the device is also indicated.

- We chose h_1 to be 5 μm. The rationale behind this choice was the following. We used polystyrene beads of size 1.2 μm and 2.2 μm for conducting experiments. Having $h_1 = 5$ μm ensured that the particle motion was constrained in the z direction. Without such constraints, the particles would move in and out of the camera focus during experiments. In addition, having $h_1 = 5$ μm ensured that there was sufficient space between the particles and channel ceilings and we found that it helped avoid the issues of clogged channels.

- We chose t_1 to be 25 μm. This ensured that the central chamber was entirely visible in the microscope field of view when using a 20$\times$ lens.

- We chose t_2 to be 85 μm. This choice was primarily driven by the fabrication tolerance limitations imposed by the mold creation technology as outlined in section 5.4. The trapezoidal structure (with sides t_2, t_3 and height l_1) would have to be fabricated as a second layer when making the mold. The fabrication technology demanded that devices be designed such that they will work despite a 30 micrometer error in the alignment between layers in all directions. So we chose t_2 to be 25 μm $+2 \times 30$ μm $= 85$ μm.

- We chose l_1 to be 150 μm based on the fact that 12 structures of size t_2 would have to be accommodated in a radial configuration.

- We chose l_2 to be 1800 μm because we found that $l_1 + l_2 \approx 2$ mm to be the length that allowed reliable manual cutting out of reservoirs in the device.

- The parameter h_2 was completely free and t_3 was subject to the upper con-

straint that 12 structures of size t_3 would have to be accommodated in a radial fashion.

In order to identify the right values for parameters h_2 and t_3 that would enhance $\overrightarrow{E}_{tip}$ by a factor greater than 5, we first express

$$\frac{\left\|\overrightarrow{E}_{tip}\right\|_2}{\left\|\overrightarrow{E}_{tip\_st}\right\|_2} \tag{5.2}$$

where $\overrightarrow{E}_{tip\_st}$ is the electric field at for the straight channel in terms of the parameters h_2 and t_3. To simplify our analysis we first made the following assumptions and approximations:

- We assumed a uniform electric field $\overrightarrow{E}_{tip}$ inside the straight channel.
- We ignored the edge effects at the intersection and assumed that as the electric flux lines relax from a cross section area of $h_1 t_1$ square units to $h_2 t_2$ square units the electric field drops by a factor equal to the ratio of the areas. So the electric field at the beginning of the tapering region would be $\overrightarrow{E}_{tip}(h_1 t_1 / h_2 t_2)$.
- For the tapering region we assumed a planar radial electric field, as would be the case for the electric field in a sector between two concentric cylindrical surfaces. The electric field in such a case is perpendicular to the concentric arcs as shown in Fig. 5.4. As the electric field flux lines diverge, the electric field strength drops by a factor that is equal to the ratio of area of the concentric surface to the area of the surface S_0 as indicated in Fig. 5.4.
- As the radii of the concentric surfaces are large and the conical angle is small (around 15° or 0.26 radians) we assumed that the arcs tend to straight lines.

- The graph of the strength of the electric field along the x axis is as shown in Fig. 5.5.

- The direction of the electric field is assumed to be parallel to the x axis.

By the definition of the potential difference we have that

$$\gamma_{AB} = \int_B^A \overrightarrow{E} \cdot d\overrightarrow{x} = \int_B^A \left\| \overrightarrow{E} \right\|_2 dx = Area\ under\ the\ curve\ as\ in\ Fig.5.5 \quad (5.3)$$

$$\Longrightarrow \gamma_{AB} \approx \left\| \overrightarrow{E}_{tip} \right\|_2 l_1 + \frac{1}{2} \left(\frac{h_1 t_1}{h_2 t_2} + \frac{h_1 t_1}{h_2 t_3} \right) \left\| \overrightarrow{E}_{tip} \right\|_2 l_2 \quad (5.4)$$

$$\Longrightarrow \left\| \overrightarrow{E}_{tip} \right\|_2 \approx \frac{\gamma_{AB}}{\left[l_1 + \frac{1}{2} \left(\frac{h_1 t_1}{h_2 t_2} + \frac{h_1 t_1}{h_2 t_3} \right) l_2 \right]} \quad (5.5)$$

For a straight channel the strength of the electric field $\left\| \overrightarrow{E}_{tip\_st} \right\|_2$ is obtained by setting $h_1 = h_2$ and $t_1 = t_2 = t_3$ in equation (5.5), hence we have

$$\left\| \overrightarrow{E}_{tip\_st} \right\|_2 \approx \frac{\gamma_{AB}}{[l_1 + l_2]}. \quad (5.6)$$

Dividing equation (5.5) by equation (5.6) we have

$$\frac{\left\| \overrightarrow{E}_{tip} \right\|_2}{\left\| \overrightarrow{E}_{tip\_st} \right\|_2} \approx \frac{[l_1 + l_2]}{\left[l_1 + \frac{1}{2} \left(\frac{h_1 t_1}{h_2 t_2} + \frac{h_1 t_1}{h_2 t_3} \right) l_2 \right]}. \quad (5.7)$$

We had fixed the values for paramters h_1, t_1, t_2, l_1, and l_2 as mentioned earlier. We have the freedom to choose any set of values for h_2 and t_3 (subject to constraints menteiond above) to meet our design objective of having

$$\frac{\left\| \overrightarrow{E}_{tip} \right\|_2}{\left\| \overrightarrow{E}_{tip\_st} \right\|_2} > 5. \quad (5.8)$$

We chose h_2 to be 10 μm, t_3 to be 500 μm.These values enhanced electroosmotic actuation by a factor of around 7.5 over that of a straight channel.

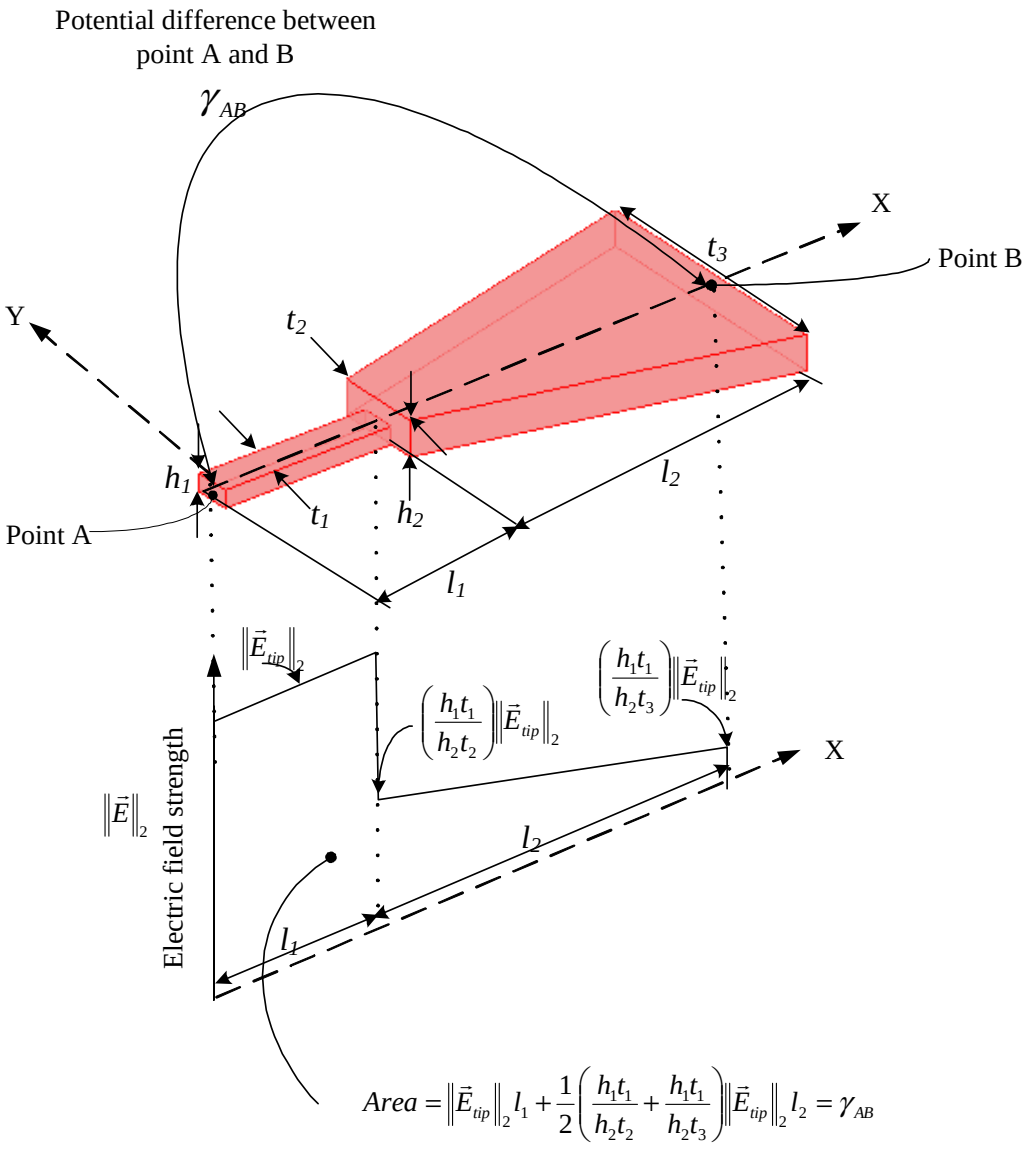

Figure 5.5: Graph of the electric field strength in the device as a function of the distance from the tip. The total area under the electric field strength curve equals the potential difference between the two ends of the channel.

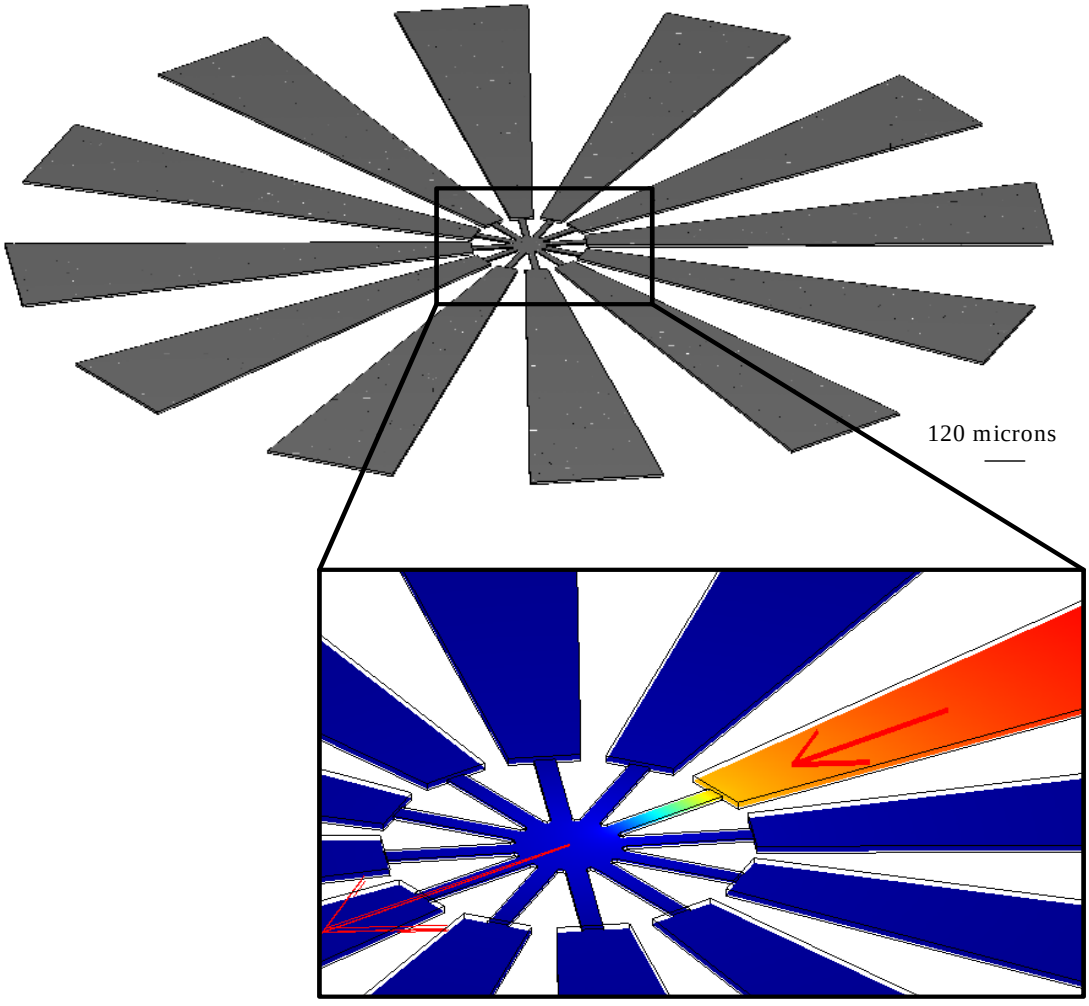

Figure 5.6: 3D rendering of the high-actuation microfluidic device. The electroosmotic actuation in this device is 7.5 times the actuation achieved in the device with straight channels.

5.4 Designing and Fabricating Molds for High-Actuation Devices

The Stanford microfluidics foundry (http://thebigone.stanford.edu/foundry/) provides an excellent service wherein a researcher can submit Autocad files of a 3D device design and, for a fee of $150, an SU8 mold is created, with a turn around time of 2 weeks. We utilized these services to fabricate the SU8 mold.

The 3D molds are created using a multilayer soft lithography process. In other words, the 3D structure is constructed by successively spin coating a layer of SU8, UV curing only desired portions of the layer and chemically etching away the uncured portion. The foundry does not reveal the exact process specifications but the general principle of soft lithography is common knowledge in microfluidic fabrication labs [32].

The structure for the high actuation device shown in Fig. 5.6 can be decomposed into three layers. The shapes of the first, second, and third layers are shown in Fig. 5.7, Fig. 5.8, and Fig. 5.9 respectively. The justifications for the various feature sizes are given in section 5.3.

In layer 2 (Fig. 5.8), the circles represent support posts. The support post diameter was chosen as 30 microns as it was the smallest feature size for free standing structures that our supplier could reliably fabricate. The spacing between the posts was chosen as 150 microns because structures with any lower aspect ratio were prone to collapse.

In layer 3 (Fig. 5.9), the reservoir placeholders were designed as annular structures because structures with large surface areas are prone to peeling due to

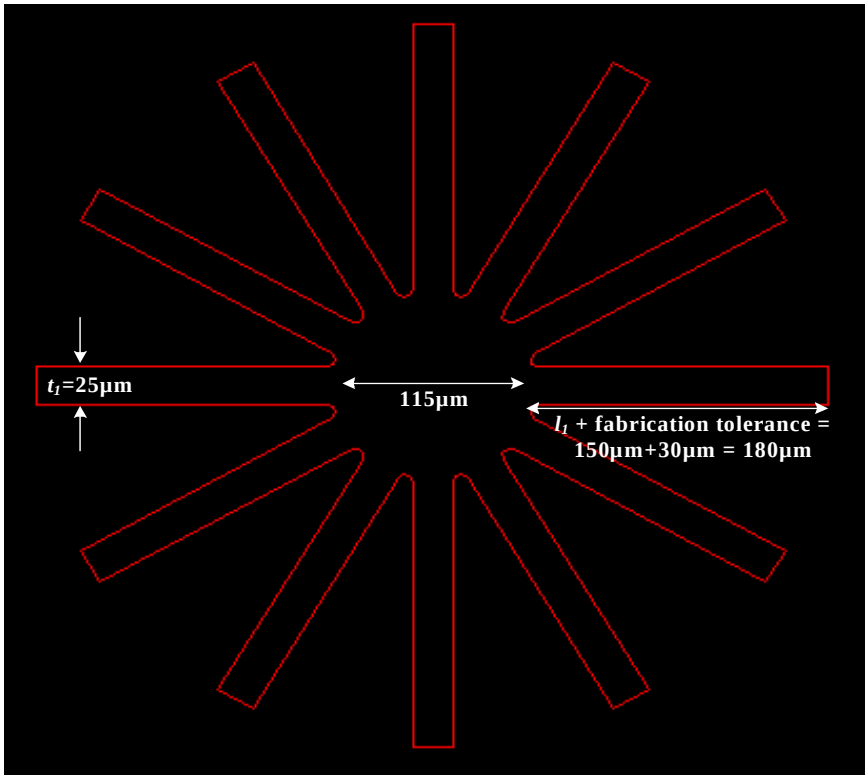

Figure 5.7: Autocad drawing of layer 1 of the high-actuation microfluidic device.

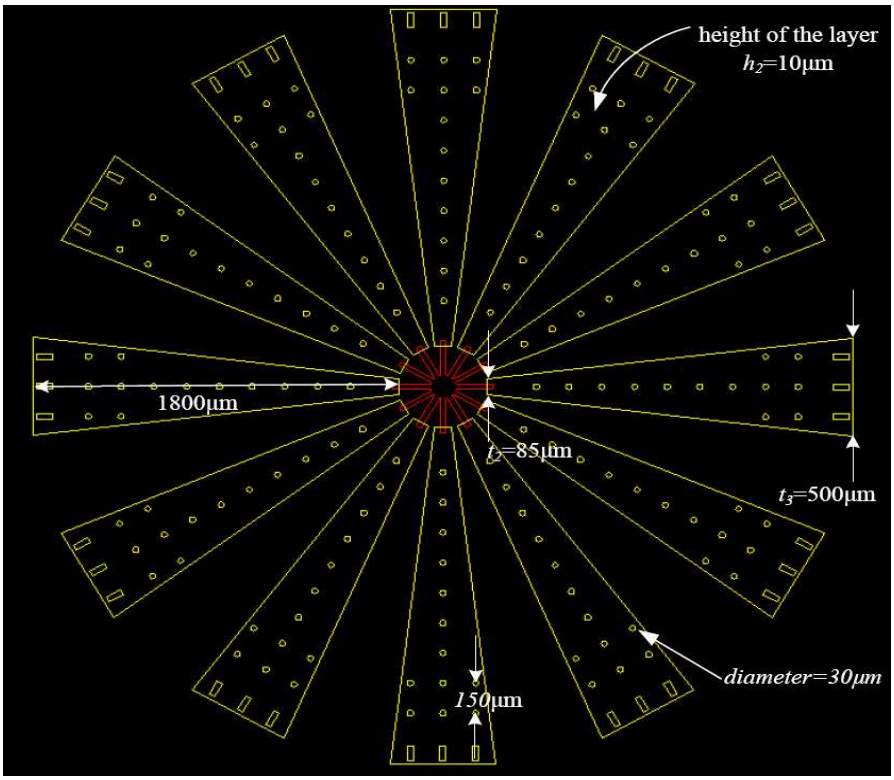

Figure 5.8: The yellow colored portion of the Autocad drawing represents layer 2 of the high-actuation microfluidic device. The 30 micron diameter circles are support posts. Their purpose is to prevent the channel ceiling from collapsing.

differential thermal stresses developed in the SU8 and silicon wafer substrate during fabrication. Alignment marks for all the three layers, which are essential to ensure alignment between the different layers during the fabrication process are also shown.

5.5 Experimental Methods

The author used the following procedure to conduct experiments towards achieving four- and five-particle steering [1]. PDMS devices were obtained from the SU8 molds through replication molding. For this, 10 parts of silicone elastomer (Sylgard 184 Dow Corning) was mixed with 1 part curing agent (Sylgard 184 Dow Corning), poured over the SU8 mold to a height of 0.5 mm, and cured at 80°C for one hour. A razor was used to cut a section of the PDMS containing the microchannels and peeled by hand. Reservoirs were further cut out in the PDMS by hand using a razor blade. The PDMS with the microchannels was then pressed on to a Pyrex glass wafer to create sealed microchannels. The PDMS conforms to minor imperfections in the glass and gets bonded to it by weak Van der Waalls forces creating a reversible and watertight seal [33], [34].

To fill the microfluidic device, one drop of 2.2 micron fluorescent polystyrene beads (Duke Scientific) was added to 8 ml of DI water (J. T. Baker HPLC grade) and a drop of this solution was placed in one of the reservoirs at the channel inlet. After all the micro-channels filled by capillary action, reservoirs were filled with the solution. Platinum electrodes from the amplifier board attached to the computer were placed inside the reservoirs.

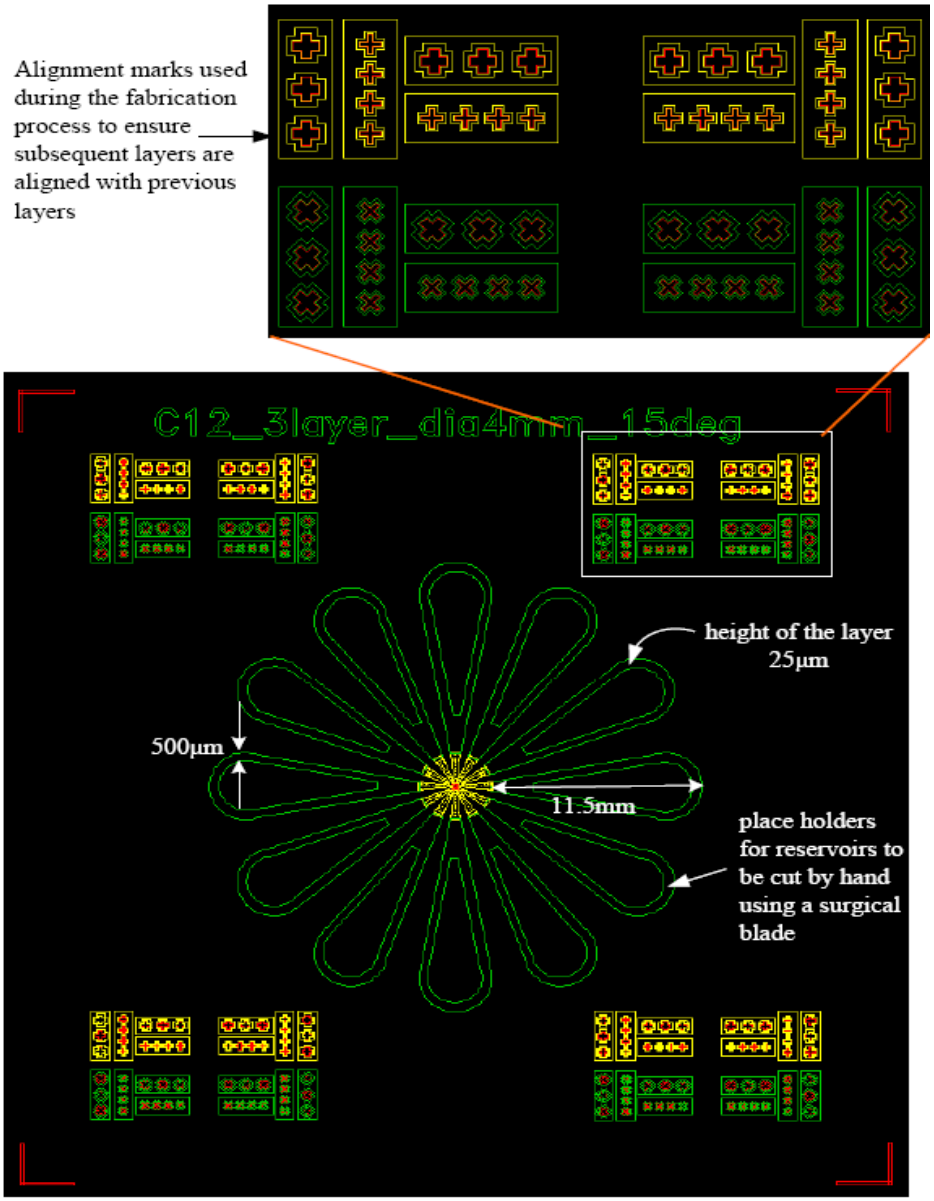

Figure 5.9: The green-colored portion of the Autocad drawing represents layer 3 of the high actuation microfluidic device. The annular structures are essentially place holders for reservoirs. Alignment marks for all three layers are also shown.

The microfluidic device was then placed under a microscope (Nikon TS100, 20x lens), illuminated by a bright 1 watt blue LED source (465 nm). A high pass filter (480 nm and longer, Chroma Technology Corporation) was placed before the camera as the polystyrene beads which emit light (510 nm - green) are seen more clearly as bright green on a gray background.

A 40 fps, 480 by 640 gray-scale pixel camera (Vision Components, VC2028E, Ettlingen, Germany) was used to transmit images to the computer. The images were then fed to the image processing algorithm that identified particle positions. The control algorithm then computed the voltage that needed to be applied to the electrodes to steer the particles along desired trajectories, and this voltage was applied to the electrodes through the amplifier attached to the computer. The selection of particles to be steered, input of the paths along which they should be steered, and changing the value of controller gain k was done through a graphical user interface. Details of this setup can be found in [1], [35].

5.6 Experiment Results - Five particle steering

The experimental demonstration of up to three-particle steering was published in [1]. This section presents experimental results for four- and five-particle steering experiments.

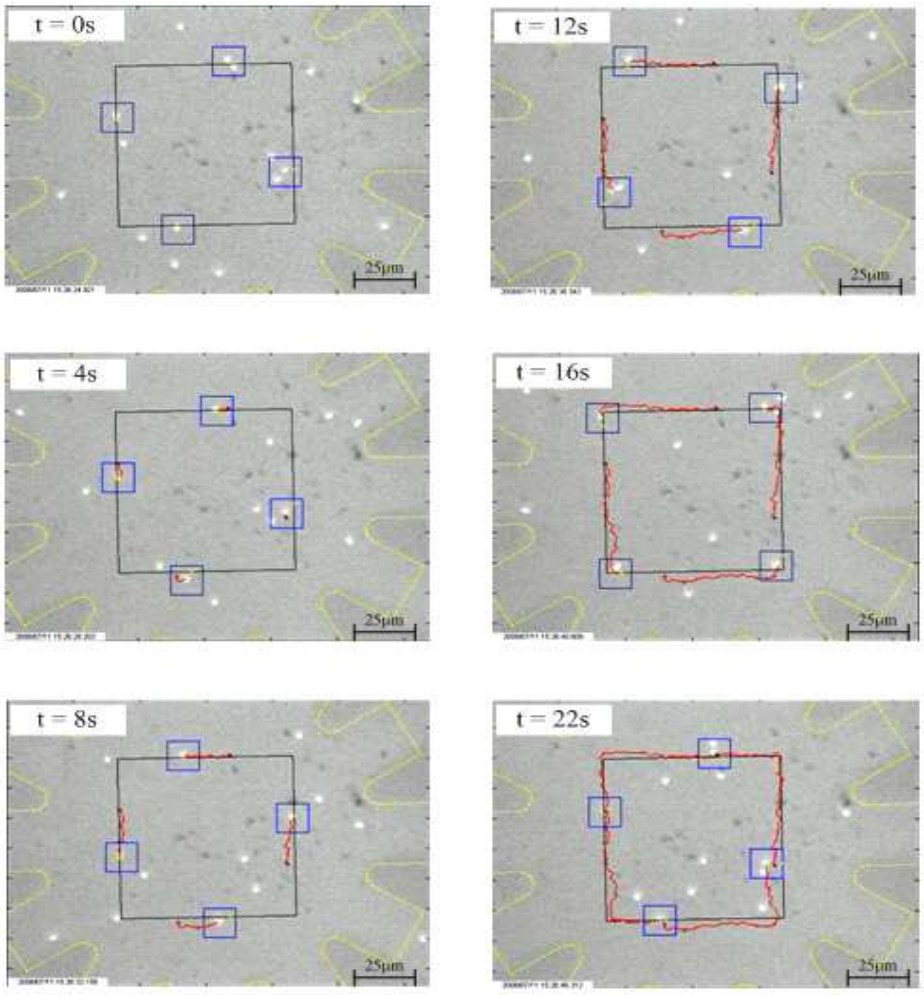

Figure 5.10: Steering of four fluorescent beads (2.2μm, Duke Scientific) along an optimal path between given initial positions (corresponding to $t =$ 0s) and final positions (corresponding to $t = 22$s). The particles being steered are enclosed in a square box. The path traversed by the particle is marked in red. The particles are controlled to an accuracy of better than 5 μm.

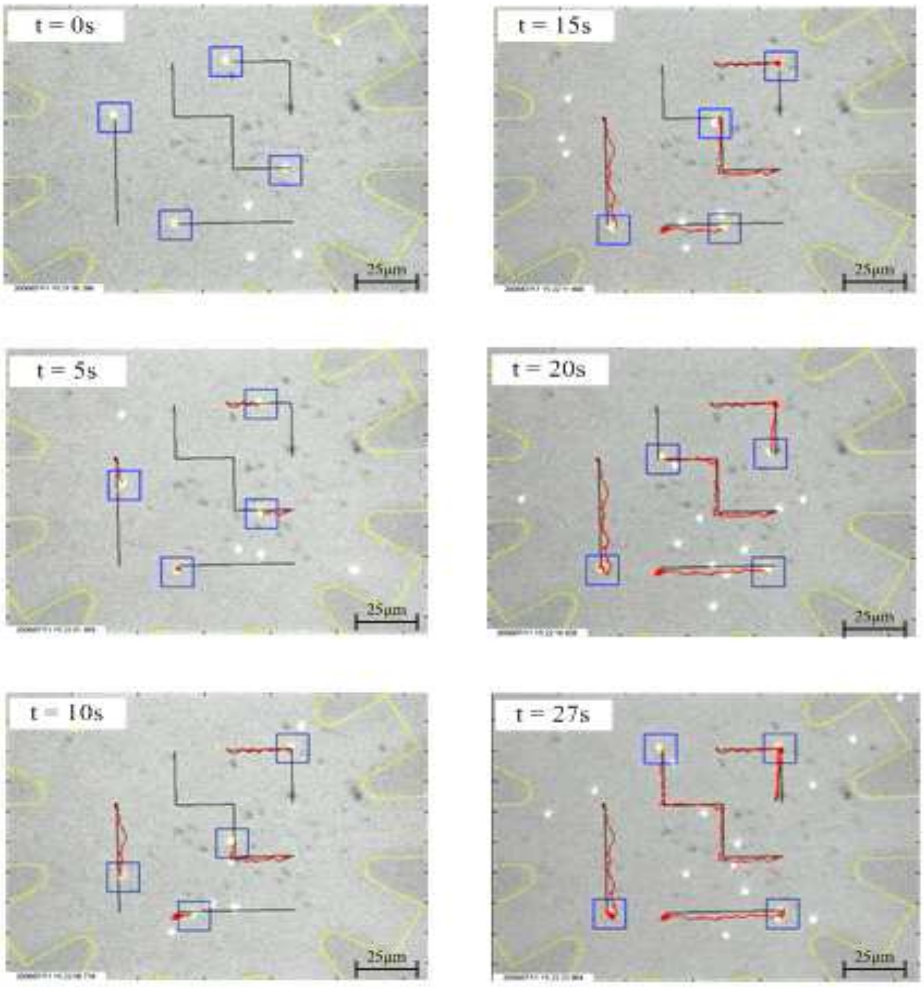

Figure 5.11: Steering of four fluorescent beads (2.2 μm, Duke Scientific) along an optimal path between given initial positions (corresponding to $t =$ 0s) and final positions (corresponding to $t = 27$s). The particles being steered are enclosed in a square box. The path traversed by the particle is marked in red. The particles are controlled to an accuracy of better than 5μm.

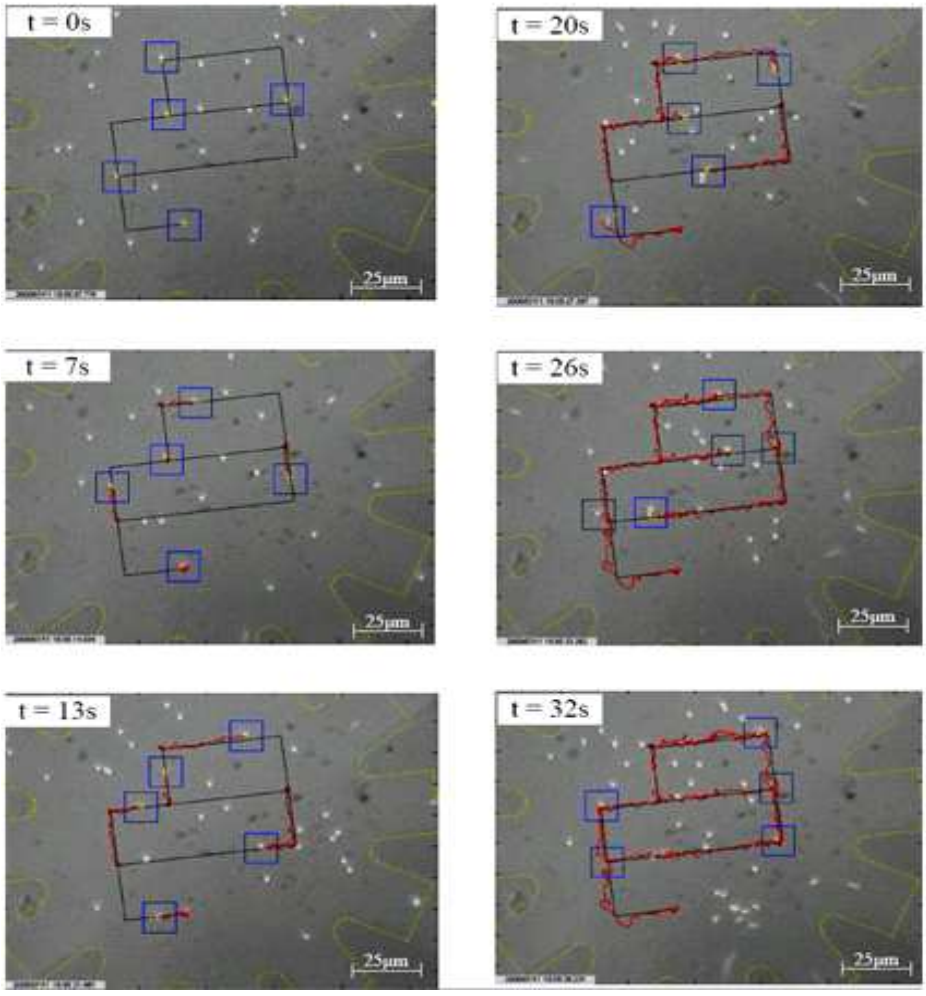

Figure 5.12: Steering of five fluorescent beads (2.2μm, Duke Scientific) along an optimal path between given initial positions (corresponding to $t =$ 0s) and final positions (corresponding to $t = 32$s). The particles being steered are enclosed in a square box. The path traversed by the particle is marked in red. The particles are controlled to an accuracy of better than 5 μm.

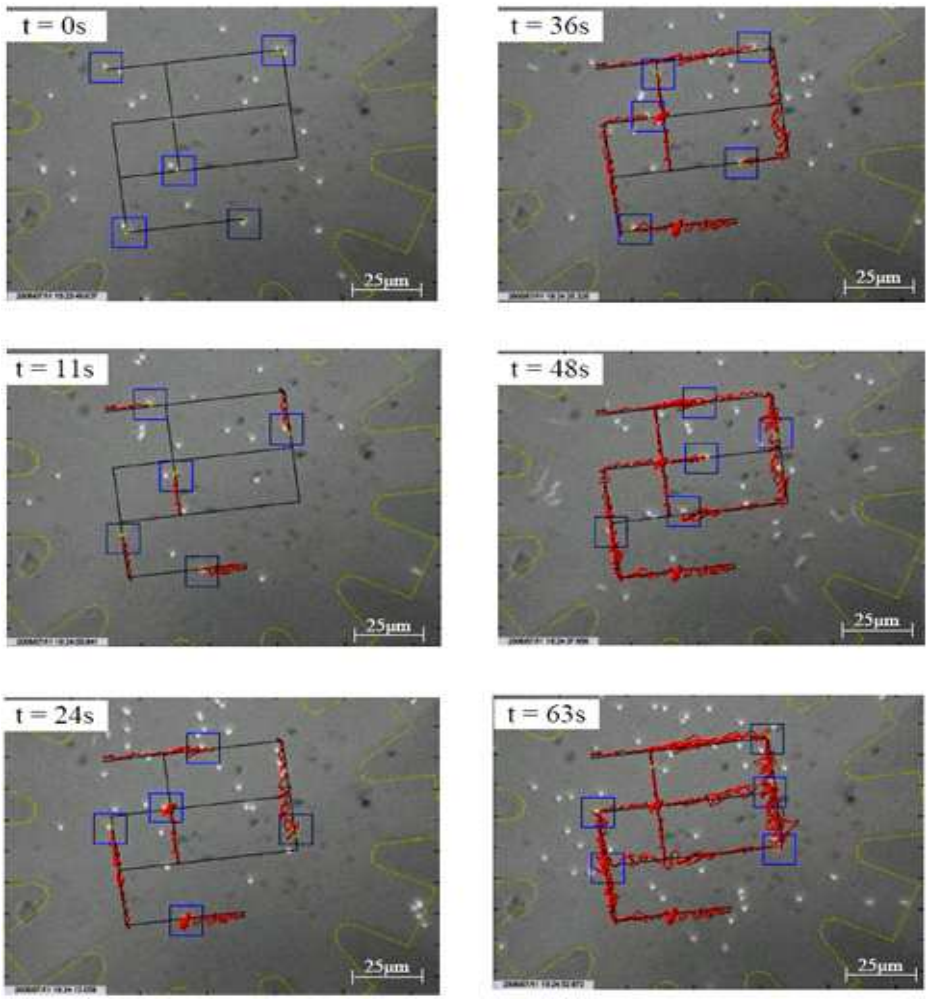

Figure 5.13: Steering of five fluorescent beads (2.2μm, Duke Scientific) along an optimal path between given initial positions (corresponding to $t =$ 0s) and final positions (corresponding to $t = 63$s). The particles being steered are enclosed in a square box. The path traversed by the particle is marked in red. The particles are controlled to an accuracy of better than 5μm.

5.7 Lessons Learned

When conducting experiments, we found that taking the following precautions can immensely reduce the effort needed in conducting experiments.

1. The thickness of the PDMS device should be about 0.5 mm for twelve channel devices. The reason for this is that, the reservoirs are very close to each other and they have to be cut out by hand using a blade. This is a very delicate and meticulous task and is very difficult to perform on thick PDMS devices.

2. When cutting out reservoirs in PDMS devices, care should be taken to ensure that the side etched with the microchannels faces upwards. This tends to prevent blockage of the microchannels due to improperly cut PDMS rough edges.

3. During the experiments, polystyrene beads stick to the Pyrex glass wafer and PDMS device and hence the devices cannot be used before removing the beads from the previous experiments. Creating a fresh batch of PDMS devices for each experiment is tedious. To reuse the PDMS devices, they should be thoroughly cleaned after each experiment. For the cleaning to be effective, the PDMS layer should first be peeled off from the Pyrex glass wafer. The polystyrene beads stuck to the PDMS layer can be removed by placing it in a sonicator, and then blow drying it with a hair dryer. Dust and oils on the PDMS can be removed by placing a piece of scotch tape on the surface and peeling it off. The Pyrex glass is best cleaned using warm water and household

dish detergent (Dawn).

4. Often, filling the microchannels with DI water using capillary action can be challenging. A common practice is to place a drop of ethanol at the inlet of one of the microchannels, which due to its higher surface tension almost instantly fills up all microchannels, and then all reservoirs can be filled with DI water. We found this to be one of the major causes of inconsistency in our experiments, as often, ethanol would seep under the PDMS and short electrical connection between two reservoirs leading to unpredictable actuation behavior. It is recommended that ethanol not be used, and only DI water be used directly to fill the microchannels. If the fluid gets stuck, gently tapping the PDMS with a finger can prod the fluid to fill the channels. While this may take a few minutes, it leads to more predictable behavior of the device.

5.8 Author's Specific Contributions to Experiments

The author's specific contributions to the 4 and 5 particle steering experiments are listed below:

1. Designed and developed detailed specifications for the high actuation microfluidic device.

2. Created Autocad files for the device design and got the SU8 molds fabricated from Stanford microfluidics foundry.

3. Fabricated and tested twelve channel PDMS devices using the mold.

4. Conducted and troubleshot all experiments for four- and five-particle steering experiments.

5. Improved experimental procedures to enhance device reusability and reduce researcher fatigue associated with conducting experiments (listed later in this section).

Chapter 6

Conclusion

This thesis shows how to combine feedback control and microfluidics to steer many particles independently in microfluidic systems. This is an issue that is important for handling of biological materials in miniaturized systems or for handling particles like quantum dots that cannot be manipulated using laser tweezers.

Equations governing electroosmotic flow at the microscale are easily inverted and therefore these flows are amenable to control. We have exploited this finding to design a feedback controller to precisely control the motion of micro-particles in planar electroosmotically-actuated microfluidic devices. We have also successfully demonstrated the use of this controller to steer up to five particles in simulations and experimentally.

In order to efficiently steer particles in the microfluidic devices, it is essential that particles do not come very close to each other during the steering process. To this end, we have developed a systematic method of generating paths which ensures that a certain minimum distance is always maintained between any two particles at all times. We have also outlined an optimal path planning method to pick the most efficient of these paths.

As the number of particles increase, the maximum speed at which they can be steered drops rapidly. If the electroosmotic actuation is weaker than the parasitic

pressure drift in the device, we are unable to steer the particles. This was the primary obstacle which initially prevented us from demonstrating steering of more than three particles experimentally. To this end, we designed devices in which the elecroosmotic actuation was several times higher than that in our earlier devices. We have used these high actuation devices to demonstrate steering of five particles in experiment.

Thus we have shown that feedback control, optimal path planning, and design of high performance devices can enable sophisticated particle steering capabilities in electroosmotically actuated microfluidic devices. The entire setup of microfluidic device, vision system, and computer can be miniaturized, hence permitting laser tweezer like capabilities in a hand held format.

Appendix A

Primer on Singular Value Decomposition

Any matrix $A \subset \mathbb{R}^{a\times b}$ of rank r can be factored [29] as:

$$A = Q\Sigma W^T = \begin{bmatrix} \overrightarrow{q}_1 & \overrightarrow{q}_2 & .. & \overrightarrow{q}_a \end{bmatrix} \begin{bmatrix} \sigma_1 & & & \\ & \sigma_2 & & \\ & & \ddots & \\ & & & \sigma_r \end{bmatrix} \begin{bmatrix} \overrightarrow{w}_1^T \\ : \\ : \\ \overrightarrow{w}_b^T \end{bmatrix}. \tag{A.1}$$

The columns of $Q \subset \mathbb{R}^{a\times a}$ given by $\overrightarrow{q}_i$ $(i = 1, 2, .., a)$ are eigenvectors of AA^T and are orthonormal.. The columns of $W \subset \mathbb{R}^{b\times b}$ given by $\overrightarrow{w}_i$ $(i = 1, 2, .., b)$ are eigenvectors of A^TA and are orthonormal. The r singular values on the diagonal of $\Sigma \subset \mathbb{R}^{a\times b}$ are the square roots of the non-zero eigenvalues of both AA^T and A^TA. The first r columns of W form the basis for the rowspace of A.The last $b-r$ columns of W form the basis for the nullspace of A.

The Singular Value Decomposition chooses these bases in an extremely special way. If A multiplies a column of W, it produces a multiple of a column of Q. More specifically

$$A\overrightarrow{w}_i = \sigma_i \overrightarrow{q}_i \text{ for all } \; i \leq r, \tag{A.2}$$

and

$$A\overrightarrow{w}_i = 0 \text{ for all } \; i > r. \tag{A.3}$$

If A^T multiplies a column of Q, it produces a multiple of a column of W. More

specifically

$$A^T \overrightarrow{q}_i = \sigma_i \overrightarrow{w}_i \text{ for all } \ i \leq r, \tag{A.4}$$

and

$$A^T \overrightarrow{q}_i = 0 \text{ for all } \ i > r. \tag{A.5}$$

Also, the non-zero eigenvalues of both AA^T and A^TA are σ_1^2, σ_2^2, ..., σ_r^2.Hence

$$AA^T \overrightarrow{q_i} = \sigma_i^2 q_i. \tag{A.6}$$

Premultiplying by $(AA^T)^{-1}$ and dividing by σ_i^2 we have

$$\frac{\overrightarrow{q}_i}{\sigma_i^2} = (AA^T)^{-1} \overrightarrow{q}_i. \tag{A.7}$$

This identity is used in chapter 3.

Bibliography

[1] M. Armani, S. Chaudhary, R. Probst, and B. Shapiro, "Using feedback control of micro-fluidics to independently steer multiple particles," *J. MEMS*, vol. 15, no. 4, pp. 945–956, 2006.

[2] A. Ashkin, "History of optical trapping and manipulation of small-neutral particles, atoms and molecules," *IEEE J. Select. Topics Quantum Electron.*, vol. 6, no. 6, pp. 841–856, 2000.

[3] J. E. Curtis, B. A. Koss, and D. G. Grier, "Dynamic holographic optical tweezers," *Opt. Commun.*, vol. 207, no. 1-6, pp. 169–175, 2002.

[4] D. G. Grier, "A revolution in optical manipulation," *Nature*, vol. 424, pp. 810–816.

[5] M. P. Hughes, "Strategies for dielectrophoretic separation in laboratory-on-a-chip systems," *Electrophoresis*, vol. 23, pp. 2569–2582.

[6] T. M. et al., "Trapping of micrometer and sub-micrometer particles by high frequency electric fields and hydrodynamic forces," *J. Phys. D: Appl. Phys.*, vol. 29, pp. 340–349.

[7] R. Pethig and M. T. et al., "Enhancing travelling-wave dielectrophoresis with signal superposition," *IEEE Eng. Med. Biol. Mag*, vol. 22, pp. 43–50.

[8] H. Morgan and N. G. G. et al., "Large area travelling wave dielectrophoresis particle separator," *J. Micromech. Mircoeng*, vol. 7, no. 2, pp. 65–70.

[9] H. M. Hertz, "Wave acoustic trap for nonintrusive positioning of microparticles," *J. Appl. Phys.*, vol. 78, pp. 4845–4849.

[10] H. Lee, T. Hunt, and R. Westervelt, "Magnetic and electric manipulation of a single cell in fluid," *Material Research Society Symp*, 2004.

[11] Y. F. et al., "A mems array for pneumatic conveyor and its control based on distributed systems," in *Proc. IEEE 18th International Conference on Microelectromechanical Systems*, Miami, USA, Jan. 2005.

[12] A. E. Cohen, "Control of nanoparticles with arbitrary two-dimensional force fields," *Phys. Rev. Lett.*, vol. 94, p. 118102.

[13] A. E. Cohen and W. E. Moerner, "Method for trapping and manipulating nanoscale objects in solution," *Appl. Phys. Lett.*, vol. 86, 2005.

[14] J. P. H. et al., "Patterning surfaces with colloidal particles using optical tweezers," *Appl. Phys. Lett.*, vol. 80, no. 25, pp. 4828–4830.

[15] S. Chaudhary and B. Shapiro, "Arbitrary steering of multiple particles independently in an electroosmotially driven microfluidic system," *IEEE Trans. Contr. Syst. Technol.*, vol. 14, no. 4, pp. 669–680, 2006.

[16] J. G. Santiago, "Electroosmotic flows in microchannels with finite inertial and pressure forces," *Anal. Chem.*, vol. 73, pp. 2353–2365, 2001.

[17] M. G. el Hak, *The MEMS Handbook*. New York, NY: CRC Press, 2002.

[18] M. Hayes, I. Kheterpal, and A. Ewing, "Effects of buffer ph on electroosmotic flow control by an applied radial voltage for capillary zone electrophoresis," *Anal. Chem.*, vol. 65, pp. 27–31, 1993.

[19] T. Huang, P. Tsai, C. Wu, and C. Lee, "Mechanictic studies of electroosmotic control at the capillary-solution interface," *Anal. Chem.*, vol. 65, pp. 2887–2893, 1993.

[20] P. Scales, F. Greiser, and T. Healey, "Electrokinetics of the silica-solution interface: A flat plate streaming potential study," *ACS J. Langmuir Surf. Colloids*, vol. 8, pp. 965–974, 1992.

[21] A. W. Adamson and A. P. Gast, *Physical chemistry of surfaces*. New York, NY: John Wiley and Sons, 1997.

[22] P. C. Hiemenz and R. Rajagopalan, *Principles of colloid and surface chemistry*. New York, NY: Marcel Dekker Inc, 1997.

[23] G. E. Karniadakis and A. Beskok, *Micro Flows: Fundamentals and Simulation*. New York, NY: Springer-Verlag, 2001.

[24] R. L. Panton, *Incompressible flow, 2nd Edition*. New York, NY: John Wiley and Sons, Inc., 1996.

[25] E. B. Cummins, "A comparison of theoretical and experimental electrokinetic and dielectrophoretic flow fields," *AIAA 2002-3193*, vol. 70, pp. 1–17, May 2002.

[26] R. F. Probstein, *Physiochemical Hydrodynamics.* New York, NY: Wiley-Interscience, 1994.

[27] L. C. Evans, *Partial differential equations.* Providence, RI: American Mathematical Society, 1991.

[28] D. T. Gillespie, "The mathematics of Brownian motion and Johnson noise," *Am. J. Phys.*, vol. 64, no. 3, pp. 225–240, 1996.

[29] G. Strang, *Linear Algebra and it's Applications.* New York, NY: Brooks/Cole, 1988.

[30] L. Perko, *Differential Equations and Dynamical Systems.* New York, NY: Springer Verlag, 2001.

[31] A. E. Bryson and Y. C. Ho, *Applied Optimal Control.* Levittown, PA: Taylor and Francis, 2004.

[32] Y. N. Xia and G. M. Whitesides, "Soft lithography," *Ann. Rev. Mater. Sci.*, vol. 28, pp. 153–184.

[33] D. C. Duffy, "Rapid prototyping of microfluidic systems in polydimethylsiloxane," *Anal. Chem.*, vol. 70, no. 23, pp. 4974–4984.

[34] G. M. Whitesides and J. C. McDonald, "Fabrication of microfluidic systems in polydimethylsiloxane," *Electrophoresis*, vol. 21, no. 1, pp. 27–40.

[35] R. Probst, "Optimal control of objects on the micro and nano scale by electrokinetic and electromagnetic manipulation of bio-sample preparation, quantum in-

formation devices and magnetic drug delivery," *PhD Dissertation, Department of Aerospace Engineering, University of Maryland*, 2010.